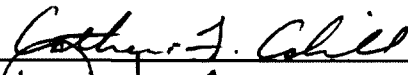
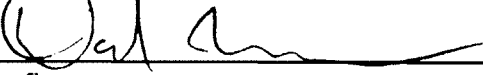
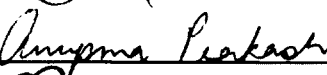
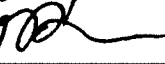


AN INTERDISCIPLINARY COMPUTATIONAL STUDY OF  
MAGNETOSPHERE-IONOSPHERE COUPLING AND ITS VISUAL AND THERMAL  
IMPACT IN THE AURORAL REGION


by

John Styers


RECOMMENDED:

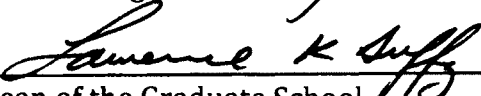
  
\_\_\_\_\_  
  
\_\_\_\_\_  
  
\_\_\_\_\_  
  
\_\_\_\_\_

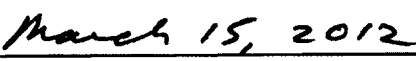
Advisory Committee Chair

  
\_\_\_\_\_  
Chair, Department of Geology and Geophysics

APPROVED:

  
\_\_\_\_\_  
Dean, College of Natural Science and Mathematics

  
\_\_\_\_\_  
Dean of the Graduate School

  
\_\_\_\_\_  
Date

**AN INTERDISCIPLINARY COMPUTATIONAL STUDY OF  
MAGNETOSPHERE-IONOSPHERE COUPLING AND ITS VISUAL AND THERMAL  
IMPACT IN THE AURORAL REGION**

**A**

**THESIS**

**Presented to the Faculty  
of the University of Alaska Fairbanks  
in partial Fulfillment of the Requirements  
for the Degree of**

**DOCTOR OF PHILOSOPHY**

**By**

**John Styers, A.A., B.S., M.S., M.S.**

**Fairbanks, Alaska**

**December 2011**

**© 2011 John Michael Styers**

UMI Number: 3528863

All rights reserved

INFORMATION TO ALL USERS

The quality of this reproduction is dependent upon the quality of the copy submitted.

In the unlikely event that the author did not send a complete manuscript and there are missing pages, these will be noted. Also, if material had to be removed, a note will indicate the deletion.

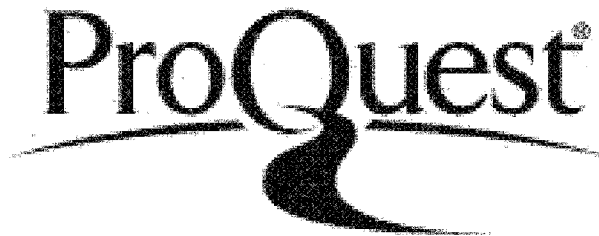


UMI 3528863

Published by ProQuest LLC 2012. Copyright in the Dissertation held by the Author.

Microform Edition © ProQuest LLC.

All rights reserved. This work is protected against unauthorized copying under Title 17, United States Code.



ProQuest LLC  
789 East Eisenhower Parkway  
P.O. Box 1346  
Ann Arbor, MI 48106-1346

**Abstract**

A three-dimensional, three-fluid simulation (ions, electrons, and neutrals) was explicitly parallelized, facilitating the study of small-scale magnetospheric-ionospheric (M-I) coupling processes. The model has ionization and recombination, self-consistently (semi-empirically) determined collision frequencies, and a height resolved ionosphere. Inclusion of ion inertial terms in the momentum equation enables the propagation of Alfvén waves. Investigation at small scales required large system domains, and thus fast parallel computers. The model was explicitly parallelized—enabling investigations of M-I coupling processes on very small temporal and spatial scales.

The generation, reflection, and propagation of Alfvén waves is of importance to the understanding of M-I coupling processes—it is, in fact, the primary means of communication of physical processes in the coupled system. Alfvénic reflections were modeled for two different boundary conditions, and it was shown that the deformation of the current layer was Alfvénic in character.

Visualizations of the data obtained appear to be consistent with the visual characteristics of actual discrete aurora in nature. The model reproduces qualitatively, and semi-quantitatively, in a self-consistent manner, some the behaviors of the formation and time-evolution of discrete arcs. These include the

narrowness of arcs; electric fields extending parallel outward from the arcs; and fast (plasma) flows in the region of discrete arcs.

Large-scale models—due to inevitable limitations of computational resources—need to make large-scale averages of computed properties. In regions of active small-scale structure, significant under-representation of the Joule heating occurs. It has been shown that the under-representation of the Joule heating in the region of active aurora can be as large as a factor of 8. This work includes a computer-based study of a quantitative approximation of this underrepresentation of the Joule heating by global, large-scale models and experimental observations.

## Table of Contents

	Page
<b>Signature Page</b> .....	<b>i</b>
<b>Title Page</b> .....	<b>ii</b>
<b>Abstract</b> .....	<b>iii</b>
<b>Table of Contents</b> .....	<b>v</b>
<b>List of Figures</b> .....	<b>viii</b>
<b>List of Tables</b> .....	<b>xi</b>
<b>List of Appendices</b> .....	<b>xii</b>
<b>Acknowledgements</b> .....	<b>xiii</b>
<b>Dedication</b> .....	<b>xiv</b>
<b>Chapter 1: Introduction</b> .....	<b>1</b>
<b>Introduction and Motivation</b> .....	<b>1</b>
<b>Outline of the Thesis</b> .....	<b>10</b>
<b>Chapter 2: Methodology</b> .....	<b>13</b>
<b>Model Boundary Conditions</b> .....	<b>17</b>
<b>Model Initial Conditions</b> .....	<b>19</b>
<b>Derivation of Ohm's Law</b> .....	<b>21</b>
<b>Relevant Scale Sizes and Model Limitations</b> .....	<b>24</b>
<b>Chapter 3: Alfvénic Model Physics and Implementation Details</b> .....	<b>27</b>
<b>Introduction and Motivation</b> .....	<b>27</b>
<b>Accelerator Mechanisms</b> .....	<b>28</b>
<b>Generator Mechanisms</b> .....	<b>33</b>
<b>Discussion of Models</b> .....	<b>37</b>
<b>Simple Alfvén Wave</b> .....	<b>37</b>
<b>Derivation of the Reflection Coefficient</b> .....	<b>38</b>

<b>Diagnostic .....</b>	<b>42</b>
<b>Reconnection Region .....</b>	<b>42</b>
<b>Alfvén Wave Reflection .....</b>	<b>47</b>
<b>Boundary Conditions A .....</b>	<b>47</b>
<b>Boundary Conditions B .....</b>	<b>48</b>
<b>Introduction to the Simulation .....</b>	<b>54</b>
<b>Inventory of Runs.....</b>	<b>54</b>
<b>Basic Properties.....</b>	<b>56</b>
<b>Alfvén Wave Diagnostic.....</b>	<b>66</b>
<b><math>E_{\parallel}</math> Source for Alfvén Wave Generation.....</b>	<b>66</b>
<b>Discussion of Various Cases.....</b>	<b>74</b>
<b>Influence of Initial Conditions .....</b>	<b>74</b>
<b>Boundaries .....</b>	<b>76</b>
<b>Conductance.....</b>	<b>81</b>
<b>Realistic Ionospheric Conductivities .....</b>	<b>84</b>
<b>Discussion.....</b>	<b>86</b>
<b>Chapter 4: Joule Heating.....</b>	<b>88</b>
<b>  Introduction and Motivation .....</b>	<b>89</b>
<b>  Boundary Conditions .....</b>	<b>96</b>
<b>  Results.....</b>	<b>97</b>
<b>  Boundary Conditions A .....</b>	<b>97</b>
<b>  Boundary Conditions B .....</b>	<b>104</b>
<b>  Discussion.....</b>	<b>107</b>
<b>Chapter 5: Conclusions.....</b>	<b>111</b>
<b>References .....</b>	<b>117</b>

**Appendices..... 127**



## List of Figures

<b>Figure 1.1 Magnetosphere-Ionosphere System .....</b>	<b>1</b>
<b>Figure 1.2 Magnetosphere-Ionosphere Coupled System.....</b>	<b>4</b>
<b>Figure 2.1 Imposed Shear.....</b>	<b>20</b>
<b>Figure 3.1 Alfvén Reflection .....</b>	<b>40</b>
<b>Figure 3.2a Velocity Perturbations Over Magnetic Field Perturbations.....</b>	<b>45</b>
<b>Figure 3.2b Velocity Perturbations Over Magnetic Field Perturbations.....</b>	<b>45</b>
<b>Figure 3.3 Reconnection Region .....</b>	<b>46</b>
<b>Figure 3.4 Progression of an Alfvén Wave.....</b>	<b>51</b>
<b>Figure 3.5 The Alfvén Relation .....</b>	<b>52</b>
<b>Figure 3.6 Progression of an Alfvén Wave.....</b>	<b>53</b>
<b>Figure 3.7 Magnetic Shear (3d View) .....</b>	<b>58</b>
<b>Figure 3.8 Magnetic Shear—Viewed From Above .....</b>	<b>58</b>
<b>Figure 3.9 3-D Structures of Deformation of the Current Sheet.....</b>	<b>59</b>
<b>Figure 3.10 Idealized Appearance of the Reconnection Region.....</b>	<b>62</b>
<b>Figure 3.11 The Appearance of the Reconnection Region .....</b>	<b>63</b>
<b>Figure 3.12 The Integrated Appearance of the Reconnection Region .....</b>	<b>63</b>
<b>Figure 3.13 The Magnetic Field in the Vicinity of the Reconnection Region.....</b>	<b>64</b>
<b>Figure 3.14 The Velocity in the Vicinity of the Reconnection Region .....</b>	<b>64</b>
<b>Figure 3.15 Velocity Perturbations for the Reference Run.....</b>	<b>65</b>
<b>Figure 3.16 Electric Field Perturbations for the Reference Run.....</b>	<b>65</b>
<b>Figure 3.17 Progress of the Deformation of the Magnetic Field Lines .....</b>	<b>70</b>
<b>Figure 3.18 Alfvén Plot Showing the Progress of the Alfvén Wave .....</b>	<b>70</b>
<b>Figure 3.19 Alfvénic Structures.....</b>	<b>71</b>
<b>Figure 3.20 Alfvén Structures for Decreasing Altitude .....</b>	<b>72</b>

<b>Figure 3.21 Alfvén Structures for Decreasing Altitude .....</b>	<b>73</b>
<b>Figure 3.22 3-D Perturbations.....</b>	<b>78</b>
<b>Figure 3.23 3-D Structures of Deformation of the Current Sheet .....</b>	<b>79</b>
<b>Figure 3.24 Sufficient Driver to Maintain Shear .....</b>	<b>80</b>
<b>Figure 3.25 Insufficient Driver (Erosion of Magnetic Shear) .....</b>	<b>80</b>
<b>Figure 3.26 Velocity Perturbations.....</b>	<b>82</b>
<b>Figure 3.27 Velocity Perturbations.....</b>	<b>83</b>
<b>Figure 3.28 Realistic Ionospheric Conductivities .....</b>	<b>85</b>
<b>Figure 4.1 Joule Heating Diagram.....</b>	<b>94</b>
<b>Figure 4.2 Joule Heating—Absence of Resistivity Region .....</b>	<b>99</b>
<b>Figures 4.3a, 4.3b, and 4.3c Velocity Perturbations in the x-y Plane.....</b>	<b>100</b>
<b>Figure 4.4 Velocity Perturbations and Joule Heating for a Shear Rate of 0.25 .....</b>	<b>103</b>
<b>Figure 4.5 Velocity Perturbations and Joule Heating for a Shear Rate of 0.50 .....</b>	<b>103</b>
<b>Figure 4.6 Velocity Perturbations and Joule Heating for a Shear Rate of 0.75 .....</b>	<b>104</b>
<b>Figure 4.7 Joule Heating for a Shear Rate of 0.25.....</b>	<b>105</b>
<b>Figure 4.8 Joule Heating for a Shear Rate of 0.50.....</b>	<b>105</b>
<b>Figure 4.9 Joule Heating for a Shear Rate of 0.75.....</b>	<b>106</b>
<b>Figure 4.10 Joule Heating for a Shear Rate of 1.00 .....</b>	<b>106</b>
<b>Figure 4.11 Peak of Joule Heating vs. Shear Rate (Boundary Conditions A)..</b>	<b>108</b>
<b>Figure 4.12 Peak of Joule Heating vs. Shear Rate (Boundary Conditions B)..</b>	<b>108</b>
<b>Figure 4.13 Peak vs. Collision Multiple (Conductivity) .....</b>	<b>109</b>
<b>Figure A.1 1-D Leap method, Time vs. Space .....</b>	<b>128</b>
<b>Figure A.2 1-D Lax-Wendroff Method—Time vs. Space .....</b>	<b>130</b>
<b>Figure A.3 Parallelization Scheme.....</b>	<b>132</b>

<b>Figure A.4 One-Dimensional Domain Decomposition .....</b>	<b>133</b>
<b>Figure A.5 Boundary Update Scheme .....</b>	<b>137</b>
<b>Figure A.6 Single Processor Computation Times .....</b>	<b>138</b>
<b>Figure A.7 Single Processor Computation Times .....</b>	<b>139</b>
<b>Figure A.8 Total Time for Fixed "Large" Domain Size.....</b>	<b>139</b>
<b>Figure A.9 VAMPIR Timeline Plot, Number of Processors vs. Time .....</b>	<b>141</b>
<b>Figure A.10 VAMPIR Summary Chart .....</b>	<b>142</b>

**List of Tables**

<b>Table 3.1 Inventory of Runs .....</b>	<b>55</b>
<b>Table 3.2 Computed Conductances .....</b>	<b>56</b>
<b>Table 4.1 Inventory of Runs .....</b>	<b>97</b>

**List of Appendices**

<b>Appendix A .....</b>	<b>127</b>
<b>Fitting Scheme .....</b>	<b>127</b>
<b>Integration Methods.....</b>	<b>127</b>
<b>The Courant Condition and Stability Considerations .....</b>	<b>131</b>
<b>Parallelization .....</b>	<b>131</b>
<b>Domain Decomposition.....</b>	<b>135</b>
<b>Languages .....</b>	<b>136</b>
<b>Parallel Distribution of the Grid .....</b>	<b>136</b>
<b>Boundary Update .....</b>	<b>136</b>
<b>Performance Testing.....</b>	<b>138</b>
<b>VAMPIR .....</b>	<b>140</b>
<b>Appendix B .....</b>	<b>144</b>
<b>Appendix C.....</b>	<b>178</b>
<b>Appendix D .....</b>	<b>183</b>

## **Acknowledgements**

I don't have words, to express my gratitude of, and admiration (both professional and personal) for, my advisor Dr. Greg Newby, and my committee: Dr. David Newman, Dr. Anupma Prakash, and Dr. Cathy Cahill. There is nothing that I could put down in these lines, that would express the fullness of my heart—or give them the credit that that they so fully deserve. I would also like to acknowledge the many helpful discussions with Dr. John Craven—whose “homespun wisdom” I found welcome more than once.

I would also like to acknowledge the invaluable personal discussions with Dr. Charles Deehr, Professor Dan Swift, and Dr. Michael Danielides—whose help in necessary matters was so great, I have—not terribly infrequently—referred to him as a second advisor. (Of note, I would like to mention that *every* time I spoke with Dr. Deehr and Professor Swift, I learned something new. The list of people I can say that about, is very short indeed.)

And this list would be frightfully incomplete, without mentioning the invaluable assistance of the Graduate School: Dr. Larry Duffy, Laura Bender, Juan Goula, and “Shelly” Baumann. That is one special team, that would shine anywhere—all the more brightly here at UAF.

## Dedication

I would like to dedicate this work to my Father, James Arthur Styers—who lived his life as a “living sacrifice” to/for his children, something I’m not sure I would’ve even been able to *do*, let alone so well. I would not have been able to complete this work without him.

I would also like to mention RoSie—the bestest, cutest, most *wonderful* “doggie” in the whole, wide world. “Someone” who made me “automatically happy”—no matter the mood I was in. I miss Rosie. ☹ ☹ ☹ ☹

I would also like to thank the Parson – Dudes and Dudettes—not only for Robert’s inestimable contribution to “The Red Green Regatta” ( ☺ ☺ ), but also for being some of *the coolest* people I have ever met.

I would also like to thank “The Anime Store” (no longer extant), Kevin, Candice, Liz, John, and the other young people of “The Comics Shop,” and “Wolf” who (in “The Eleventh Hour” ☺ ;) ) ran the Barnes and Noble “Doctor Who Book Club”—for just about the only mental stimulation I was to receive in my 11+ year stay in Fairbanks. Oh, and more than an “honorable mention” goes to Peter Payne of “JList,” in that regard.

While still on the subject of Fairbanks, I would like to also mention Dorlenn. Smart people in Fairbanks are, sadly, all too rare—smart, cool people are a *real* commodity. ☺ ;) And no discourse on Fairbanks would be complete, without a

mention of Jay and The Mayflower Buffet—keeping countless graduate students sufficiently “calorated” to do their work. “—What happens in the Mayflower, stays in the Mayflower.” ☺ ;)

I would also like to thank that Fred Meyers cashier—Angela—for being so nice to me, all these years. And Speaking of Fred Meyers, I would also like to thank a man who works in the liquor store [there], and who I know only as “Jim”—who, it is sad, but completely true, to say, showed more interest into the well-being and progress of my studies in the space of a year, than my entire academic department in all my time here: “Hey, Doc!”. ☺ ☺ I would also like to thank Suncha and Marsha of that bank that changes its name every five minutes. ☺ ;) Two saint-like people, who have helped me more times than I can count. I have doubtless forgotten to mention countless others.

“The world exists in order that we may create from it their excellence; and so that I—I myself—can communicate to others that beauty which else they might never see. I should understand something now, should I not, of that grace and those forms, dug from and shaped to transcend this dreary place where we scratch about and wait to die? Clay scabbled out of the dungy earth, mixed with water, with sand, with flint, with ashes of bones; kneaded, caressed and moulded by patient hands; fired in the kin and put to work to ease our lot, to add comfort and a little style to our necessity to eat, to drink, to wash, to excrete; or set up simply to be admired, like music, for our dignity and pleasure; and, like our own flesh, doomed at last to be



shattered and discarded, rubbish trampled back into the ground hence it came.  
What else thus bodies forth the nature of life and manifests, from the finite, the  
infinite? I have work to do. Somehow, my grief and loss are to enrich the world."

-Richard Adams

"The Girl in a Swing"

## Chapter 1 Introduction

### Introduction and Motivation

The sun is the source of virtually all energy on our planet. From the sun streams a flow of very fast plasma, with a frozen-in magnetic field. This solar wind interacts with the magnetosphere of the Earth, providing a source of energy, and determining the dynamics of the coupled magnetosphere-ionosphere system.

The coupling of the magnetosphere and the ionosphere is an important component of magnetospheric dynamics. The dynamics are determined by physical processes which occur at the magnetospheric boundaries. The outer boundary is the magnetopause. The magnetopause is defined as the region where the magnetospheric effects overcome those of the shocked solar wind plasma. The inner boundary of the magnetosphere is the ionosphere. For a sketch of the magnetosphere-ionosphere system, see Figure 1.1.

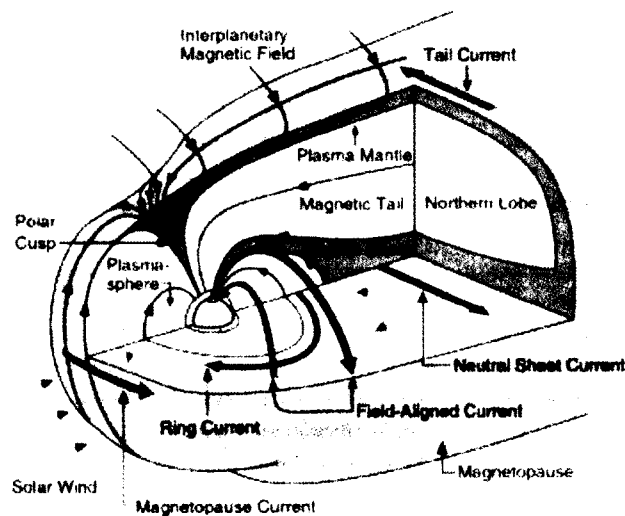


**Figure 1.1** Magnetosphere-Ionosphere System [Crooker, Greenwald, Hesse, Hudson, Hughes, Lyons, Maynard, Ryssel, and Siscoe 1999].

The sun emits a highly conducting plasma at very fast speeds ( $\sim 500$  km/s)—the solar wind. This plasma consists mainly of electrons and protons, with approximately 5% Helium ions. Because of the plasma's high conductivity, the magnetic field of the plasma is frozen in. Please note that—while the solar wind plasma has an extremely high conductivity—it is not a superconductor. Superconductors expel magnetic flux, while the magnetic field is “frozen in,” in the solar wind plasma. At the distance from the sun equal of the Earth's orbit, typical values of the electron particle density are  $\sim 5 \text{ cm}^{-3}$ ; typical values of the particle temperature are  $10^5 \text{ K}$ ; and a typical value of the interplanetary magnetic field is 5 nT. Values can vary greatly during storm times.

The solar wind plasma strikes the Earth's magnetic field. It cannot easily penetrate, and is slowed—and most of the solar wind passes around this obstacle. As the solar wind strikes with supersonic speed, a bow shock is generated. As the solar wind is slowed, some of its potential energy is converted into heat. The area earthward of the bow shock is called the magnetosheath. It is denser, hotter, and its magnetic field is stronger than the solar wind. The boundary of the magnetosheath is defined by the position(s) of the bow shock and the magnetopause; it represents the boundary of where the plasma conditions of the solar wind are overcome by those of the magnetosphere.

The magnetosphere is the cavity created by the presence of the Earth's magnetic field in the solar wind. The magnetosphere is highly distorted by the

kinetic energy imparted from the solar wind—compressed on the dayside, and stretched into a long magnetotail on the nightside.

Most of the plasma in the magnetotail is found in the plasma sheet—a sheet roughly in the plane of the magnetic equator. The remainder is contained in the magnetotail lobes—a region of much more rarified plasma.

Ultraviolet light continually strikes the dayside of the Earth, ionizing atoms. At high enough altitudes, collisions become so rare that an abundance of ions accumulates. This region is called the ionosphere. Typical values of the electron density are  $\sim 10^5 \text{ cm}^{-3}$ ; typical values of the electron temperature are  $\sim 10^3 \text{ K}$ ; a typical value for the magnetic field is  $10^4 \text{ nT}$ . The ionosphere starts at around 100 km above the Earth's surface, and extends up to around 450 km.

At mid- and low- latitudes, the ionosphere gives rise to a co-rotating (with the Earth) torus of cooler, but denser, plasma called the plasmasphere. At the equator, the plasmasphere extends outward to a distance of about  $4 R_E$ . Its outer boundary is the plasmopause.

A diagram of the interaction of the coupled magnetosphere-ionosphere system is shown in Figure 1.2. The system consists of the ionosphere, where collisions of charged particles with neutrals cannot be neglected, and the magnetosphere, where collisions are so infrequent that one can treat it as

collisionless. The system is strongly coupled, as the magnetic field connects them.

There is a flow of both energy and momentum between the two systems.

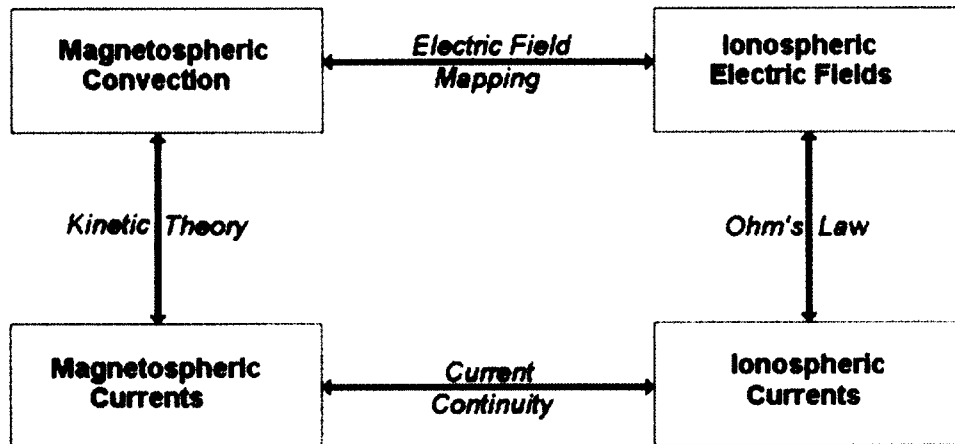


Figure 1.2 Magnetosphere-Ionosphere Coupled System (after Fig. 5.16. in Baumjohann and Treumann, 1997)

Being coupled, a change in one part of the system will change other parts of the system. A change in the magnetospheric convection will change the electric field mapped to the ionosphere. Ionospheric current flow will then change, due to the altered electric field, through Ohm's law. Current continuity requires the field-aligned currents to close, and this will alter the magnetospheric current distribution—which is due to the drift of charged particles.

Changes cannot be made in one system without affecting the other. Plasma motion in the magnetosphere generates Alfvén waves. Alfvén waves are a class of hydromagnetic waves. They are transverse electromagnetic waves, which propagate along the direction of the magnetic guide field (Parks 1991). Alfvén

waves impinging on the ionosphere can travel progressively downwards into regions of higher neutral densities. Continually increasing friction (as the wave travels deeper into the ionosphere) with the neutrals makes it progressively more difficult for the charged particles to move—eventually causing the Alfvén wave to be partially reflected, and partially absorbed. On reaching the magnetosphere, this Alfvén wave will produce plasma motion, spawning another Alfvén wave. Alfvén waves are thus the primary means of communication between the coupled magnetospheric and ionospheric systems.

Gradients in the convection generate field-aligned currents, which propagate into the ionosphere. (Uniform displacement of magnetic field lines in a uniform system produces no current. A gradient is required, because uniform motion would just represent a shift of the plasma, and thus no net current.) These currents must close perpendicularly to the magnetic field, as they cannot pass below the lower regions of the ionosphere. The lower ionosphere provides the lower boundary, at which these currents must close. How these currents close is determined by properties of the ionosphere. Communication in the magnetosphere is mainly carried out via Alfvén waves, and these waves carry the field-aligned current. Therefore, to successfully model these field-aligned currents, one must include the equations which can resolve Alfvén wave propagation.

Magnetosphere-ionosphere (M-I) coupling has been studied for several decades. The spatial and temporal resolution considered in the M-I system varies greatly—ranging from rapidly moving auroral arcs (as small as 100 m), to global

convection (several thousand km). Various models have been developed to study M-I coupling at various scales (e.g. Wolf, Harel, Spiro, Voigt, Reiff, and Chen 1982; Harel, Wolf, Reiff, Spiro, Burke, Rich, and Smiddy 1981; Kan 1998; Roble and Rees 1977; Fuller-Rowell and Rees 1980; Sojka 1989; Schunk 1988; Roble, Ridley, and Dickinson 1987; Maurits and Watkins 1996)

The plasma properties in the different regions of the M-I system vary greatly. Many methods have been used to model the regions of differing plasma dynamics. In the majority of the magnetosphere, the plasma is collisionless. In such regions the frozen-in condition (i.e.  $\vec{E} + \vec{v} \times \vec{B} = 0$ ) applies, and the ideal magnetohydrodynamic (MHD) equations are used. In the ionosphere, collisions (electron-neutral, ion-neutral, and Coulomb) generate a finite conductivity—and the ionosphere is treated as a partially conducting boundary to the magnetosphere. Several large-scale steady state M-I coupling models have been developed (e.g. Axford 1969; Vasyliunas 1970a; Vasyliunas 1972). These models deal with the global convection pattern, resolved on a temporal scale of several minutes.

There have also been models developed to simulate large-scale magnetospheric dynamics (e.g. the Rice convection model for the inner magnetosphere, see Wolf, Harel, Spiro, Voigt, Reiff, and Chen 1982; Harel, Wolf, Reiff, Spiro, Burke Rich, and Smiddy 1981). In these simulations, the ionosphere is

usually treated as a height-integrated, partially conducting boundary, and thus does not fully resolve the ionospheric dynamics.

The basic principles behind the ionospheric plasma dynamics are relatively well understood (Schunk 1988). Below about 150 km altitude, the plasma in the ionosphere is characterized by high collision frequencies (electron-neutral, ion-neutral, and Coulomb). Above 150 km altitude, for both ions and electrons, collision frequencies are much smaller than the gyro-frequencies; thus, the  $\vec{E} \times \vec{B}$  drift of either electrons or ions does not make a contribution to the current. However, below about 120 km (lower E-region), the ion-neutral collision frequency ( $10^5 \text{ s}^{-1}$ ) can be much higher than the ion gyrofrequency (about  $300 \text{ s}^{-1}$  in a 0.5 gauss geomagnetic field), which means that the mean free path of the ions is significantly shorter than their gyroradius. Thus the ions in the lower E-region are no longer drifting in the  $\vec{E} \times \vec{B}$  direction. The electrons still move with the  $\vec{E} \times \vec{B}$  drift. Their gyrofrequency ( $9 \times 10^5 \text{ s}^{-1}$  assuming a 0.5 gauss geomagnetic field) is still much higher than their collision frequency ( $10^5 \text{ s}^{-1}$ ). The difference between the ion and electron drift motion gives rise to ionospheric currents perpendicular to the magnetic field. The component of the ion motion in the direction of the electric field gives rise to the Pedersen current. This current closes the field-aligned current. The electron's  $\vec{E} \times \vec{B}$  drift motion is the main source of the Hall current in the ionosphere. As the altitude increases from 120 to 150 km, the ions begin drifting in the  $\vec{E} \times \vec{B}$  direction.



Using the definitions of the Pedersen and Hall conductivities, the current in the ionosphere can be expressed as (c.f. **Chapter 2**):

$$\vec{j} = \sigma_0 \vec{E}_{\parallel} + \sigma_p \vec{E}_{\perp} + \sigma_H \hat{b} \times \vec{E} \quad (\text{Equation 1.1})$$

Where  $\sigma_0$ ,  $\sigma_p$ , and  $\sigma_H$  are the parallel, Pedersen, and Hall conductivities respectively;  $\hat{b}$  is the unit vector of the magnetic field;  $\vec{E}_{\parallel}$  and  $\vec{E}_{\perp}$  are the parallel and perpendicular components of the electric field with respect to the magnetic field. The ionospheric conductivities are determined from the ion-neutral and electron-neutral collision frequencies.

There have been various models developed to simulate large-scale convection in the ionosphere (e.g. Roble and Rees 1977; Fuller-Rowell and Rees 1980; Sojka 1989; Schunk 1988; Roble, Ridley, and Dickinson 1987; Maurits and Watkins 1996). For all these models, the velocity distribution is prescribed at the top of the simulation domain.

These can be useful to study large-scale ionospheric convection. However, they are unable to resolve either small spatial structures, or changes evolving on fast temporal scales. This is because, in order to run a global simulation, sacrifices in spatial and temporal scales must be made—as computer resources are limited.

All these models (necessarily) use a relatively long time step. Thus, the inertia term in the momentum equation (c.f. **Equation 2.2**) ends up being neglected. This eliminates the ability to model important plasma waves (Alfvén,

slow, and fast waves). The models are therefore unable to model the field-aligned current formation and subsequent evolution characteristic of small-scale auroral structures.

Auroral arcs can exhibit very small-scale structure (a width of as small as 100 m, e.g. Maggs and Davis 1968; Borovsky 1993). Arcs can also move rather quickly (several km per second)—faster than the usual velocity of the ambient plasma. Thus arcs display both small spatial and fast temporal scales.

To properly depict M-I coupling, a model must be able to resolve the relevant spatial and temporal scales. Such a model, for two dimensions, was developed (Zhu, Otto, Lummerzheim, Rees, and Lanchester 2001).

A new three-dimensional model is described in Chapter 2. Explicit parallelization greatly enhanced the size of the system domain—which allowed for modeling on very small spatial scales. With this model, we have been able to reproduce self-consistent features of discrete arc formation and evolution: i.e. very thin structures, reminiscent of actual auroral arcs; velocity shear parallel to the thin precipitation regions; and electric fields forming perpendicularly to the arc structures. Results also show that the ionosphere has significant feedback into magnetospheric evolution.

There are many unresolved issues of M-I coupling. The model developed in this thesis enabled the studying of some of these issues on fine numerical and spatial scales. A fully height-resolved, realistic ionosphere was modeled—which

enabled the study of Alfvén wave reflection. Discrete electron precipitation regions were modeled, and their time-evolution was observed. These regions, both qualitatively and semi-quantitatively, resemble discrete aurora.

Large-scale experimental observations and global models have limited spatial and temporal resolution, and yield parameters that are averaged both in space and in time. These large-scale experimental observations can fail to resolve accurate values for many important physical processes. A computer model designed to look at small-scale temporal and spatial scales was employed to make quantitative measurement of the Joule heating occurring over various scale averages.

Because of the (unavoidable) underestimation of the Joule heating in global models, they fail to match up with observations. Even with present-day computational resources, the largest supercomputers have limited ability to resolve small scales over a global simulation domain. Attempting to mitigate this mismatch was a partial motivation for this work.

A study was made of the under-measurement of Joule heating in the region of small-scale structure—showing as much as a factor of 8 under-valuing of the actual heating.

### **Outline of the Thesis**

A three-dimensional, three-fluid (ion, electron, neutral) model is described in Chapter 2. An existing model (originally developed by Birk and Otto 1996) was explicitly parallelized. This enabled the quantitative, self-consistent simulation of

the dynamics and structures of the ionosphere on fast temporal scales, and on small spatial scales. The model was designed to study the aurora, specifically discrete arcs.

The model includes a full set of dynamic equations for the neutrals, ions, and electrons. The height profile of the density and temperature of the neutrals is set phenomenologically—with two settings, depending on the level of solar activity. It computes the ion-neutral, electron-neutral, and Coulomb collision frequencies. The inclusion of the inertia terms in the momentum equation enables the modeling of Alfvén waves. This is essential to the successful modeling of the M-I system on small spatial and temporal scales.

This model has been employed to study M-I coupling processes, with emphasis on fast dynamics and small-scale structure. Several relevant and interesting results were obtained—pointing to the conclusion that ionospheric processes significantly alter magnetospheric dynamics.

Chapter 3 describes studies made of evolving M-I processes at small spatial and temporal scales. A self-consistent mechanism for the formation and evolution of discrete arcs was developed. An in-depth look was taken at reflection of Alfvén waves from the lower ionospheric boundary, and the development of consistent ionospheric conductivities.

Using the model, it was shown that the current sheet that forms as part of the mechanism of discrete arc formation has Alfvénic boundaries, and that the

propagation of Alfvén waves, on these boundaries, causes the spreading of the field-aligned current.

In Chapter 4, considerations of the Joule heating associated with small-scale structures were explored, using the model. Large-scale observation and global models have limited spatial and temporal resolution, and yield parameters that are averaged in space and time. These large-scale observations fail to resolve true values for many important physical processes—resulting in an underestimation. (The same model was used to study Alfvén waves, with the added utility of calculating Joule heating on differing scale sizes.) This model was designed to look at small-scale temporal and spatial scales, and was employed to make quantitative measurement of the Joule heating occurring over various scale averages. This resulted in a quantitative approximation on the underestimation of the value of the Joule heating for large-scale models. A strong (approximately factor as high as eight) change was found from the smallest to largest scale averaging.

A summary of the simulation results is made in Chapter 5. Some suggestions for future work are also presented.

## Chapter 2: Methodology

M-I coupling is complex. Models are often employed to understand the underlying processes. This chapter describes the equations developed for this work, and how they are solved.

The interaction of a highly collisionless plasma with a strongly collision dominated plasma requires an extension of the usual fluid plasma equations, to include the transport which dominates ionospheric dynamics. A code originally written by Birk and Otto (1996) was explicitly parallelized, enabling a study of the fine-scale structure of M-I (magnetosphere-ionosphere) coupling on very fine temporal and spatial scales. It is believed that this model successfully reproduces all the physics (e.g. Alfvén wave propagation and reflection, inertia, friction) relevant to the problems addressed.

The model includes ionospheric transport as source terms (mass, momentum, energy) in the set of fluid plasma equations. The model is three-fluid (electrons, ions, neutrals). The set of equations used in the model is shown below. For the complete set of equations, see (Birk and Otto, 1996).

$$\frac{\partial \rho}{\partial t} = -\nabla \cdot \rho \vec{v} \quad (\text{Equation 2.1 Ion Continuity Equation})$$

$$\begin{aligned} \frac{\partial \rho \vec{v}}{\partial t} = & -\nabla \cdot (\rho \vec{v} \vec{v}) - \frac{1}{2} \nabla p + \rho \vec{g} + (\nabla \times \vec{B}) \times \vec{B} \\ & + \rho \vec{v} (\iota - \beta \rho) - \rho \vec{v}_n (\iota - \beta \rho) - \rho v_{in} (\vec{v}_n - \vec{v}) \end{aligned} \quad (\text{Equation 2.2 Ion-Inertia Equation})$$

$$\frac{\partial \bar{B}}{\partial t} = +\nabla \times (\bar{v} \times \bar{B}) - \nabla \times (\eta \nabla \times \bar{B}) \quad (\text{Equation 2.3})$$

$$\begin{aligned} \frac{\partial \rho}{\partial t} = & -\bar{v} \cdot \nabla \rho - \gamma p \nabla \cdot \bar{v} + (\iota - \beta \rho) T_n \\ & + (\gamma - 1) \left[ 2\eta (\nabla \times B)^2 \iota e_c - \frac{3v_{in}\rho}{m_i + m_e} (T_i - T_n) \left( \frac{m_n v_{in}\rho}{m_i + m_n} + \mu m_i \right) (v - v_n)^2 \right] \\ & + 3v_{eff} (T_n - T_e) + \frac{\partial}{\partial z} \left( \lambda_e \frac{\partial T_e}{\partial z} \right) \end{aligned} \quad (\text{Equation 2.4})$$

(Note that in the model, electron temperature terms were not used. Also, the electron temperature equation was not employed. For the study of Joule heating and Alfvén waves, one does not need the Hall conductivities; however, one does need the Pederson conductivities.)

Here  $\rho$  and  $\rho_n$  are the total plasma and neutral mass density;  $m_i$  and  $m_n$  are the ion and neutral particle mass;  $T_e$ ,  $T_i$ , and  $T_n$  are the electron, ion, and neutral temperatures;  $p$ ,  $p_e$ , and  $p_n$  are the total plasma pressure, electron pressure, and neutral pressure;  $n$  is the plasma number density;  $\bar{v}$ ,  $\bar{v}_e$ , and  $\bar{v}_n$  are the plasma, electron, and neutral velocities;  $\bar{B}$  is the magnetic induction vector;  $\bar{g}$  is gravitational acceleration;  $\iota$  is the ionization rate;  $v_{in}$  is the ion-neutral,  $v_{ei}$  is the Coulomb, and  $v_{eff}$  is the effective collision frequency between electrons and neutrals;  $\eta$  is the resistivity;  $\gamma$  and  $\gamma_n$  are the ratios of specific heats for the plasma and neutrals;  $e_c$  is the average energy that goes into

electron heating for each ionization process (a typical value is  $2eV$ );  $\lambda_e$  is the electron heat conduction coefficient; and  $\kappa = 1/(\gamma - 1)$ . For energy conservation, it is required that  $\gamma_n = \gamma = 5/3$ . The resistivity in the simulation is given by:

$$\eta = \eta_{ei} + \eta_{en} + \eta_{in} \quad (\text{Equation 2.5})$$

with  $\eta_{ei} = \lambda v_{ei} \tau_A$ ,  $\eta_{en} = \lambda v_{en} \tau_A$ , and  $\eta_{in} = \lambda v_{in} \tau_A$ . Where  $v_{ei}$ ,  $v_{en}$ , and  $v_{in}$  are the electron-ion, electron-neutral, and ion-neutral collision frequencies, the parameterization of  $v_{ei}$ ,  $v_{en}$ , and  $v_{in}$  is given in (Schunk, 1983),  $\tau_A = l_0 / v_A$  is the Alfvén time; and  $\lambda = \left( \frac{c}{\omega_{pe} l_0} \right)^2$  is a normalization coefficient.

The model assumes:

$$n = n_e = n_i \quad (\text{Equation 2.6})$$

$$\rho = n(m_e + m_i) \quad (\text{Equation 2.7})$$

$$p = p_e + p_i \quad (\text{Equation 2.8})$$

$$\rho \vec{v} = \rho_e \vec{v}_e + \rho_i \vec{v}_i \quad (\text{Equation 2.9})$$

The model assumes quasineutrality. This prevents the development of oscillations on the order of the plasma frequency. The physical argument for this is that the Debye length is very small. This is fortunate, as the inclusion of oscillations in the model on the order of plasma frequency not assuming quasineutrality would cause the model to be computationally untenable on the considered spatial and temporal scales, even with modern computing resources.



Thus, the model does not reproduce Langmuir waves. There is a set of similar equations for the neutrals. The inclusion of the ion-inertia terms (the terms to the left of the equals sign—and the first term to the right of it, in Equation 2.2) enables the model to produce Alfvén waves.

The model conserves mass, momentum, and energy. The transport coefficients are chosen semi-empirically as functions of mass and temperature. Please note that there is no self-consistent treatment of kinetic processes (collisions, ionization, and recombination)—however, the model does have ionization and recombination. There is momentum transfer between neutrals and plasma. The model includes collisional thermalization, and dissipative terms.

Quantities are normalized to the horizontal length scale  $l_0 = 1.0$  km; the vertical length scale to  $l_{z0} = 100$  km; the plasma and neutral number density  $n$  and  $n_0$  to  $n_0 = 50,000 \text{ cm}^{-3}$ ; the mass  $m_e$ ,  $m_i$ , and  $m_n$  to the mass of a carbon atom  $m_0 = m_{O^+}$ ; the mass density  $\rho$  and  $\rho_n$  to  $\rho_0 = n_0 m_0$ ; the magnetic field  $B$  to  $B_0 = 0.5$  G; the vertical velocity  $v_z$ ,  $v_{ez}$ , and  $v_{nz}$  to the Alfvén velocity

$$v_A = B_0 (\mu_0 \rho_0)^{-\frac{1}{2}} \quad (1,220 \text{ km s}^{-1}); \text{ the horizontal velocity } v_x \text{ and } v_y \text{ to } \frac{l_0}{l_{z0} v_A}$$

$(2.44 \text{ km s}^{-1})$ ; the pressure  $p$ ,  $p_e$ , and  $p_n$  to  $P_0 = B_0^2 / (2\mu_0)$ ;  $T_e$  and  $T_n$  to  $T_0 = P_0 / (n_0 k)$  ( $k$  = the Boltzmann constant); and the time  $t$  to the characteristic

Alfvén time  $\tau_A = \frac{l_{z0}}{v_A}$ , typically 0.1 seconds.

### **Model Boundary Conditions**

One must assume boundary conditions to solve the model equations. However, the system has no physical boundaries. This section describes the boundary conditions employed, and the motivation for said choice of boundary conditions.

The model employs Cartesian coordinates. The x and y directions are chosen perpendicularly and parallel to the current layer, respectively. The z direction is chosen in the vertical direction. The grid in the x-direction is irregularly spaced—in order to increase resolution near the current sheet. The grid in the z-direction is also irregularly spaced—to increase resolution towards the bottom of the simulation domain (the ionosphere). Present values allow a maximum resolution of 0.1 km in the x-direction, a maximum resolution of 0.4 km is possible in the y-direction, and a maximum of resolution of 250 km is possible in the z-direction.

At the positive and negative x boundaries, boundary conditions for densities, pressures, and temperatures are computed by extrapolation (continuous boundary conditions). That is, the values at the mathematical boundary were extrapolated from those at the physical boundary.

The magnetic field  $\vec{B}$ , the current  $\vec{j}$ , and the plasma velocity  $\vec{v}$  are determined from Ohm's law (see below). After the boundary conditions for

density  $\rho$  and pressure  $p$  are obtained, the collision frequencies are computed. The electric field is extrapolated from the physical boundary at the x boundaries, and the Pedersen and Hall conductivities are used to compute the current density from  $\vec{j} = \sigma \cdot \vec{E}$  on the boundary. The normal component of the magnetic field  $\vec{B}$  is determined from the relation  $\nabla \cdot \vec{B} = 0$ .

Periodic boundary conditions were employed in the y-direction—that is, the values at the lower y boundary were mapped to the upper y-boundary. This allowed waves to freely propagate through the system.

At the lower z boundary, two different boundary conditions were chosen. The first was identical to the x boundary conditions (above), and allowed the magnetic field lines to map out of the lower boundary of the system. The second set magnetic perturbations in the x and y directions to zero ( $\delta B_x = \delta B_y = 0$ ). This enabled the ionospheric currents to close, at the bottom of the system domain.

At the top boundary ( $z \sim \text{few } R_E$ ), the value at the mathematical boundary is computed by extrapolation of the values at the physical boundary, for most quantities. This maintains the initial perturbation for the Alfvén waves, and it is intended to allow the transmission of the waves that are reflected in the lower ionosphere.

The values for the magnetic field and the plasma velocity at the top of the simulation are imposed (upper z boundary). This spawns a downward-traveling

Alfvén wave, and permits the reflected Alfvén (from the ionosphere) to pass through the top of the simulation domain.

### Model Initial Conditions

Initial conditions are needed to solve the model equations. This presents a challenge—as M-I coupled systems do not have “initial conditions.” This section describes the initial conditions chosen, and the motivation for said choice.

The collision frequencies  $\nu_{en}$ ,  $\nu_{in}$ , and  $\nu_{ei}$  are computed as initial conditions.

The magnetic field (at the top of the simulation domain—the magnetosphere) is given by:

$$b_x = 0$$

$$b_y = b_{y0} \tanh(x) + \frac{1}{2} v_{y0} \frac{\tanh(2x)}{\cosh^2\left(\frac{x}{3}\right)} \frac{1}{2} \left[ 1 + \tanh\left(\frac{x - x_{\max} + 20}{4}\right) \right] \quad (\text{Equation 2.10})$$

$$b_z = \sqrt{b_{z0}^2 + \frac{b_{y0}^2}{\cosh^2(x)}}$$

The velocity at the top of the simulation domain (the magnetosphere) is given by:

$$v_x = 0$$

$$v_y = -\frac{1}{2} \frac{b_{z0}}{\sqrt{\rho_0}} v_{y0} \frac{1}{b_{z0}} \frac{\tanh(2x)}{\cosh^2\left(\frac{x}{3}\right)} \frac{1}{2} \left[ \frac{1 + \tanh(x - x_{\max} + 20)}{4} \right] \quad (\text{Equation 2.11})$$

$$v_z = j\nu_{z0}\rho$$

See Figure 2.1.

These boundary conditions were chosen to produce a clean, “pure Alfvén wave.” (Other conditions chosen would produce a “noise” of different plasma waves.) This superposition of differing types of plasma waves (traveling at different speeds) was not only more numerically untenable, but would have made this numerical study less precise and more difficult.

In the computation of the y-components of the magnetic field (Equation 2.11), the first hyperbolic tangent produces a shear across the simulation. The ratio of the hyperbolic tangent to the square of the hyperbolic cosine (second term) strengthens the magnetic shear across the simulation domain. The third term, a hyperbolic tangent, heightens the magnetic shear towards the center of the y-range.

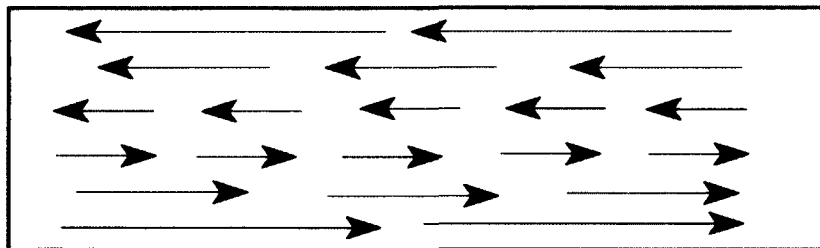


**Figure 2.1 Imposed Shear (Vectors) at the Top of the Simulation Domain—for Either the Magnetic Field or the Velocity (Differing only by Constants). Such a Choice of Conditions Facilitated the Spawning of a “Clean Alfvén Wave.”**

Please note that the mass density is conserved, at  $1 = n_0 m_0$ . Thus, as the molecular weight decreases with altitude, the numerical density (normalized to  $50,000 \text{ cm}^{-3}$ ) increases accordingly.

Note that it is the gradient that causes the generation of the field-aligned current. A uniform deformation of the magnetic field everywhere in the simulation would result in just a shift of conditions, and no net current.

### Derivation of Ohm's Law

Ohm's law provides the equation of motion for electrons and when combined with the induction equation it determines the evolution of the magnetic field (**Equation 2.3**). It is thus of vital importance in the understanding of ionospheric dynamics. The derivation of the version of Ohm's law used in the model follows.

The starting point for this derivation is the general momentum equation for the electron and the various ion species. However, the form used in the simulation (**Equation 2.3**) is different from the one commonly used:

$$\frac{\partial n_s \vec{v}_s}{\partial t} + \nabla \cdot (n_s \vec{v}_s \vec{v}_s) = -\frac{1}{m_s} \nabla \cdot \underline{\Pi}_s + \frac{q_s}{m_s} n_s (\vec{E} + \vec{v}_s \times \vec{B}) - \sum_{k \neq s} n_s \nu_{sk} (\vec{v}_s - \vec{v}_k) + \nu_s n_s \vec{v}_s - \mu_s n_s \vec{v}_s + \vec{P}_s \quad (\text{Equation 2.12})$$

Where  $\iota_s$  is the ionization frequency;  $\mu_s$  is the recombination frequency;  $\nu_{sk}$  is the (elastic/symmetric) collision frequency for momentum exchange; and  $\vec{P}_s$  is the first moment of the inelastic collision operator.

The electron and ion momentum equations are thus given by: (Note that charge neutrality is assumed:  $n_e = n_i \equiv n$ .)

$$\begin{aligned}
\frac{\partial n \vec{v}_e}{\partial t} &= -\nabla \cdot (n \vec{v}_e \vec{v}_e) - \frac{1}{m_e} \nabla \cdot \underline{\Pi}_e - \frac{e}{m_e} n (\vec{E} + \vec{v}_e \times \vec{B}) + n \vec{g} \\
&\quad - \nu_{ei} n (\vec{v}_e - \vec{v}_i) - \nu_{en} n (\vec{v}_e - \vec{v}_n) - n (\mu \vec{v}_e - \iota \vec{v}_n) \\
\frac{\partial n \vec{v}_i}{\partial t} &= -\nabla \cdot (n \vec{v}_i \vec{v}_i) - \frac{1}{m_i} \nabla \cdot \underline{\Pi}_i - \frac{e}{m_i} n (\vec{E} + \vec{v}_i \times \vec{B}) + n \vec{g} \\
&\quad - \nu_{ie} n (\vec{v}_i - \vec{v}_e) - \nu_{in} n (\vec{v}_i - \vec{v}_n) - n (\mu \vec{v}_i - \iota \vec{v}_n)
\end{aligned} \tag{Equation 2.13}$$

To bring this into a more suitable form to replace electron and ion velocity, current, and electric field, one rearranges the momentum equations for the electrons and neutrals:

$$\begin{aligned}
(\vec{v}_e - \vec{v}_n) &= -\frac{e}{m_e \nu_{en}} ((\vec{v}_e - \vec{v}_n) \times \vec{B} + \vec{E} + \vec{v}_n \times \vec{B}) + \frac{1}{\nu_{en} n} \vec{T}_e \\
(\vec{v}_i - \vec{v}_n) &= -\frac{e}{m_i \nu_{in}} ((\vec{v}_i - \vec{v}_n) \times \vec{B} + \vec{E} + \vec{v}_n \times \vec{B}) + \frac{1}{\nu_{in} n} \vec{T}_i
\end{aligned} \tag{Equation 2.14}$$

where

$$\begin{aligned}
\vec{T}_e &= -\frac{\partial n \vec{v}_e}{\partial t} - \nabla \cdot (n \vec{v}_e \vec{v}_e) - \frac{1}{m_e} \nabla \cdot \underline{\Pi}_e + n \vec{g} \\
&\quad - \nu_{ei} n (\vec{v}_e - \vec{v}_i) - n (\mu_e \vec{v}_e - \nu_e \vec{v}_n)
\end{aligned}$$

$$\begin{aligned} \vec{T}_i = & -\frac{\partial n\vec{v}_i}{\partial t} - \nabla \cdot (n\vec{v}_i\vec{v}_i) - \frac{1}{m_i} \nabla \cdot \underline{\Pi}_i + n\vec{g} \\ & - \mathbf{v}_{ei}n(\vec{v}_i - \vec{v}_e) - n(\mu_e\vec{v}_i - \mathbf{v}_e\vec{v}_n) \end{aligned}$$

Separating into the parallel and perpendicular (of  $\vec{B}$ ) components, the parallel components are given by:

$$\begin{aligned} (\vec{v}_e - \vec{v}_n)_\parallel &= -\frac{e}{m_e v_{en}} \vec{E}_\parallel + \frac{1}{v_{en} n} \vec{T}_{e\parallel} \\ (\vec{v}_i - \vec{v}_n)_\parallel &= -\frac{e}{m_i v_{in}} \vec{E}_\parallel + \frac{1}{v_{in} n} \vec{T}_{i\parallel} \quad (\text{Equation 2.15}) \end{aligned}$$

The perpendicular components are given by:

$$\begin{aligned} (\vec{v}_e - \vec{v}_n)_\perp &= \frac{e}{m_e} \left[ -\frac{v_{en}}{\omega_{ce}^2 + v_{en}^2} (\vec{E}_\perp + \vec{v}_n \times \vec{B}) - \frac{\omega_{ce}}{\omega_{ce}^2 + v_{en}^2} \hat{b} \times (\vec{E} + \vec{v}_n \times \vec{B}) \right] \\ &+ \frac{v_{en}}{\omega_{ce}^2 + v_{en}^2} \frac{1}{n} \vec{T}_{e\perp} + \frac{\omega_{ce}}{\omega_{ce}^2 + v_{en}^2} \frac{1}{n} \hat{b} \times \vec{T}_e \\ (\vec{v}_i - \vec{v}_n)_\perp &= \frac{e}{m_i} \left[ -\frac{v_{in}}{\omega_{ci}^2 + v_{in}^2} (\vec{E}_\perp + \vec{v}_n \times \vec{B}) - \frac{\omega_{ci}}{\omega_{ci}^2 + v_{in}^2} \hat{b} \times (\vec{E} + \vec{v}_n \times \vec{B}) \right] \\ &+ \frac{v_{in}}{\omega_{ci}^2 + v_{in}^2} \frac{1}{n} \vec{T}_{i\perp} + \frac{\omega_{ci}}{\omega_{ci}^2 + v_{in}^2} \frac{1}{n} \hat{b} \times \vec{T}_i \quad (\text{Equation 2.16}) \end{aligned}$$

Then, using  $\vec{E}' = \vec{E} + \vec{v}_n \times \vec{B}$ , one obtains Ohm's Law: (Note that the reference frame is the rest frame of the neutrals.)

$$\begin{aligned} \vec{j} = & \sigma_p \vec{E}'_\perp + \sigma_h \hat{b} \times \vec{E}' + \sigma_0 \vec{E}'_\parallel - \frac{v_{en}}{\omega_{ce}^2 + v_{en}^2} e \vec{T}_{e\perp} + \frac{v_{in}}{\omega_{ci}^2 + v_{in}^2} e \vec{T}_{i\perp} \\ & - \frac{\omega_{ce}}{\omega_{ce}^2 + v_{en}^2} e \hat{b} \times \vec{T}_e - \frac{\omega_{ci}}{\omega_{ci}^2 + v_{in}^2} e \hat{b} \times \vec{T}_i \quad (\text{Equation 2.17 Ohm's Law}) \end{aligned}$$

where

$$\sigma_p = \frac{en}{B} \left( \frac{v_{en} \omega_{ce}}{\omega_{ce}^2 + v_{en}^2} + \frac{v_{in} \omega_{ci}}{\omega_{ci}^2 + v_{in}^2} \right)$$



$$\sigma_h = \frac{en}{B} \left( \frac{\omega_{ce}^2}{\omega_{ce}^2 + \nu_{en}^2} - \frac{\omega_{ci}^2}{\omega_{ci}^2 + \nu_{in}^2} \right)$$

$$\sigma_0 = \frac{en}{B} \left( \frac{\omega_{ce}}{\nu_{en} + \nu_{ei}} + \frac{\omega_{ci}}{\nu_{in}} \right)$$

These are the Pedersen, Hall, and parallel conductivities.

### Relevant Scale Sizes and Model Limitations

Model results are valid over a certain range of spatial and time scales. This section describes the spatial and temporal scales employed in the model. Model limitations are also discussed.

The relevant physical length scales are the ion inertial scale ( $\sim 50$  km at 100 km above the Earth's surface), and the electron inertia length ( $= \left( \frac{m_e}{m_i} \right)^{\frac{1}{2}} \frac{c}{\omega_{pi}} \sim 4.67$  km). (The electron inertia is neglected.) Note that the ion skin depth is given by

$$\omega_{pi} = \left( \frac{4\pi n_i Z^2 e^2}{m_i} \right)^{\frac{1}{2}} = 1.32 \times 10^3 Z \mu^{\frac{1}{2}} n_i^{\frac{1}{2}} \frac{\text{rad}}{\text{sec}},$$

where  $\mu \left( = \frac{m_i}{m_p} \right)$  was chosen at  $\frac{1}{12}$  (carbon);  $n_i$  was chosen at  $10^5 \text{ cm}^{-3}$ . The ion

inertia scale can easily be resolved by the parallel model. It could only have been marginally resolved by the serial code. The electron inertial length (skin depth) can marginally be resolved by the parallel model (Inclusion by four or more grid points at 1 km/grid point resolution—comfortably resolved by later runs with the parallel model). However, since temporal changes associated with electron inertia are even faster than the subsecond scales considered here, electron inertia is

neglected in the model (**Equation 2.3**). This enabled the study of micro-scale physics in the ionosphere and lower magnetosphere on very small spatial and temporal scales.

Including the ion inertia, and not assuming a steady-state condition, enables the model to reproduce small-scale ionospheric processes, e.g. the formation of a field-aligned current layer. This is essential to the description of the formation and evolution of discrete aurora. The model can also reproduce Alfvén wave propagation—and the height-dependent collision frequencies can reproduce realistic ionospheric conductances (and thus Alfvénic reflections).

The three-fluid (electrons, ions, neutrals) approach enables the simulation of ionospheric (i.e. Hall/Pederson) currents—and thus current closure, via Pedersen currents, in the lower ionosphere. The model can also simulate realistic small-scale heating processes. The treatment of all ions as singly-charged ions, of height-dependent mass, however, cannot reproduce those quantities—which would require a multi-fluid approach.

Please note that the “base IDL routines” were originally developed by Antonius Otto. Dr. Otto also wrote the IDL code that checked for Alfvénic perturbations (Chapter 3). Dr. Otto also wrote the IDL routines which show the 3-D current sheet deformations (**Figure 3.9** and **Figure 3.23**).

An extant, serial, 3-dimensional code was explicitly parallelized—for any arbitrary, 1-dimensional domain scheme. The nature of this code is laid out in

express detail in this chapter and the first four appendices. No additional physics was added to the model (save for a new Joule heating routine)—however, the *vastly* increased system sizes, made possible by the parallelization, allowed for the addressing of new problems.

The explicit parallelization of a very complex (coupled partial differential equations) extant code, for a generalized parallelization scheme, and a generalized (but still orthogonal) grid—as well as the development of a routine to automatically calculate the Joule heating, for a generalized set of scale sizes, are entirely new contributions. Both represent significant achievements in both code design and implementation.

In this work, every effort has been made in the model to capture the relevant physics behind the questions in hand. The model supplies a consistent, complete description of the problems addressed in the thesis. The model shows—qualitatively—(and semi-quantitatively) some of the features of discrete auroral arcs, including narrow arc formation, fast plasma flows in the region of discrete arcs, and the formation and maintenance of a parallel (to the magnetic “guide field”) electric field. The model also investigated the Joule heating over multiple length scales, in the region of discrete aurora.

## **Chapter 3 Alfvénic Model Physics and Implementation Details**

### **Introduction and Motivation**

The formation and time evolution of discrete auroral arcs has been one of the most enduring problems of auroral physics. Unresolved issues are the narrowness of arcs, current sheet structures above the arcs, electric fields extending parallel outwards from the arcs, fast (plasma) flows in the region of discrete arcs, and the formation and maintenance of parallel electric fields—deep into the ionosphere.

In this chapter, we discuss a potential mechanism for the formation and time-evolution of discrete auroral arcs. It is shown that this model qualitatively—and semi-quantitatively—reproduces, in a self-consistent manner, many of the properties of discrete aurora.

The review of accelerator and generator mechanisms that follows indicates several issues insufficiently addressed or integrated in the research literature. These include the thinness of arcs (around 100 m in thickness, although arcs of less than 70 m are extant); fast plasma flows, at speeds up to 90 km/s, at a height of 110 km above the Earth's surface (Vogt, 1999); and the formulation and maintenance of parallel electric fields deep into the ionosphere. Discrete aurora have streams of electrons of approximately 10 keV energies, in a very narrow spectrum (McIlwanin, 1960). These streams of electrons are accelerated by parallel electric fields, which penetrate deep into the ionosphere (Lysak, 1990).

Theories on the formation of auroral arcs abound in the literature. For this chapter, they have been separated into auroral arc generator mechanisms, and electron-acceleration mechanisms.

### **Accelerator Mechanisms**

The following is a breakdown of theories for the mechanisms believed responsible for the acceleration of electrons into the region of formation for auroral arcs. Electrons are accelerated along magnetic field lines, which pass into the auroral region.

a) Static magnetosphere-ionosphere coupling (Lyons 1980; Lyons 1981; Kan and Lee 1980; Chiu and Cornwall 1980; Lee and Kan 1981; Chiu, Newman, and Cornwall 1981; Goertz 1985; Weimer, Goertz, Gurnett, Maynard, and Burch 1985)

In the theory of static magnetosphere-ionosphere coupling, a perpendicular electric field in the magnetosphere causes the production of a current loop that closes in the ionosphere. For the formation of an auroral arc, a parallel potential must develop along field lines (to have currents flowing down and back through the magnetosphere), while a potential must develop perpendicularly to the field, in order to get currents to flow in the ionosphere.

b) Particle anisotropies in the dipole magnetic field (Alfvén and Fälthammar 1963; Persson 1963; Persson 1966; Lennartsson 1976; Lennartsson 1977; Ponyavin, Pudovkin, and Sazhin 1977)

If one assumes that ions and electrons have a different pitch angle distribution in the magnetosphere, then they will be reflected (mirrored) at different locations in the ionosphere. This will produce an ambipolar separation in the charge, and a resultant electric field. Note that the ions (mirroring after the electrons) must have sufficient energy to cross this electric field.

c) Thermoelectric contact potential (Hultqvist 1971)

When two regions of plasma at different temperatures come into contact with each other, an electric field forms between them, because of the loss of electrons from the warmer plasma to the cooler plasma. This has been proposed as a theory for the formation of auroral electric fields.

d) Strong plasma double layers (Albert and Lindstrom 1970; Carlqvist and Bostrom 1970; Block 1972; Block 1978; Gurnett 1972; Hubbard and Joyce 1979)

Sometimes, regions of strong electric fields form in a collisionless plasma, in regions where current is flowing. It has been put forward that these regions—called “double layers”—may provide the driving force for the acceleration of auroral electrons.

e) Electrostatic shocks (Swift 1975; Swift 1976; Swift 1979a; Hudson and Mozer 1978; Hudson and Potter 1981)

Very similar to the theory of double layers as means of accelerating auroral electrons, the electrostatic shocks treatment differs only in the solution of the

Poisson-Vlasov equations. They are solved with the restriction that the spatial gradient of the layers is small, in relation to the gyroradii.

f) Ion-acoustic double layers (Lotko and Kennel 1983; Hudson, Lotko, Roth, and Witt 1983; Hudson, Crystal, Lotko, and Barnes 1987; Bujarbarua and Goswami 1985; Lotko 1986; Prakash and Lysak 1992)

In the theory of ion-acoustic double layers, there are localized regions of drops in potential. It is believed that electrons gain energy by passing downward through successive regions of these drops.

g) Kinetic (oblique) Alfvén waves (Hasegawa and Chen 1976; Goertz and Boswell 1979; Leontyev and Lyatskiy 1980; Lysak and Carlson 1981; Dungey 1982; Lysak and Dum 1983)

From the wave polarization:

$$\frac{E_{\parallel}}{E_{\perp}} = \frac{\frac{\partial \phi}{\partial x_{\parallel}} + \frac{1}{c} \frac{\partial A_{\parallel}}{\partial t}}{\frac{\partial \phi}{\partial x_{\perp}}} - \frac{k_{\parallel}}{k_{\perp}} \left[ \frac{\lambda_e^2 k_{\perp}^2}{1 + \lambda_e^2} \right]$$

(Equation 3.1 Wave Polarization Equation)

One can see in the limit of perpendicular wavelengths becoming much larger than the electron inertial length, the parallel electric field vanishes. As the limit of the perpendicular wavelength approaches zero, the wave becomes electrostatic.

Therefore, as the waves travel further into the ionosphere (waves less able to oscillate, due to friction with the neutrals), these conditions require fine structure (Swift 2007).

h) Electromagnetic ion-cyclotron waves (Temerin, McFadden, Boehm, Carlson, and Lotko 1986; Temerin and Cravens 1990)

The theory of electromagnetic ion-cyclotron waves is similar to the that of the oblique Alfvén wave model (above). Mainly, that a parallel electric field forms for a parallel  $k$  vector greater than zero. However, in the oblique Alfvén model electrons are accelerated impulsively; where in the electromagnetic ion-cyclotron waves accelerate model electrons are accelerated more slowly, in a manner similar to that of a linear accelerator.

i) Anomalous resistivity (Palmadesso, Coffey, Osakow, and Papadopoulos 1974; Ionson, Ong, and Fontheim 1976; Mozer 1976; Papadopoulos 1977; Galeev 1983; Stasiewicz 1984)

In the theory of anomalous resistivity, the momentum of drifting electrons is transferred to ions in a plasma. This produces a resistive electric field. It is believed that electrons are accelerated by such a [magnetic] field-aligned electric field. Coulomb collisions provide too weak a mechanism for arc formation. However, scattering by plasma waves may provide enough momentum transfer for this mechanism to function.



j) Lower-hybrid-wave Landau resonances (Bingham, Bryant, and Hall 1984; Bingham, Bryant, and 1988; Bryant, Hall, and Bingham 1991; Bryant, Cook, Wang, de Angelis, and Perry 1991)

As a potential accelerator mechanism for auroral arc formation, it is proposed that electrons are accelerated by Landau resonances with a range of lower-hybrid waves. For this to occur, the lower-hybrid waves would have to have field aligned phase velocities that exceed the electron-thermal speed. Such a spectrum of waves would Landau resonate with electrons traveling at suprathermal velocities.

k) Electron precipitation induced by auroral kilometric radiation (Calvert 1982; Calvert 1987)

In the theory of auroral kilometric radiation, it is proposed that sufficiently energetic electrons in the magnetosphere are deflected into the ionosphere by pitch-angle scattering. The mechanism is believed to be standing electromagnetic waves in density cavities; these waves are often referred to as auroral kilometric radiation.

l) Lower-hybrid-wave broadened DC electrostatic structure (Smith 1986a; Smith 1986b; Smith 1987)

In the lower-hybrid-wave broadened DC electrostatic structure model, it is put forth that cross-(magnetic) field currents induced by lower-hybrid-wave turbulence broaden the current channel within a potential structure.

### **Generator Mechanisms**

In this section, generator mechanisms (mechanisms that are proposed to generate an electric field along magnetic field lines which pass into the auroral region) are discussed.

m) Shear in the low-latitude boundary layer (Eastman, Hones, Barne, and Asbridge 1976; Sonnerup 1980; Bythrow, Heelis, Hanson, Power, and Hoffman 1981; Heikkila 1984; Lundin and Evans 1985; Lotko, Sonnerup, and Lysak 1987)

If plasma is flowing across a magnetic field, the associated inertia of the flow can function as a (MHD) generator. This can produce electrical currents, where the flow is sheared across field lines. It has been proposed that the Earth's low-latitude boundary layer maps to the polar regions, and these flows are driving auroral currents.

n) Shear in the plasma sheet (Rostoker and Bostrom 1976; Hasegawa and Sato 1979; Birn and Hesse 1991; Birn, Hesse, and Schindler 1992)

Similarly, it has been proposed that flows in the plasma sheet can function as an (MHD) generator, due to their inertia. It is theorized that this can drive field-aligned currents from the region of the current sheet.

o) Magnetic-field-line reconnection (Akasofu, Chapman, and Kendall 1967; Sato and Iijima 1979; Atkinson, Creutzberg, and Gattinger 1989; Atkinson 1992)

Reconnection in the magnetotail may drive auroral currents. This may be a mapping to X-type reconnection field lines, or to the compression from the outflows from the reconnection region.

p) Poynting-flux absorption on a resonance layer in the outer edge of the plasma sheet (Goertz 1983; Goertz 1984; Goertz 1990; Harrold, Goertz, Smith, and Hansen 1990)

It has been proposed that magnetosonic waves can be produced by the solar wind transferring its kinetic energy to the magnetosphere. Then, Alfvén waves are produced across density gradients on the surface of the plasma-sheet. This is believed to be a resonant process, driven by the conversion of magnetosonic wave energy, by a resonant conversion of magnetosonic wave energy. Then, Alfvén waves transfer their energy to kinetic energy of particles, driven by electric fields along the [magnetic] field lines.

q) Ionospheric-conductivity feedback instability (Ogawa and Sato 1971; Sato and Holzer 1973; Sato 1978; Lysak 1986; Lysak 1991; Watanabe and Sato 1988)

It has been theorized that a patch of enhanced conductivity may form between a downward (towards the Earth's surface) and upward traveling

ionospheric currents. It is believed that the conductivity will increase with current flow, developing over time into an auroral arc.

r) Earthward ion streams in the plasma-sheet boundary layer (Kan 1975; Kan and Akasofu 1976; Lui, Hones, Yasuhara, Akasofu, and Bame 1977; Lyons and Evans 1984; Lyons 1991)

High-energy ions follow in narrow structures along field lines, originating from the plasma-sheet boundary layers. It has been put forward that perhaps these ions are transferring their energy to electrons through an electrostatic potential structure, resulting in the formation of auroral arcs.

s) Earthward electron streams in the plasma-sheet boundary layer (Onsager, Thomsen, Elphic, and Gosling 1991)

Similarly, it has been theorized that electron beams of high energy ( $\sim 10$  keV), streaming from the outer edges of the plasma-sheet, can result in the formation of auroral arcs. This is believed to occur from either conversion of the electron stream to kinetic energy by means of an electrostatic potential structure, or by direct precipitation.

t) Pressure gradients in the plasma sheet (Vasyliunas 1970b; Kern 1967; Block 1984; Galperin and Volosevich 1989; Galperin, Volosevich, and Zelenyi 1992)

A current along the [magnetic] field line will result from a gradient in the particle pressure perpendicular to a gradient in the magnetic induction (with the

further requirement that both gradients are perpendicular to the guide field). It has been put forward that by this mechanism, gradients in the magnetosphere may produce auroral arcs.

u) Electrostatic fluid turbulence in the plasma sheet (Swift 1977; Swift 1979b; Swift 1981a; Swift 1981b; Lotko and Schultz 1988; Song and Lysak 1988)

It is believed that electrostatic  $\vec{E} \times \vec{B}$ -drift spawned turbulence behaves in a similar fashion to two-dimensional Navier-Stokes turbulence in the magnetosphere. When energy is transferred into the magnetosphere, at differing plasma spatial scales, this will result in growing of eddies of a specific size. Swift argued that arcs formed by these mechanisms would be isotropic, and not aligned in an east-west configuration.

v) Earthward plasma flow into a high-conductivity zone (Rothwell, Silevitch, Block, and Falthammar 1991)

In this model, the auroral arc produces a region of high conductivity, into which plasma streams. The auroral arc uses as its source of energy the kinetic energy of plasma flowing from the plasma-sheet.

## **Discussion of Models**

None of the models above provide a complete, consistent description for the formation and evolution of discrete auroral arcs. They fail to account for the thinness of aurora arcs by at least an order of magnitude (Borovsky 1993). A new theory is needed.

Alfvén waves are the primary means of communicating information from the ionosphere to the magnetosphere (and vice versa). In the following sections, a model is developed which shows that the edges of the current sheet (part of the formation mechanism of discrete arcs expounded) is formed by magnetic shear, and deformed by Alfvénic perturbations on its surface. The model shows—qualitatively—(and semi-quantitatively) some of the features of discrete auroral arcs, including narrow arc formation, fast plasma flows in the region of discrete arcs, and the formation and maintenance of a parallel (to the magnetic “guide field”) electric field.

### **Simple Alfvén Wave**

In order to investigate our premise that Alfvén waves play in the generation and time evolution of discrete arcs, we first consider the idealized case of an “infinite (Alfvénic) wave train,” reflecting from the ionosphere. Such a derivation will be used extensively in making quantitative measurements of Alfvén waves from the ionosphere.

As a first approximation in the modeling of an Alfvénic reflection, the behavior of an infinite wave train normally incident on the ionosphere is considered. The scheme is outlined in Figure 3.1. Infinite wave trains of velocity and magnetic perturbations travel down from the top of the figure. Then, in three “snapshots” of time, their behavior is shown. Note that the velocity and magnetic perturbations reflect in different directions. This is permissible for an Alfvén wave; perturbations in the magnetic field may be positive or negative.

### Derivation of the Reflection Coefficient

Derived below is the reflection coefficient for an infinite Alfvén wave train, normally incident upon the ionosphere. This relation will make quantitative measurements of Alfvénic reflections in the general case. (For a complete derivation, see Scholer, 1970.)

Assuming an incoming “infinite wave train” (of constant magnitude), one has:

For the incoming wave:

$$\delta B_y = B_i$$

$$\delta v_y = v_i$$

$$v_i = \frac{B_i}{B_x} v_A$$

Where  $\delta B_y$  and  $\delta v_y$  are the magnetic and velocity perturbations in y, respectively,

and the i and o subscripts denote the incoming and outgoing wave. The velocity with the A subscript denotes the Alfvén speed. See Fig. 3.1.

For the outgoing wave:

$$\begin{aligned}\delta B_y &= B_0 \\ \delta v_y &= v_0 \\ v_0 &= -\frac{B_0}{B_x} v_A\end{aligned}$$

(The minus sign is a due to the change in wave propagation direction.)



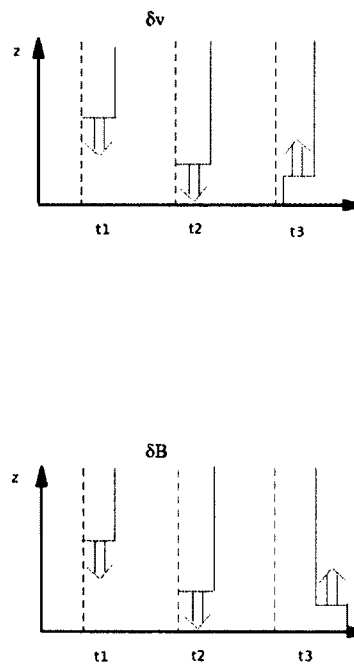


**Figure 3.1 Alfvén Reflection (After Fig. 3 in Zhu, Otto, Lummerzheim, Rees and Lanchester 2001)**

The Pederson current (which closes currents in the ionosphere), is defined as:

$$\vec{j} = \sigma_p \vec{E}$$

Integrated:

$$\vec{I} = \Sigma_p \vec{E}$$

$$\vec{I}_p = \int \vec{j} dz$$

$$I_{px} = -\frac{1}{\mu_0} B_y$$

With direction(s) determined from  $\nabla \times \vec{B} = \mu_0 \vec{j}$  ( $j_z = \frac{1}{\mu_0} \frac{\partial}{\partial x} \delta B_y$ ). Please note that

for a perfectly conducting ionosphere,  $\delta v = v_{in} + v_{out} = 0$ .

$$I_z = \int j_z dx = \frac{1}{\mu_0} \int \frac{\partial B_y}{\partial x} dx = \frac{1}{\mu_0} (\delta B_y|_{(2)} - \delta B_y|_{(1)})$$

$$I_{p,z} = \frac{1}{\mu_0} (B_i + B_0)$$

$$= \Sigma_p (E_{zi} + E_{z0})$$

$$= \Sigma_p B_x (v_i + v_0)$$

Note:  $\vec{E} = \vec{v} \times \vec{B}$

Substituting for  $v_i, v_0$  gives:

$$B_i + B_0 = \mu_0 v_A \Sigma_p (B_i - B_0) \quad (\text{Equation 3.2})$$

$$\text{Note: } v_i = \frac{B_i}{B_x} v_A, \quad v_0 = -\frac{B_0}{B_x} v_A$$

or

$$B_0 = \frac{\mu_0 v_A \Sigma_p - 1}{\mu_0 v_A \Sigma_p + 1} B_i$$

$$\frac{B_o}{B_i}(= r) = \frac{\Sigma_p - \frac{1}{\mu_o v_A}}{\Sigma_p + \frac{1}{\mu_o v_A}}$$

Where  $\mu_o v_A$  is the ‘‘Alfvénic impedance.’’

### Diagnostic

From Equation 3.2 and using  $\vec{E} = \vec{v} \times \vec{B}$ :

$$\frac{\Delta v / v_A}{\Delta B / B_o} = \frac{1}{\mu_o \Sigma_p v_A}$$

Which can be rearranged as:

$$\frac{\Delta v}{\Delta B} = \frac{1}{\mu_o \Sigma_p B_o}$$

Or:

$$\Sigma_p = \frac{1}{\mu_o B_o} \frac{\Delta B}{\Delta v}$$

Thus, the Pedersen Conductivity is uniquely defined by the ratio of  $\frac{\Delta v}{\Delta B}$ . Note that while this condition holds even for Alfvén waves propagating through the system, it is violated (does not hold) for regions where field-aligned currents exist. Figures 3.3a and 3.3b show a snapshot of this ratio of the velocity in the z-direction, over the magnetic field in the z-direction (color code). This ratio is shown to be constant, in all regions save those which contain the field-aligned current.

### Reconnection Region

At the start of the simulation run, an initial perturbation in the form of a region of transient resistivity is turned on in a small, localized area. This causes a

region of patchy reconnection to form (c.f. **Fig. 3.3**). This “reconnection region” has the form of:

$$\frac{1}{\cosh^2\left(\frac{z-95}{5}\right)} \left[ \frac{1}{\cosh^2\left(\frac{y}{2}\right)} + \frac{1}{\cosh^2\left(\frac{y-y_{\max}}{2}\right)} \right]$$

Multiplied by the “time factor” of:

$$4\eta \exp\left(-\frac{t}{4}\right)$$

Where  $\eta$  is the resistivity (0.05) and  $t$  is the time.

The resulting parallel electric field from this reconnection results in currents that turn on a current-dependent resistivity. The reconnection region is maintained by these existing currents. In fact, the region grows in size over time. The magnetic shear provides the source of free energy—in addition to the shear flow, applied at the top of the system. Magnetic shear is generated through shear flow in the simulation. An initial field-aligned current layer is assumed and shear flow imposed at the top boundary is used to generate additional Poynting flux, which intensifies the current layer (and magnetic shear) in the absence of dissipation.

Possible physical explanations for this initial localized electric field component parallel to the magnetic field are

- a) double layers (Block 1975; Swift 1975; Lee and Kan 1981)
- b) electrostatic shocks (Kan 1975)

c) particle inertia (Seyler 1990)

Consider the condition of a superconductor. If either a maximum current value is exceeded, or there is too rapid a change in the current value, the superconductivity is lost. The magnetosphere is a superconducting plasma; the presence of this initial localized electric field component corresponds to too fast a flow resulting in a loss of this superconductivity. The system has become “choked.”

In this model, progressive reconnecting of field lines at increasing distance from the initial current layer causes the spreading of the auroral arcs. The detailed mechanism of this process is examined in detail later in this chapter.

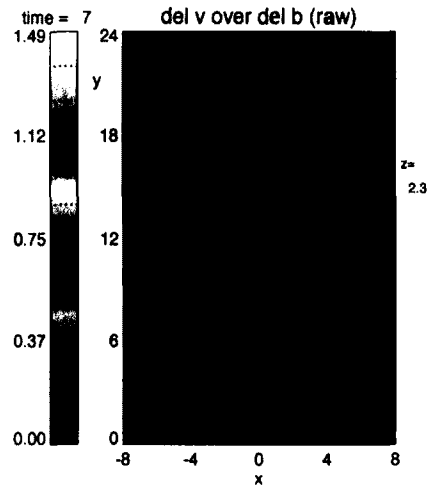


**Figure 3.2a Velocity Perturbations Over Magnetic Field Perturbations (Boundary Conditions A) for a Cut in the z-Plane at 230 km**

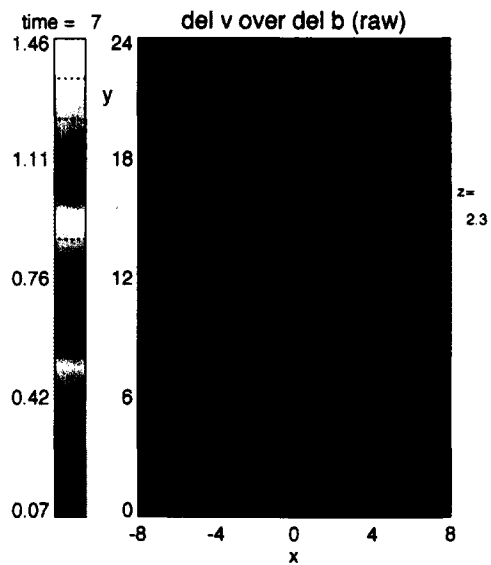


**Figure 3.2b Velocity Perturbations Over Magnetic Field Perturbations (Boundary Conditions B) for a Cut in the z-Plane at 230 km**

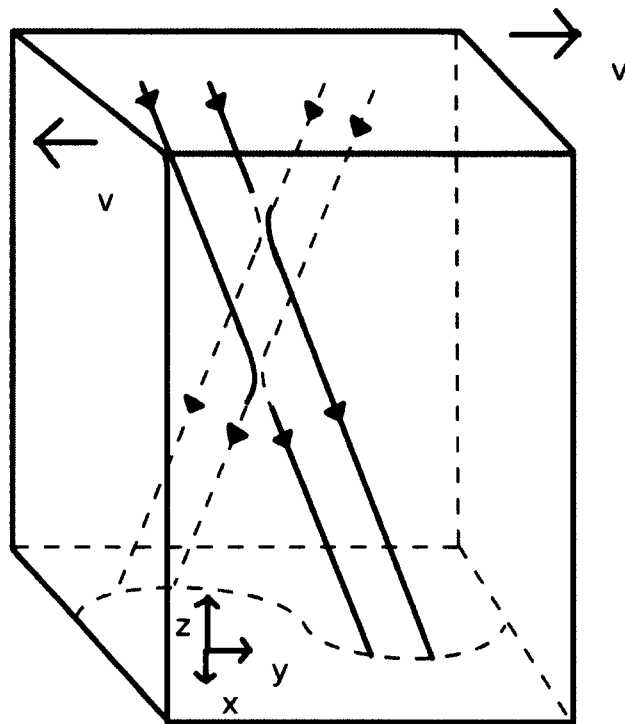


Figure 3.3 Reconnection Region (after Fig. 2a in Otto and Birk 1993)

### **Alfvén Wave Reflection**

Of primary importance is how currents close in the ionosphere. Further downward in the ionosphere, collisions with the neutrals increase. Eventually, collisions become so frequent, that ions—with their much larger gyroradius—can no longer complete their gyrations without (statistically) having a collision. As ions can no longer freely  $\vec{E} \times \vec{B}$  drift, they will start traveling along the electric field. This is the so-called Pedersen current.

Field-aligned currents are carried (mainly) by electrons. The Pedersen current is carried (mainly) by ions. Current is closed in the ionosphere by the Pedersen current.

For an Alfvén wave traveling downward into the ionosphere, eventually collisions with the neutrals will cause both (all) conductivities to fall too low (resistivities to rise too high) for the ions to freely move, and the wave will be reflected. Next, we discuss some practical issues in developing a computational simulation.

### **Boundary Conditions A**

Modification of the original boundary condition was required for the model, because the original way of handling the magnetic field at the lower boundary resulted in an unrealistically low ionospheric conductivity, which caused too rapid



flows to develop in the ionosphere—with resultant numerical instability. In this case, the components of the magnetic field were assumed symmetric.

### **Boundary Conditions B**

As mentioned above, a new way of treating the lower boundary of the simulation was required. At the mathematical [lower] boundary, the magnetic perturbations in x and y were set to zero ( $\delta B_x = \delta B_y = 0$ ).

Unfortunately, this change resulted in large fluxes into and out of grid points—and areas of low density. These large fluxes resulted in some of the areas of low density becoming areas of negative density—with resultant numerical instability.

This required the implementation of a new smoothing algorithm. The new algorithm only performs “local smoothing.” as opposed to the previous smoothing routine, which performed smoothing on the entire simulation domain. This enabled calling the smoothing algorithm more often—without “washing out” the relevant physics.

To obtain realistic ionospheric conductivities, the collision frequencies (of the ions with the neutrals) had to be increased. Note that this meant that the time step had to be decreased—in order to resolve the new shorter collision times.

Fig 3.4 shows the progressive Alfvén wave propagation from the upper boundary, and subsequent reflection from the lower boundary (for Boundary Conditions A). This figure shows a snapshot of velocity vectors and velocity in the z-direction (color code). One can see some “stirring” of the plasma at the bottom of the simulation domain, and a resulting (smaller) Alfvén wave being generated and moving upwards. This is a result of the system responding to a non-equilibrium situation—in the only way it can, by offsetting these conditions by the promotion of an electric field via plasma motion.

In Fig. 3.5, the Alfvén relation is shown. This figure shows a snapshot of the ratio of the velocity perturbations to the magnetic perturbations (color code). For a wave to be an Alfvén wave, the ratio of its velocity perturbations to its magnetic perturbations must be either plus or minus 1. (This is the Whalen relation.) The figure shows that the wave in question is clearly Alfvénic in character.

Fig 3.6 shows the progressive Alfvén wave propagation from the upper boundary, and reflection from the lower boundary—Boundary Conditions B. This figure shows a snapshot of the velocity vectors and velocity in the z-direction (color code).

One very notable difference of the evolution of the system from previous boundary conditions is the formation of an upward-traveling Alfvén wave. The

magnetic shear (an initial condition) creates the current sheet—which places the system in a non-equilibrium condition. The only way that this system can sustain this situation is by producing an electric field via plasma motion ( $\vec{E} = \vec{v} \times \vec{B}$ ).

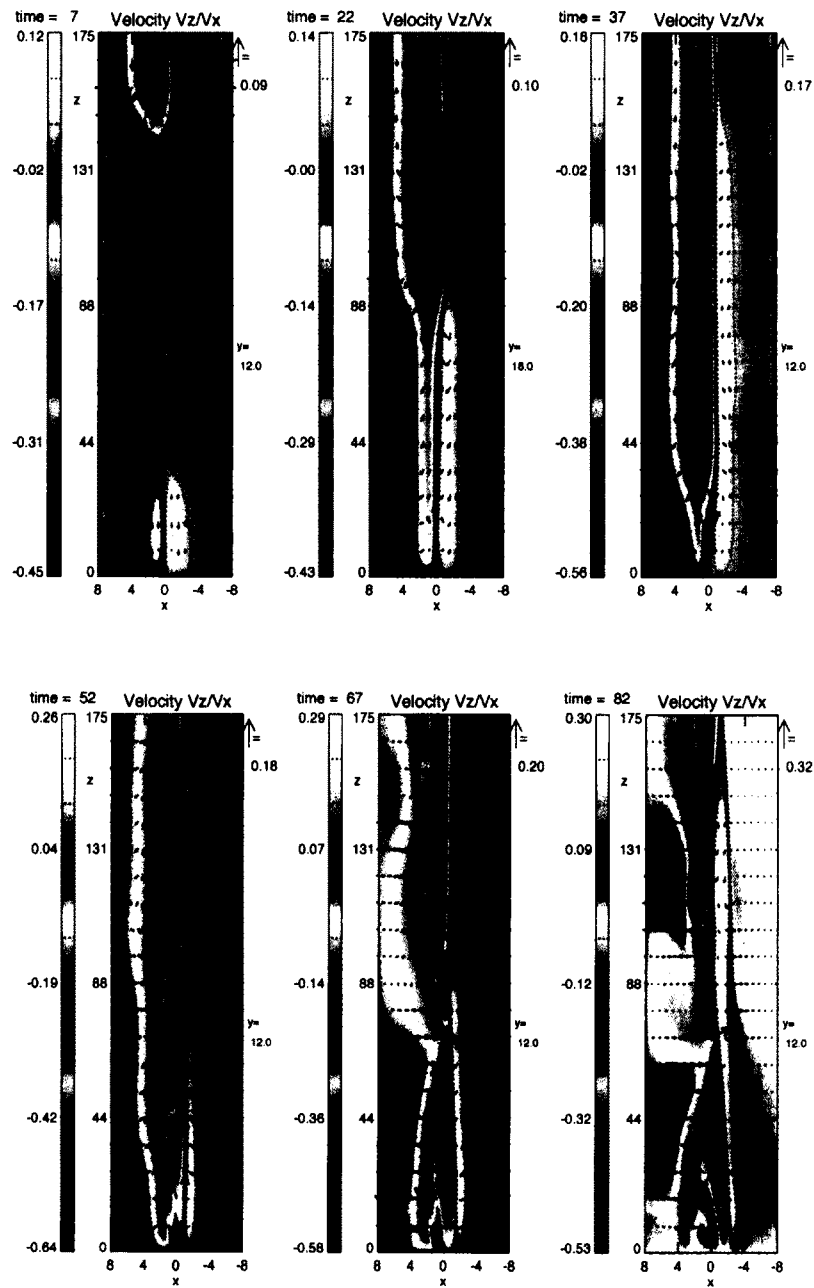


**Figure 3.4 Progression of an Alfvén Wave (Boundary Conditions A) at 7.5, 22.5, 37.5, 52.5, 67.5, and 82.5 Alfvén Times. Cuts Are Taken at 12 km in the y-Plane (Mid-Point)**

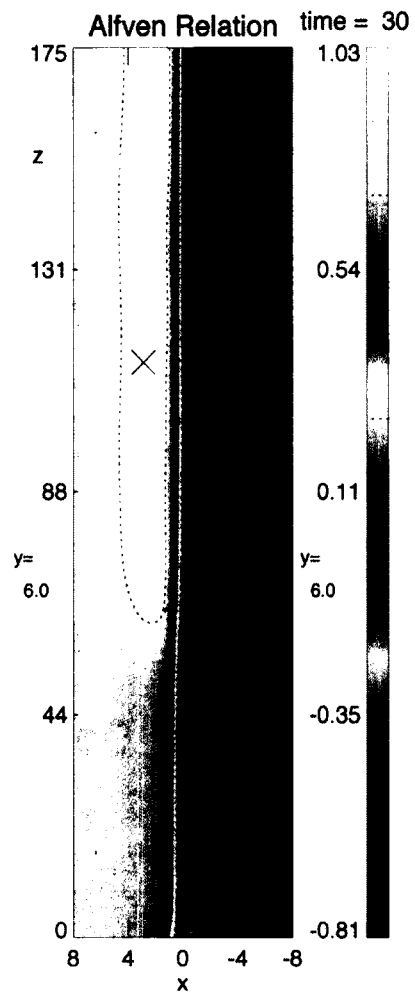


**Figure 3.5 The Alfvén Relation. The Alfvén Relation is Shown for 30 Alfvén Times, in the x-z Plane, at y = 6 km. This Shows That at a Value of +1, the Wave in Question is Definitely an Alfvén Wave.**

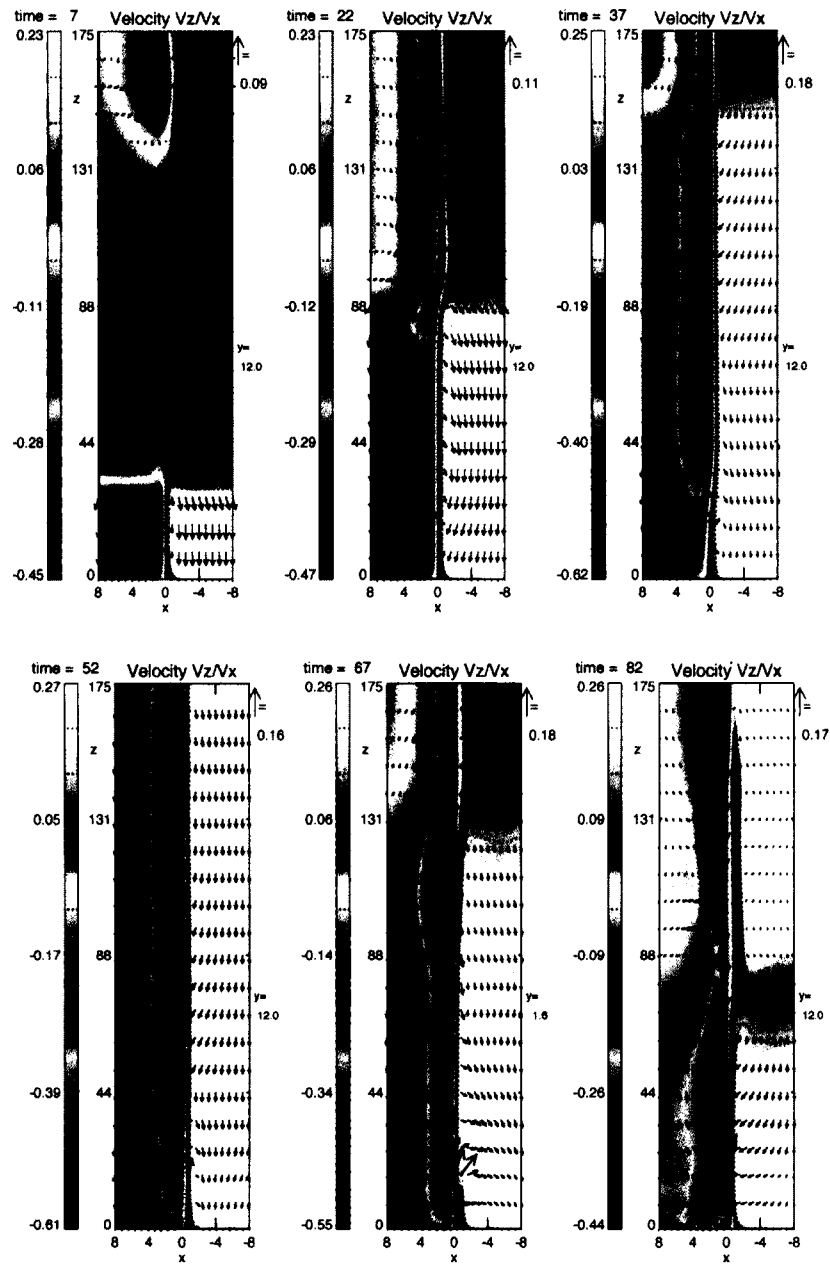


**Figure 3.6 Progression of an Alfvén Wave (Boundary Conditions B) at 7.5, 22.5, 37.5, 52.5, 67.5, and 82.5 Alfvén Times. Cuts Are Taken at 12 km in the y-Plane (Mid-Point)**

## Introduction to the Simulation

### Inventory of Runs

After the examination of a simple Alfvén wave formation and reflection we will now investigate the results of changing system parameters. Shown below is an inventory of the runs, used during the study. The parameters varied were the boundary conditions, the symmetry of the shear at the top of the simulation, the velocity of the shear prescribed at the top of the simulation, the collisions (of ions with the neutrals), and the plasma density.

For a detailed description of the motivation for altering the lower boundary conditions, c.f. Chapter 2. The symmetry of the shear at the top of the simulation domain was varied in order to investigate changes in “parity” of various properties in the simulation. (By an addition, or subtraction, of a constant value, the shear applied at the top of the simulation domain could be made to be either symmetric, or anti-symmetric (c.f. **Fig 2.1**.) The velocity of the shear applied at the top of the simulation box was altered in order to investigate the effects of differing the amounts of Poynting flux into the system (nominal value, in system units, was 0.5). Varying the collisions (of ions with the neutrals) and the (plasma) density was performed in order to investigate the changes this made in the height-integrated Pedersen conductivity (c.f. **Chapter 2**).

**Table 3.1 Inventory of Runs**

Sigma=1	Reference run—collisions, symmetry, shear all “nominal”
Old b.c.	Ideally conducting ionosphere, remaining parameters nominal
Sigma= 1 symmetry	Nominal collisions, symmetric velocity and magnetic shear
Sigma =1 velocity	Nominal collisions, nominal symmetric (asymmetric shear), heightened velocity shear (2x nominal)
Sigma=1.2 *	1.2x collisions, “older run”
Sigma=1.5 *	1.5x collisions, “older run”
Sigma=2 *	2x collisions, “older run”
Sigma=5	5x collisions
Sigma=5 symmetry	5x collisions, symmetric velocity shear
Sigma=5 velocity	5x collisions, enhanced velocity shear
Sigma=7.5 *	7.5x collisions, “older run”
Sigma=10	10x collisions, note that the time step had to be altered
density	Enhanced [plasma] density towards the bottom of the simulation—all other parameters nominal
* denotes “old data”	

Shown below is a table of the conductances, computed for the various runs in the study. Recall that:

$$\Sigma_p = \frac{1}{\mu_0 B_0} \frac{\Delta B}{\Delta v}$$

Note that these were measure at time step of 15 Alfvén times.



**Table 3.2 Computed Conductances**

	Time step	Delta v	B nought	Delta B	Delta v/ Delta B	R	Sigma Pedersen
Sigma=1	15	0.20435	4	0.78	0.26199	0.58479	0.95422
Sigma=1 symmetry	15	0.20440	4	0.78	0.26206	0.58470	0.95397
Sigma=1 velocity	15	0.20435	4	0.78	0.26199	0.58479	0.95421
Sigma=1.2*	15	0.18152	4	0.71	0.25567	0.59277	0.97781
Sigma=1.5*	15	0.15375	4	0.73	0.21062	0.65204	1.18696
Sigma=2*	15	0.12416	4	0.75	0.16555	0.71592	1.51009
Sigma=5	15	0.06414	4	0.92	0.06972	0.86964	3.58572
Sigma=5 symmetry	15	0.06414	4	0.92	0.06971	0.86965	3.58586
Sigma=5 velocity	15	0.06414	4	0.92	0.06972	0.86963	3.58538
Sigma=7.5*	15	0.04931	4	0.94	0.05245	0.90031	4.76568
Sigma=10	15	0.03942	4	0.94	0.04194	0.91948	5.96018
Density	15	0.16233	4	0.96	0.16909	0.71072	1.47843
* denotes "old data"							

**Basic Properties**

An imposed magnetic shear causes the formation of a current layer:

$$\vec{j} = \frac{1}{\mu_0} \nabla \times \vec{B}$$

Fig. 3.7 shows an idealized depiction of this shear. This shear results in the formation of the current sheet. Fig. 3.8 shows this magnetic shear, as viewed from above. As the magnetic shear has a “net curl,” this produces a current—the current sheet. The opposing magnetic shear serves as an “energy source” for the developing instability.

Fig. 3.9 shows the 3-D structures of deformation of the current sheet, for Boundary Conditions A—for 7.5, 15, 22.5, 30, 37.4, and 45 Alfvén times, respectively. The figure shows the equipotential surface of the current sheet, chosen phenomenologically. One can see in the first frame, the disturbance produced by the Initial Perturbation, and the Alfvén waves flowing away from it. Note that there is deformation of the current sheet without reconnection. The deformation of the current sheet, and enhanced reconnection (electric fields) in the vicinity are very similar to observations of actual discrete aurora. The remaining frames show the (ideal) reflection of the Alfvén wave from the top of the simulation domain.

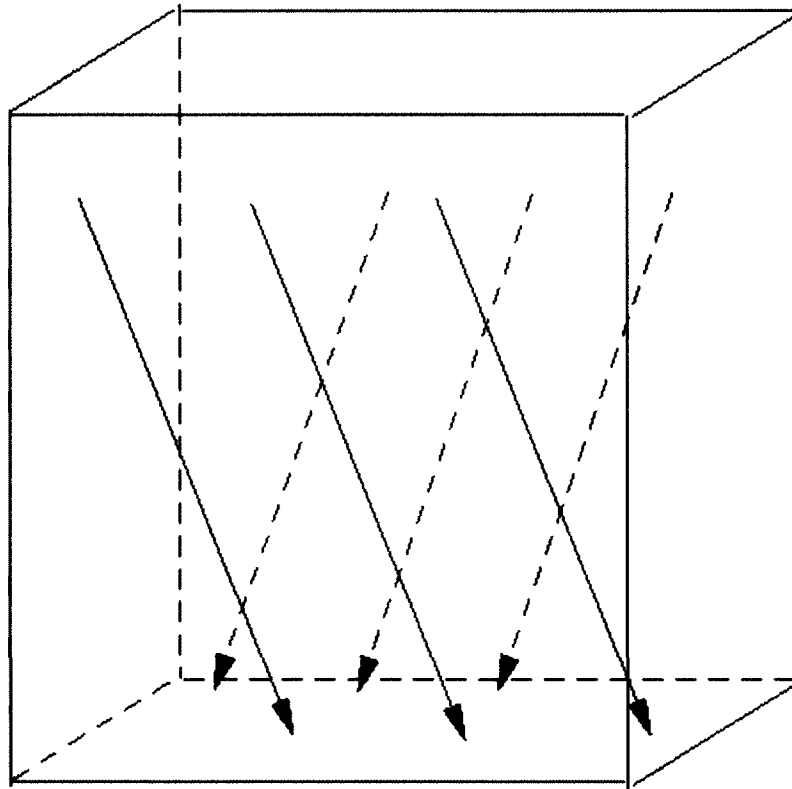


Figure 3.7 Magnetic Shear (3d View) (after Fig. 1 in Otto and Birk 1993)

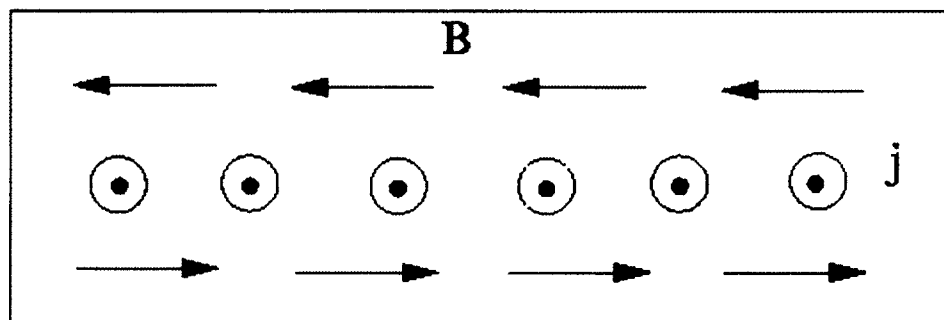
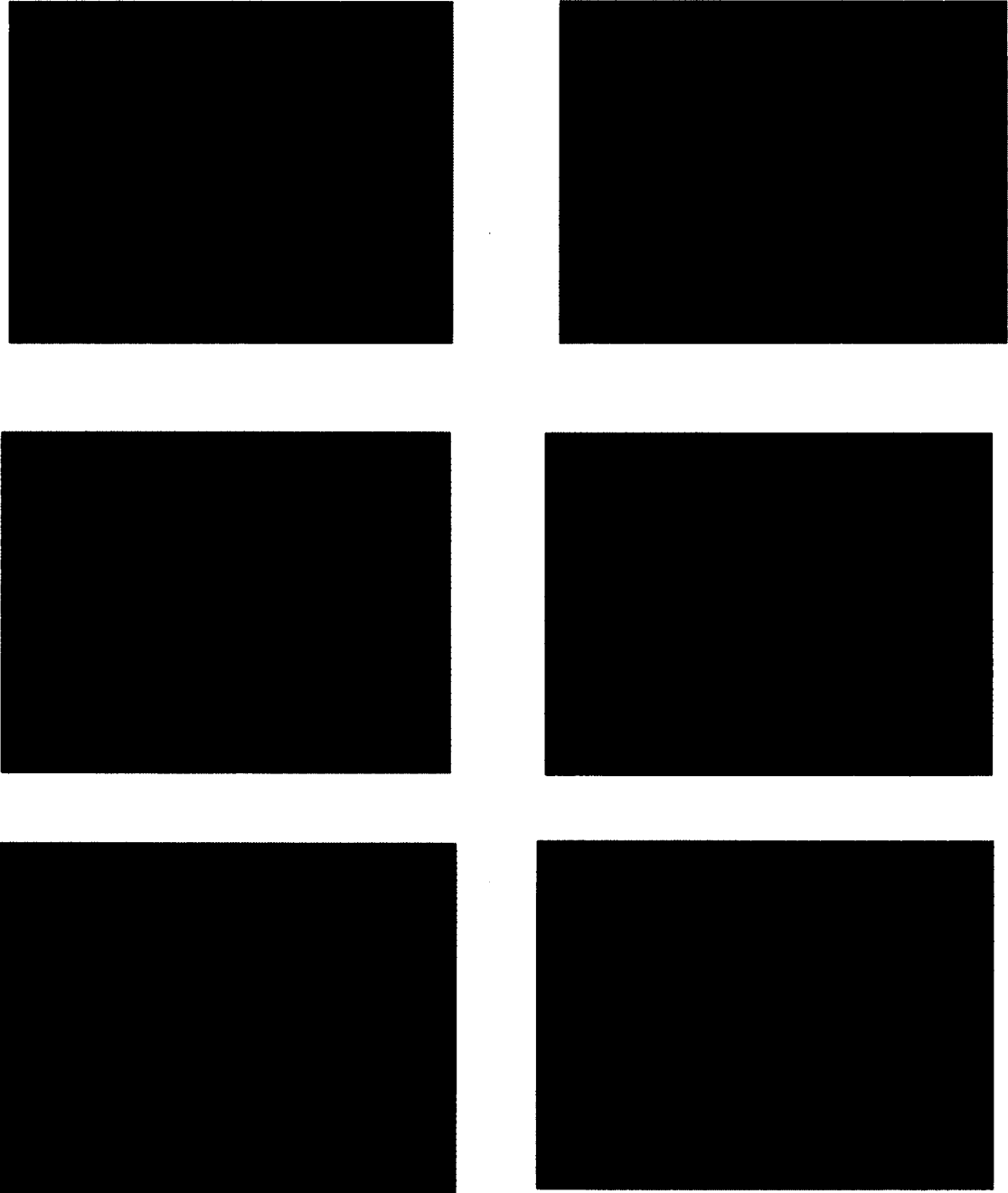


Figure 3.8 Magnetic Shear—Viewed From Above



**Figure 3.9 3-D Structures of Deformation of the Current Sheet, for Boundary Conditions A, for 7.5, 15, 22.5, 30, 37.5, and 45 Alfvén Times, Respectively. One Can See in the First Frame, the Disturbance Produced by the Initial Perturbation, and the Alfvén Waves Flowing Away From It. The Remaining Frames Show the (Ideal) Reflection of the Alfvén Wave From the Top of the Simulation Domain.**

Fig. 3.10 shows the idealized appearance of the reconnection region—both the magnetic field line configuration, and the velocity outflow. The magnetic field is in a classic “X-line” configuration, and there are strong velocity outflows to the sides. These are the hallmarks of magnetic reconnection (Otto, 1998).

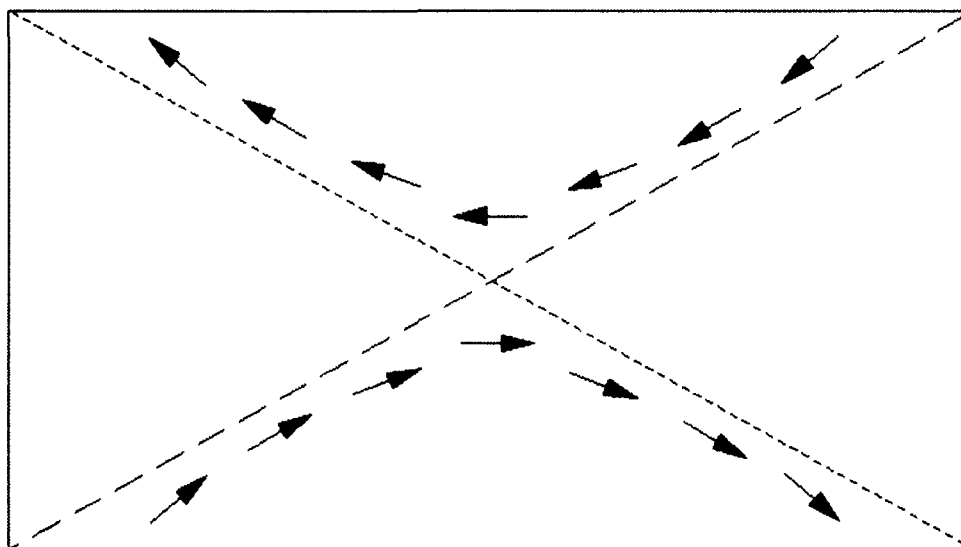
The appearance of the reconnection region can be seen in Fig. 3.11. This shows a snapshot of parallel electric field lines parallel electric field magnitude (color code) on the left, and parallel current field lines, and parallel current magnitude (color code). It is highly localized, and at a height of 5,980 km. Shown in Fig. 3.12 is the appearance of the reconnection region, integrated [through the entire simulation domain] in x. This figure shows a snapshot of (integrated) parallel electric field lines and (integrated) parallel electric field magnitude (color code) on the left, and (integrated) parallel current field lines and (integrated) parallel current magnitude (color code) on the left. Please note that the reconnection region has spread into two regions. The reconnection region moves downward, as the simulation progresses.

Fig. 3.13 shows the magnetic field in the region of reconnection region. This figure shows a snapshot of magnetic field vectors, and the magnitude of the magnetic field in the z-direction (color code). One can see an X-line developing. An

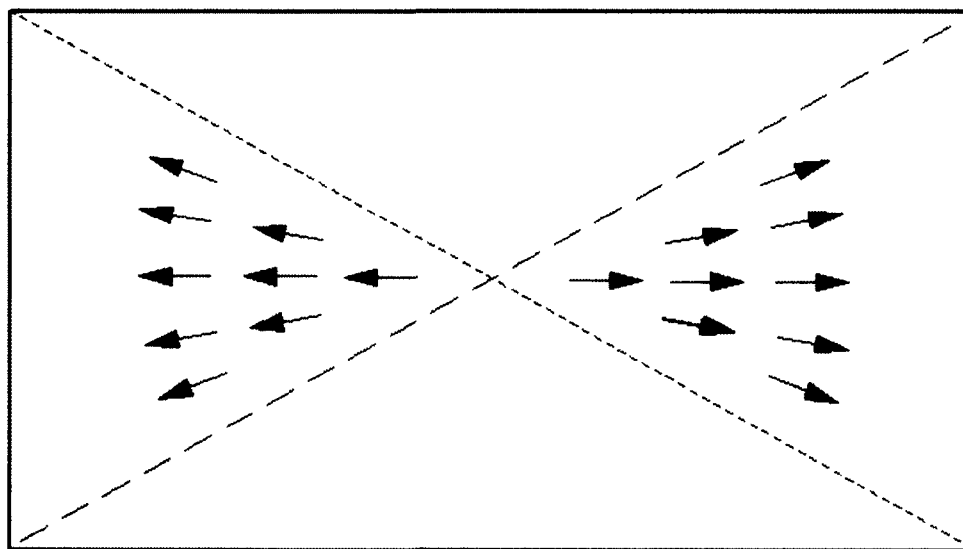
X-line is the (idealized) juncture of two magnetic field lines, undergoing reconnection. Fig. 3.14 shows the velocity perturbations in the region of the reconnection region. This figure shows a snapshot of velocity field vectors, and the magnitude of the velocity in the z-direction (color code). Notice the strong flows, above and below the reconnection region—consistent with magnetic reconnection.

Fig. 3.15 and Fig. 16 show the velocity perturbation and electric perturbations, respectively, in a z-plane—towards the bottom of the simulation domain, for the reference run, in the ionosphere. Figure 3.15 shows a snapshot of the velocity field vectors, and the magnitude of the velocity in the z-direction (color code). Figure 3.16 shows the electric field vectors, and the magnitude of the electric field in the z-direction (color code). These plots also show two very aurora-like features: The electric field spreading directly outward from a narrow [mostly electron] precipitation region—and a corresponding velocity shear (carried by the Alfvén waves) parallel to these thin precipitation regions. These behaviors closely resemble the electric and velocity fields near actual auroral arcs (Haerendel, Buchert, La Hoz, Raaf, and Rieger 1993).

### Magnetic Field Lines



### Velocity Outflow



**Figure 3.10 Idealized Appearance of the Reconnection Region (z-plane)**

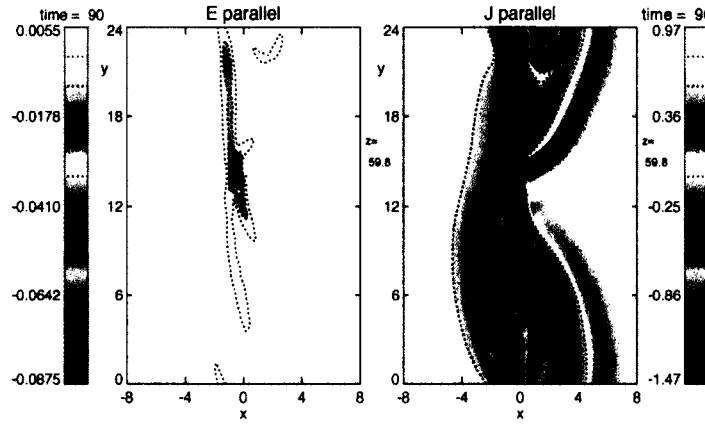


**Figure 3.11 The Appearance of the Reconnection Region (Reference Run). Cuts Are Taken in the z-Plane at 5,980 km.**

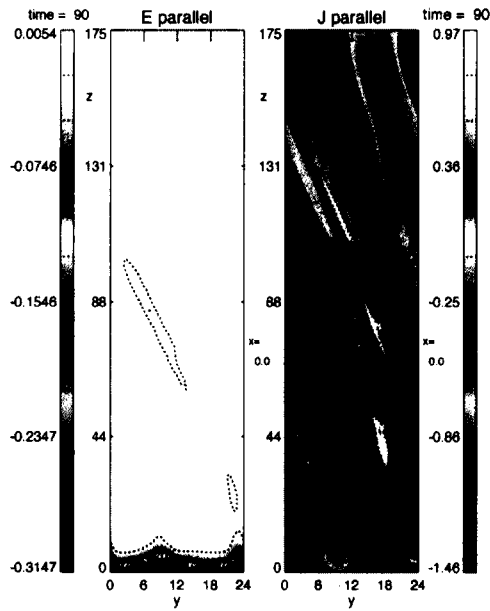


**Figure 3.12 The Integrated Appearance of the Reconnection Region (Reference Run)—Integrated Through the x-Plane. Note That the Initial Reconnection Region Has Spread Into Two Regions.**



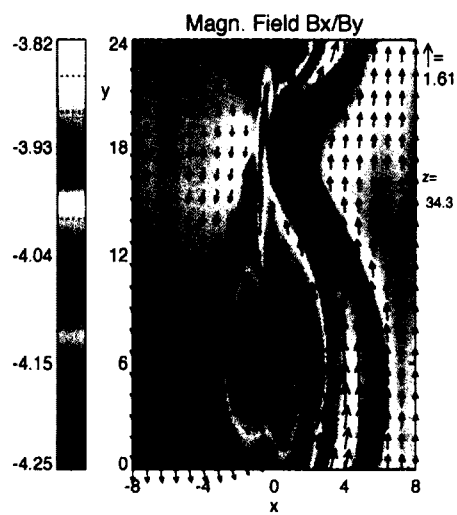


**Figure 3.13 The Magnetic Field in the Vicinity of the Reconnection Region (Sigma 5 Case). Cuts Taken in the z-Plane at 5,980 km.**

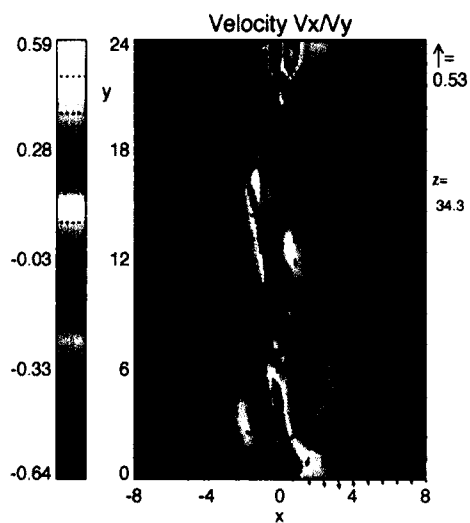


**Figure 3.14 The Velocity in the Vicinity of the Reconnection Region (Sigma 5 Case). Cuts Taken in the z-Plane at 5,980 km.**

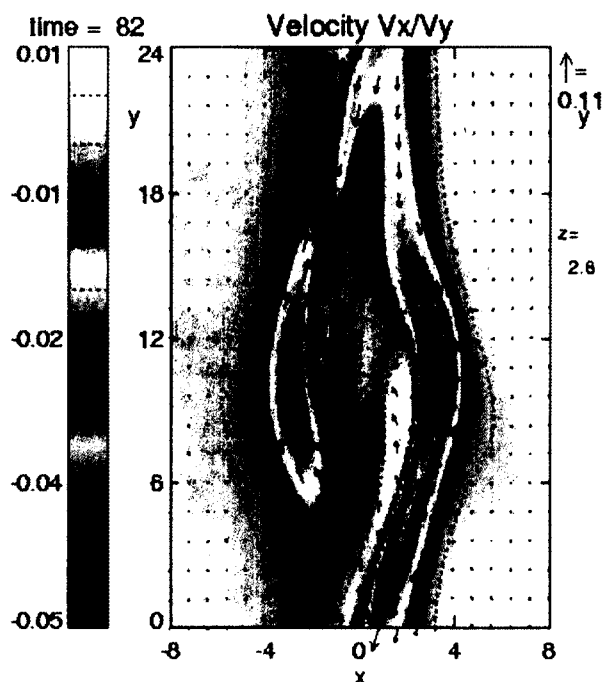


Figure 3.15 Velocity Perturbation for the Reference Run. Cut in the z-Plane at 280 km (Near the Bottom of the Simulation Domain). Note the Anti-Parallel Velocity Shear—on Either Side of the Precipitation Region.

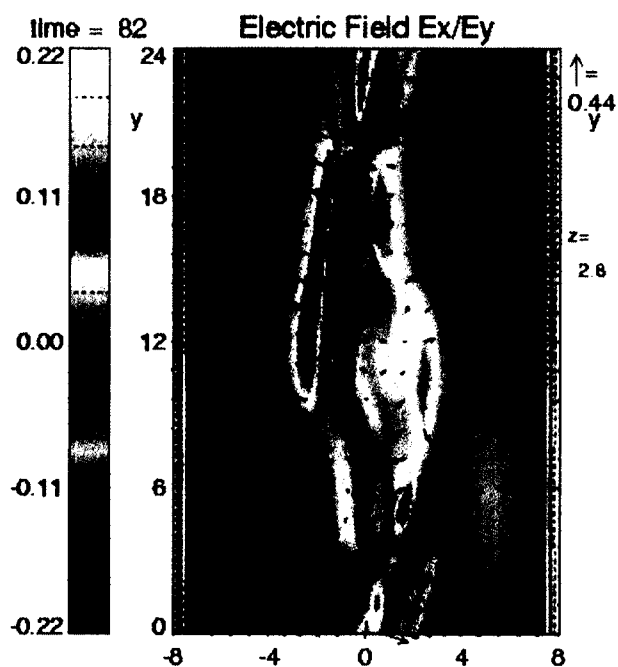


Figure 3.16 Electric Field Perturbations for the Reference Run. Cut in the z-Plane at 280 km (Near the Bottom of the Simulation Domain). Note the Electric Field Components—Pointing Away From the Precipitation Regions.

## Alfvén Wave Diagnostic

### $E_{\parallel}$ region source for Alfvén wave generation

Here the cause for the perturbation of the field-aligned current layer is examined. Since the perturbation has to propagate along the magnetic field, the hypothesis that the reconnection region might be a source of Alfvén wave generation is tested. (The reconnection region is a source of Alfvén waves. This is most evident from the first frames of both Figures 3.9 and 3.23. However, the following discussion maps them, formally, from the reconnection region—to the bottom of the ionosphere, and back.) Consider a region just to the right of the reconnection region (c.f. **Fig 3.2**). As the field lines are reconnected, Alfvén waves travel outwards from the reconnection region, and move further and further down the field line. This (idealized) scenario is portrayed in Fig. 3.17. A snapshot in time of four field lines is shown. The deformation of the field lines is shown to travel downwards, reflect from the bottom of the simulation domain, and start traveling back upwards.

Consider the progress of the Alfvén wave with distance moved from the reconnection region (c.f. **Fig. 3.18**). (The darker colors indicate an Alfvén wave that has reflected from the bottom of the simulation domain, and is heading upwards.) If one were to travel along the second bar across the plot, one would see no signature for line a. One would see Alfvénic signatures for lines b,c,d, and e; however, one

would not see Alfvén signatures for lines f and g, as there is a superposition of the downward and upward traveling Alfvén waves. As there is a change in sign for the velocity (change in direction), the ratio of the superposition of the magnetic and velocity perturbations is no longer + or - 1 (the Walén relation). This forms the basis for the Alfvén wave diagnostic. The location where one is subtracting out the Alfvénic signatures—the location of the “probe”—is signified by an “X.”

If one were to subtract out the velocity and magnetic perturbations of the downward traveling wave for lines f and g, one would again see an Alfvénic signature. This forms a simplified picture of the Alfvén wave diagnostic, used to search (e.g. the edges of the current sheet) for Alfvénic signatures.

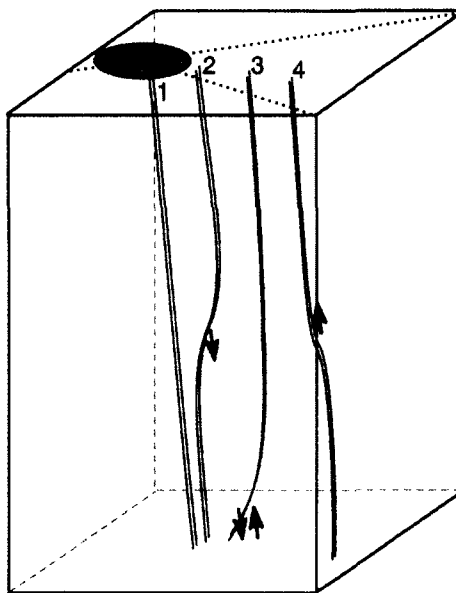
The location of the probe is chosen somewhat arbitrarily. Care must be taken in interpreting results (e.g. potentially there could be extremely slow oscillations of the current sheet that may register as Alfvénic, regardless of its speed).

Fig. 3.19 shows a cut of the Alfvén diagnostic (z-plane) of the reconnection region. This figure shows a snapshot of the velocity field lines and magnitude of the velocity in the z-direction (color code) on the left, and lines of constant Alfvénic speed perturbations and the magnitude of Alfvénic speed perturbations on the right (color code). One can clearly see that the edges of the current sheet have

perturbations that are Alfvénic (by the color code) in character. Note that as one descends to the bottom of the ionosphere, this region gets thinner and thinner—due to the narrowing of the current sheet.

Figs. 3.20 and 3.21 show plots of the Alfvén diagnostic for regions of decreasing altitude. These figures show snapshots of the velocity field lines and magnitude of the velocity in the z-direction (color code) on the left, and lines of constant Alfvénic speed perturbations and the magnitude of Alfvénic speed perturbations on the right (color code). It can be clearly seen, that the perturbations on the edges of the current sheet are Alfvénic, and all the way down to the bottom of the simulation (i.e. bottom of the ionosphere). It is these Alfvénic perturbations, that carry with them both velocity and magnetic perturbations—which are responsible for both the anti-parallel velocity shear, and the electric field, pointing outwards from the (electron) precipitation region(s) (c.f. **Fig 3.15** and **Fig 3.16**). This is shown in Figure 3.22. On the near side of the current sheet, the velocity perturbation is shown (at one point), along with the electric field perturbation (at one point)—similarly on the far side of the current sheet. Because the Alfvénic perturbations have been reflected, the direction of the velocity and electric field perturbations changes. The Alfvénic perturbations—along the entire edge of the current sheet—produce the opposing velocity shear on either side of the (electron) precipitation region, and the electric field projection outwards (from the

precipitation region). Both of these are important features, displayed by discrete [auroral] arcs (Haerendel, Buchert, La Hoz, Raaf, and Rieger 1993).



**Figure 3.17 Progress of the Deformation of the Magnetic Field Lines (Caused by Alfvén Waves) as the Lines Move Further Out From the Reconnection Region**



**Figure 3.18 Alfvén Plot Showing the Progress of the Alfvén Wave—Which Increases With Distance From the Reconnection Region**

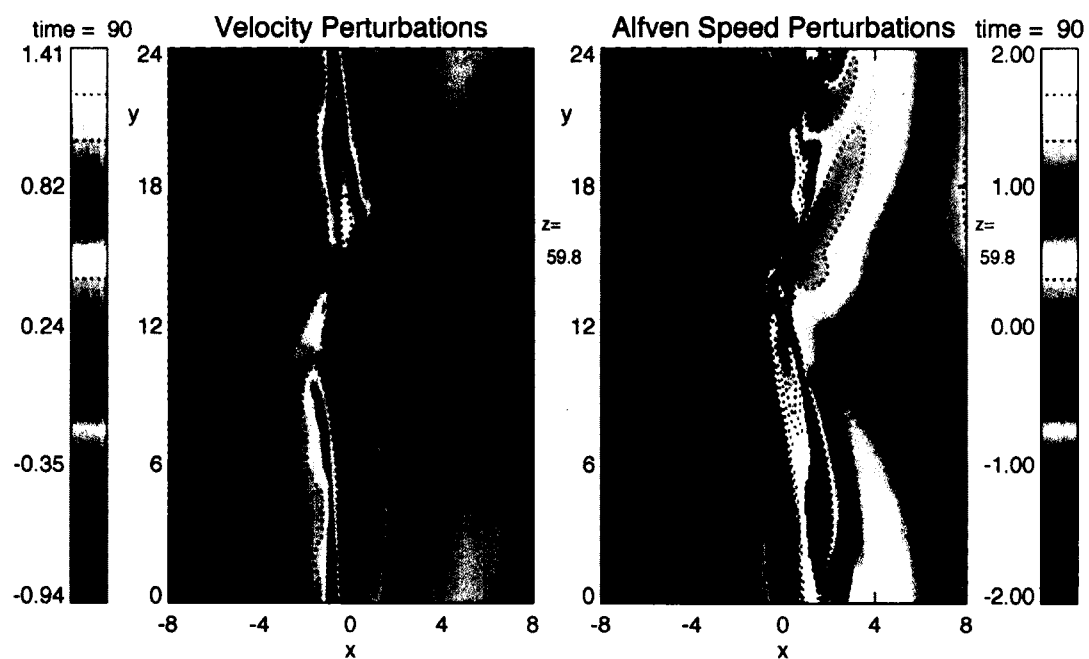


**Figure 3.19 Alfvénic Structures. The Above Are Cuts in the z-Plane (Parallel to the Earth's Surface) at 5,980 km. The y-Direction (Perpendicular to the Current Sheet) Is in km's—As Is the x-Direction (Parallel to the Current Sheet). z is in 100's of km's. This Figure Shows Clear Alfvénic Signatures, on the Boundary of the Current Sheet (Reference Run).**



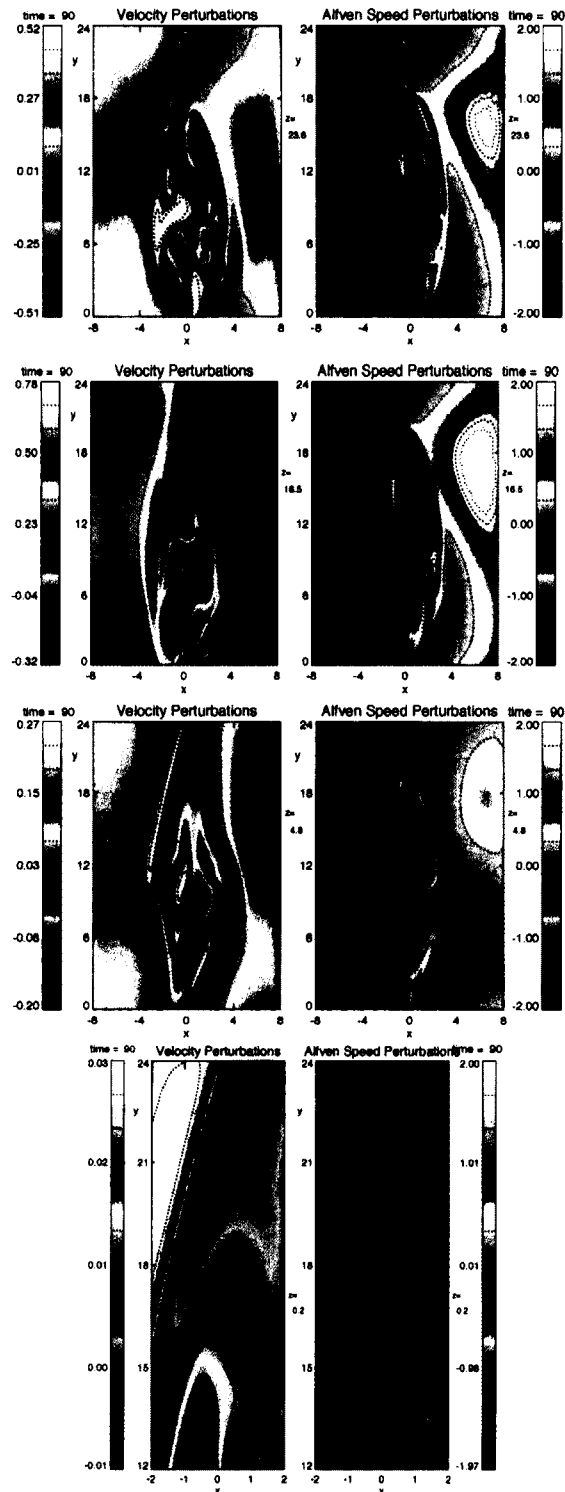


**Figure 3.20** Alfvén Structures for Decreasing Altitude—z-Plane Cuts at 2,360, 1,680, 480, and 200 km, Respectively (Reference Case). Note That the Range of the Last Plot Had to Be "Expanded"—as the Structures Became Quite Thin.

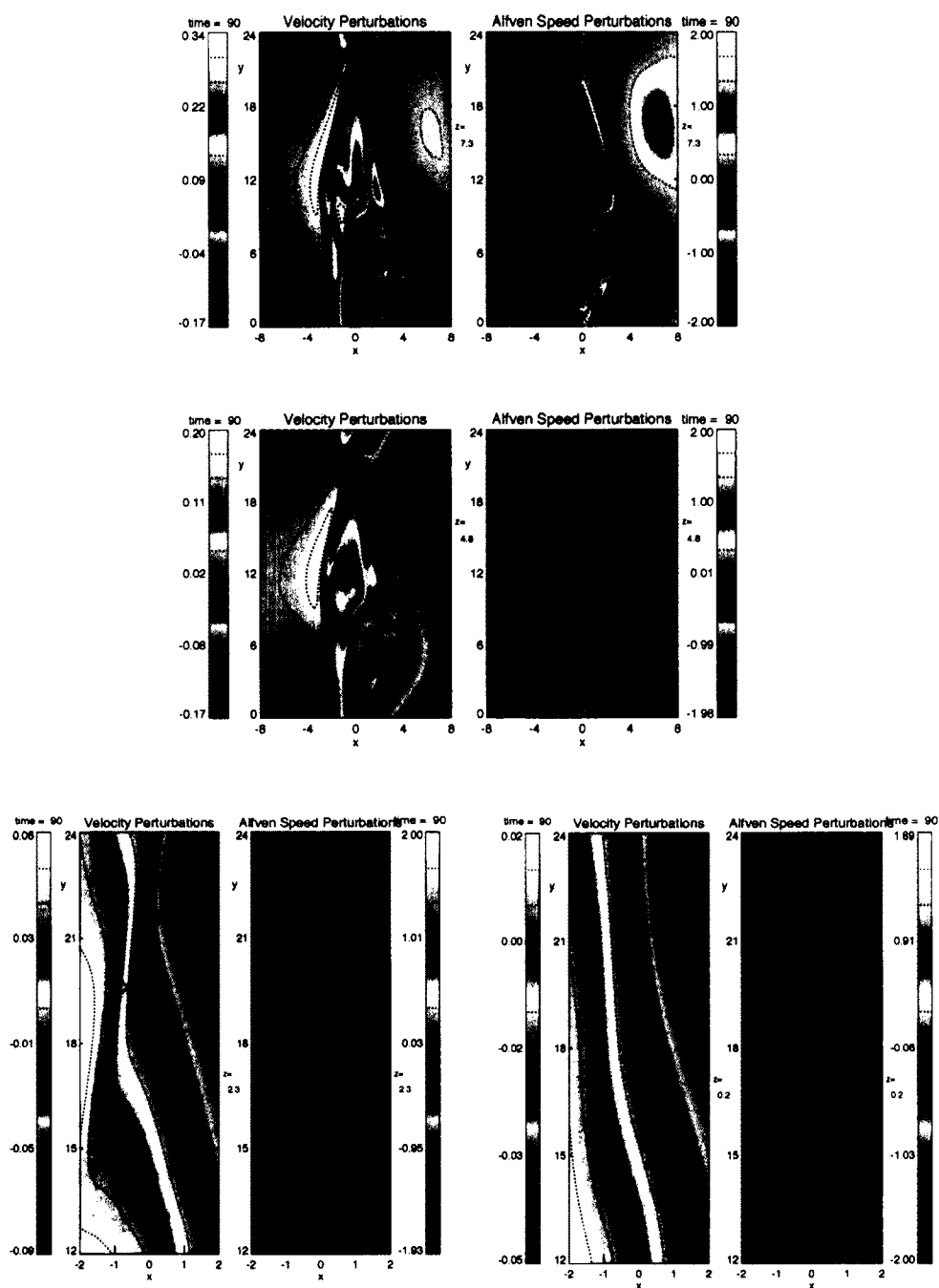


**Figure 3.21 Alfvén Structures for Decreasing Altitude—z-Plane Cuts at 2,360, 1,680, 480, and 200 km, Respectively (Sigma 5 Case, Boundary Conditions B). Note That the Range of the Last Two Plots Had to Be Expanded—as the Structures Became Quite Thin.**

## Discussion of Various Cases

### Influence of Initial Conditions

Below is a discussion of the initial conditions of the runs used in this study. Their effects on the system, particularly the increase in Pedersen conductivity, are discussed. This provides a test of the version of Ohm's law (**Equation 2.18**).

The "sigma=1" run is the reference run. The collisions, symmetry, and shear are all "nominal." That is, the collisions are  $\sim v_{in}$ ; the symmetric is anti-symmetric; and the shear is 0.5 (in system units).

The "old b.c." case employs the old boundary conditions (i.e. Boundary Conditions A). It has an ideally conducting ionosphere; thus the reflection coefficient is not defined. All other parameters are nominal.

The "sigma=1 symmetry" run has all parameters nominal, but the shear velocity was made symmetric. (In the nominal case, the shear was asymmetric.) Aside from a translation of the system, this appeared to have no quantitative or qualitative effect on the system.

In the "sigma=1 velocity" run the velocity of the shear at the top of the simulation was increased. This had the effect of inputting more energy into the system.

In the " $\sigma=1.2$ " run, the collisions towards the bottom of the simulation domain (the ionosphere) are increased by 1.2. This increased the Pedersen conductivity as expected.

In the " $\sigma=1.5$ " run, the collisions towards the bottom of the simulation domain (the ionosphere) are increased by 1.5. This increased the Pedersen conductivity as expected.

In the " $\sigma=2$ " run, the collisions towards the bottom of the simulation domain (the ionosphere) are doubled. This increased the Pedersen conductivity as expected.

In the " $\sigma=5$ " run, the collisions towards the bottom of the simulation domain (the ionosphere) are increased by a factor of 5. This increased the Pedersen conductivity as expected.

In Fig. 3.23 the 3-D structures of the deformation of the current sheet are shown. An equipotential of the current sheet, is shown for 7.5, 15, 22.5, 30, 37.5, and 45 Alfvén times. With this realistic Pedersen conductivity, these current sheets display aurora-like features.

In the " $\sigma=5$  symmetry" run, the collision frequencies were increased by a factor of 5, and the shear was made symmetric. (In the nominal case, the shear was asymmetric.) Aside from a translation of the system, this appeared to have no

quantitative or qualitative effect on the system; the Pedersen conductivity was not appreciably different from the "sigma 5" case.

In the "sigma=5 velocity" run the velocity of the shear at the top of the simulation was increased, and the collision frequency towards the bottom of the simulation domain (the ionosphere) was increased by a factor of 5. This had the effect of inputting more energy into the system, and the Pedersen conductivity was increased as expected.

In the "sigma=7.5" run, the collisions towards the bottom of the simulation domain (the ionosphere) are increased by a factor of 7.5. This increased the Pedersen conductivity as expected.

In the "density" run, the plasma density was increased towards the bottom of the simulation domain (the ionosphere). Although this did increase the Pedersen conductivity, it did not increase it to the extent expected. This points to the possibility that our version of Ohm's Law (**Equation 2.18**) is not completely correct, or, at least, sufficiently inclusive to describe the system.

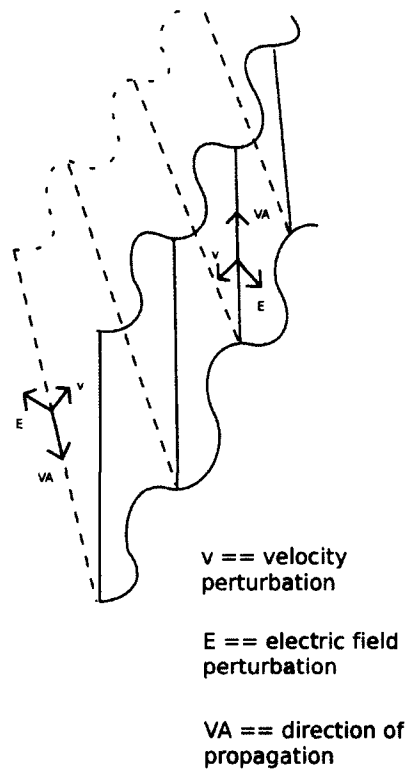
### **Boundaries**

For the Boundary Conditions B case, the magnetic shear at the bottom of the simulation (the ionosphere) was eroded away (dissipation of magnetic energy, into Joule heating), by the plasma being set in motion—spawning an upward-traveling Alfvén wave. If this erosion was a stronger effect than the velocity shear imposed at

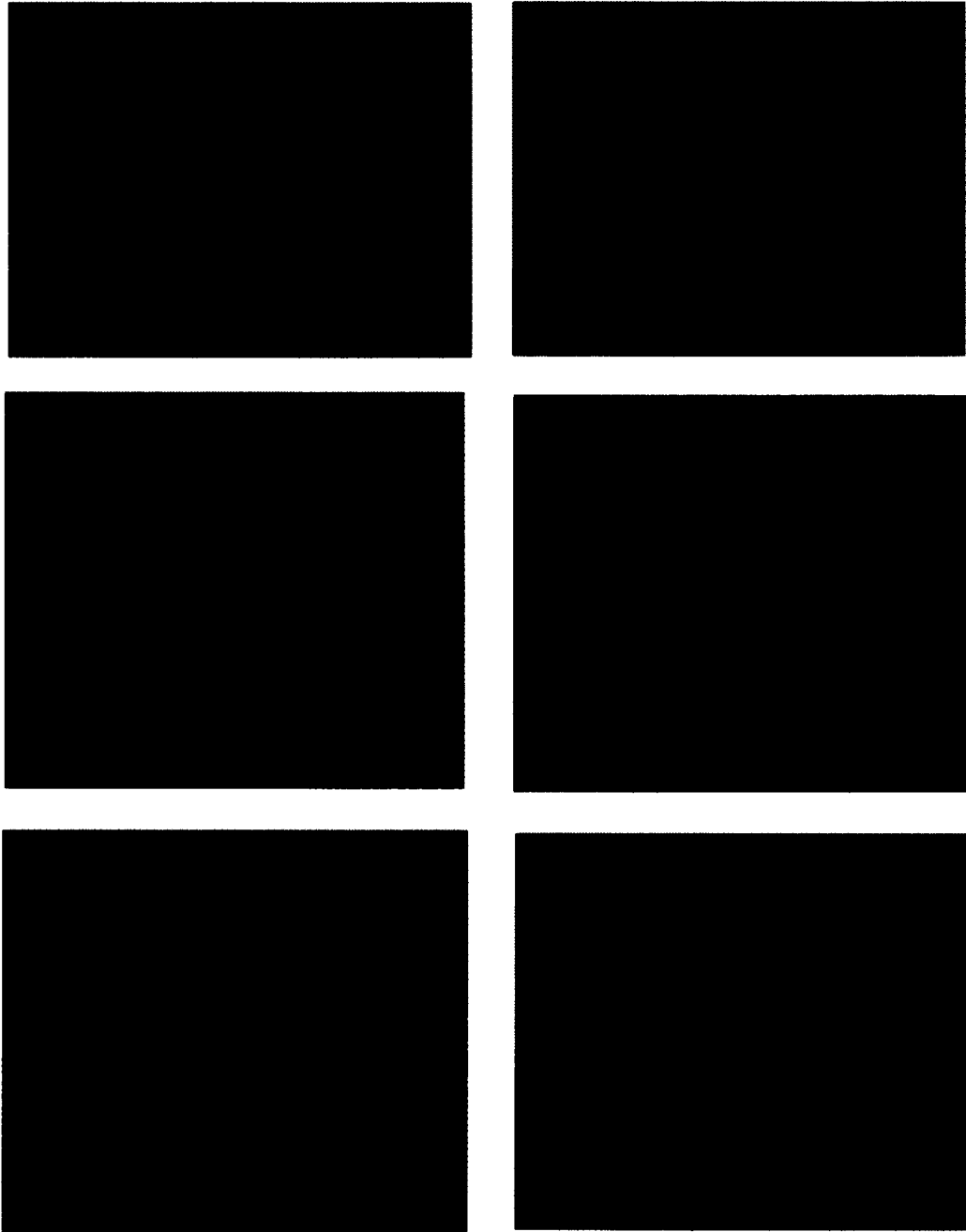
the top of the system, the reconnection region could no longer be maintained, and the characteristics of the discrete aurora were lost.

Fig. 3.24 shows the condition of a sufficient driver (the reference case). This figure shows a snapshot of the magnetic field vectors, and the magnitude of the magnetic field in the z-direction (color code). Fig. 3.25 shows the condition of an insufficient driver [to maintain the reconnection region]. This figure shows a snapshot of the magnetic field vectors, and the magnitude of the magnetic field in the z-direction (color code). The first figure illustrates conditions where enough energy (in the form of Poynting flux) was inputted into the system to maintain reconnection; the second figure illustrates conditions where enough of the magnetic energy was dissipated (in the form of Joule heating) that magnetic reconnection could no longer be maintained, and the characteristics of discrete aurora were lost. Visually, this corresponds to the presence, or lack, of the “kink” ([magnetic] reconnection region) in the [magnetic] field lines.

This is the sigma 10 case, where the collisions were increased by a factor of 10. Please note that the time step had to be altered, to [numerically] resolve the higher collision frequency (lower collision time).



**Figure 3.22 3-D Perturbations. This Figure Shows the Velocity Perturbations, Electric Field Perturbation, and the Direction of Travel of the Alfvénic Perturbations (At Two Points Only—One on the Near Side, and One on the Far Side of the Current Sheet).**



**Figure 3.23 3-D Structures of Deformation of the Current Sheet, for the Boundary Conditions B, the Sigma 5 Case, for 7.5, 15, 22.5, 30, 37.5, and 45 Alfvén Times, Respectively. One Can See in the First Frame, the Disturbance Produced by the Initial Perturbation, and the Alfvén Waves Flowing Away From It. The Remaining Frames Show the Reflection of the Alfvén Wave From the Bottom of the Simulation Domain. With a Realistic Pedersen Conductivity, These Current Sheets Display Aurora-Like Features.**



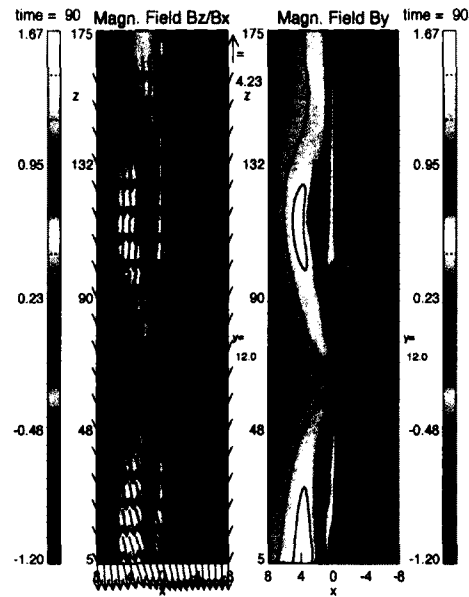


**Figure 3.24 Sufficient Driver to Maintain Shear—Reference Case. Cut in the y-Plane (Perpendicular to the Current Sheet)—at  $y=12$  km (Mid-Point)**

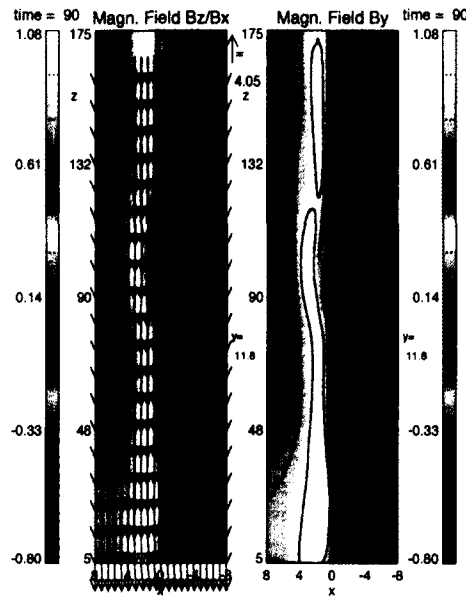


**Figure 3.25 Insufficient Driver (Erosion of Magnetic Shear)—Sigma 10 Case, Boundary Conditions B. Cut in the y-Plane (Perpendicular to the Current Sheet)—at  $y=12$  km (Mid-Point)**

## Conductance

In Fig. 3.26, a progression of descending plots of velocity perturbations, in the z-plane, is shown. The plots are snapshots of velocity field vectors and magnitude of velocity in the z-direction (color code) on the left, and velocity field lines and magnitude of the velocity in the z-direction (color code) on the right. These are for the reference case. The plots display a remarkable amount of fine-scale structure—in the form of rapid changes of velocity (both magnitude and direction) over small spatial scales.

However, in Fig. 3.27, the sigma 10 case (Boundary Conditions B), less fine-scale structure is shown, as more of the Alfvén wave is reflected, due to the higher conductance. This is a remarkable result. The plots are snapshots of velocity field vectors and magnitude of velocity in the z-direction (color code) on the left, and velocity field lines and magnitude of the velocity in the z-direction (color code) on the right.

Upon examination of the various cases, it appears that a higher conductance is more conducive to a switching off of the magnetic reconnection, and the loss of discrete aurora-like features. However, it is not obvious why this should be the case.

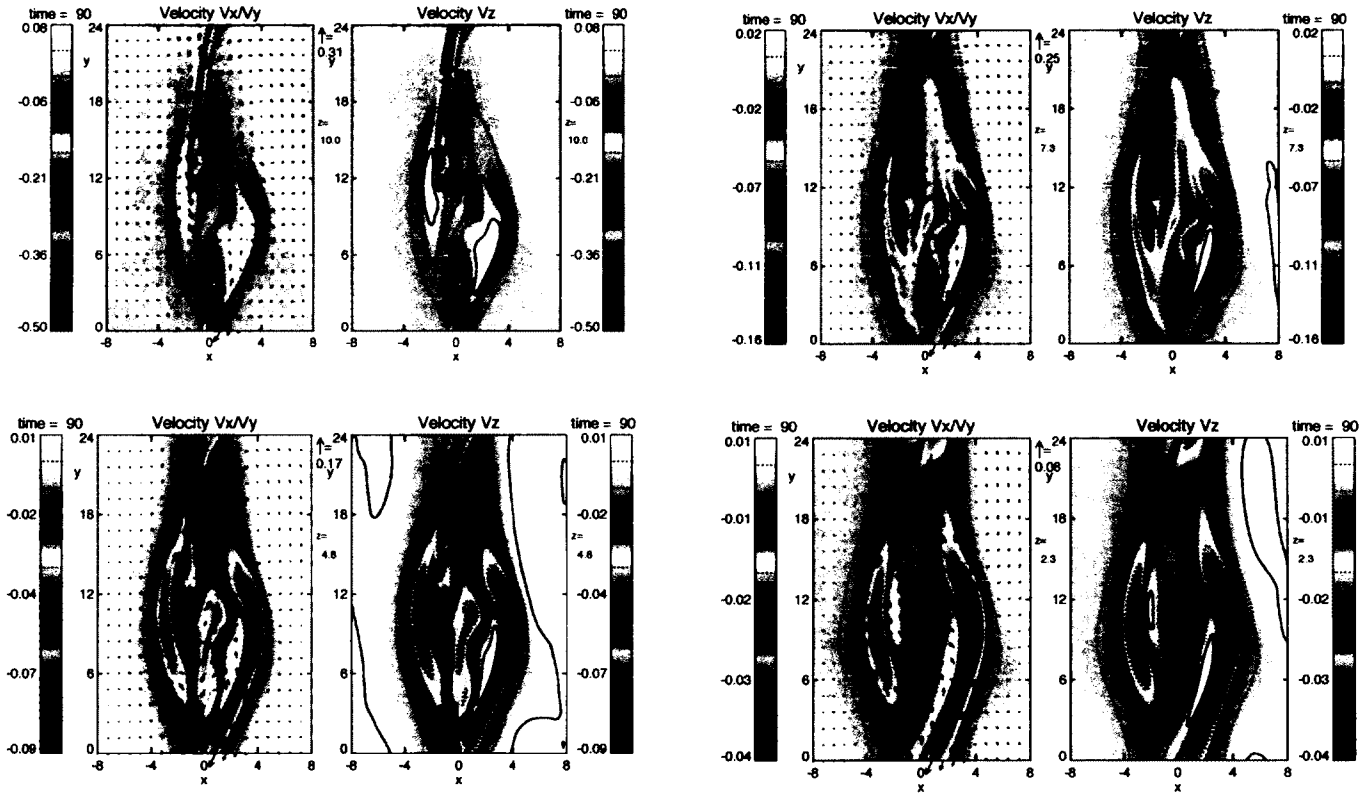


**Figure 3.26 Velocity Perturbations—Cuts in the z-Plane, at 1,000, 730, 480, and 230 km (Reference Run). These Plots Show Remarkable Fine-Scale Structure**

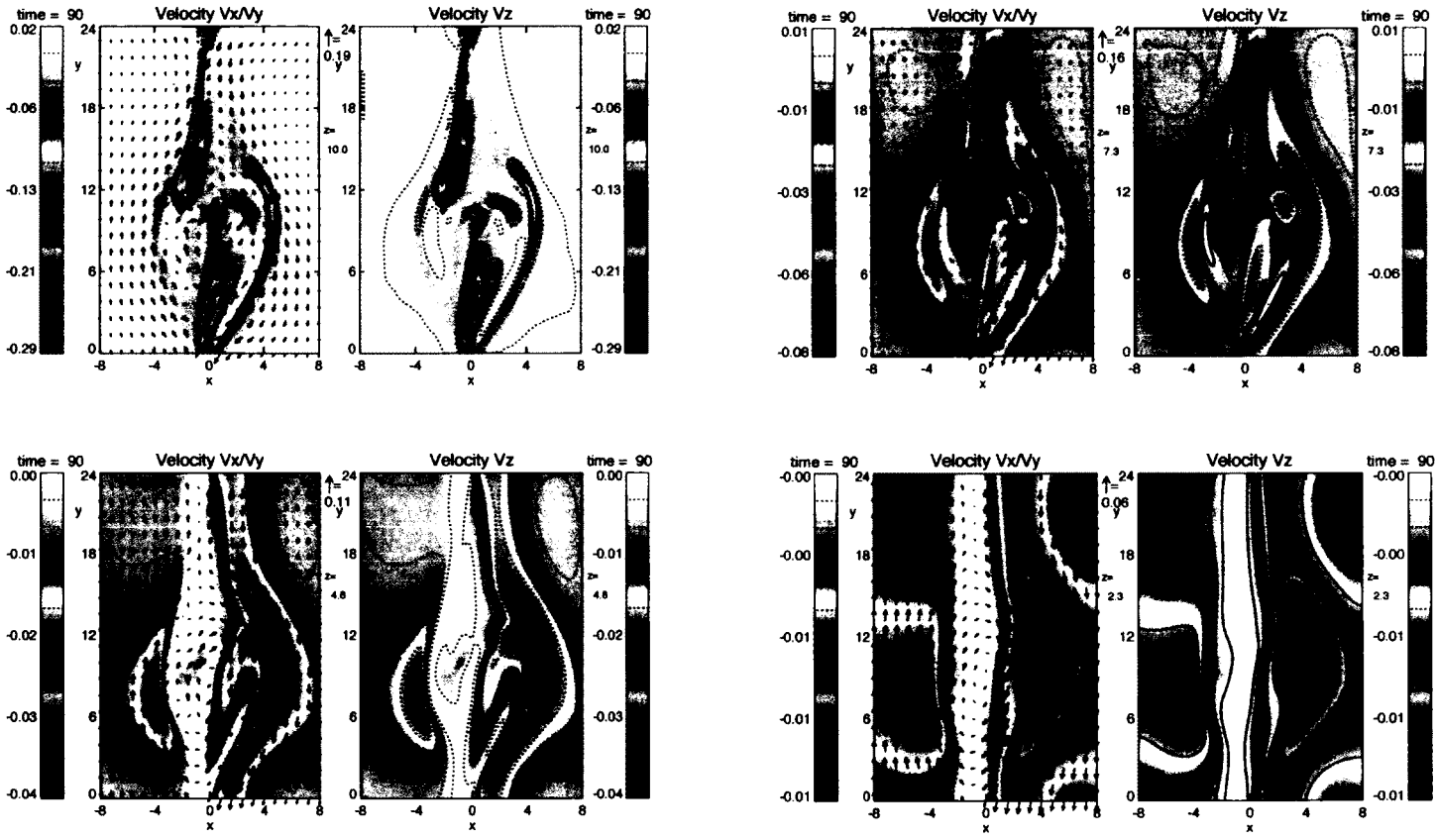


**Figure 3.27 Velocity Perturbations—Cuts in the z-Plane, at 1,000, 730, 480, and 230 km (Sigma 10 Case, Boundary Conditions B). Note That These Plots Show Less Fine-Scale Structure—Due to More of the Alfvén Waves Being Reflected Higher in the Simulation Domain.**

## Realistic Ionospheric Conductivities

Recall that:

$$\Sigma_p = \frac{1}{\mu_0 B_0} \frac{\Delta B}{\Delta v}$$

Therefore,

$$\Sigma_p \text{ (physical units)} = \left(4\pi \times 10^{-7} \frac{H}{m}\right) (0.5G) \Sigma_p \text{ (system units)}$$

(See the normalization, **Chapter 2**.)

$\Sigma_p$  ranges from  $\sim 0.95$  to  $5.96$  (c.f. **Table 3.2**). Therefore, the height-integrated Pedersen conductivity ranges from approximately  $4.18 \times 10^{-6}$  to  $2.62 \times 10^{-5}$  Siemens.

In Fig. 3.28, a plot of realistic ionospheric conductivities (nighttime) is shown. It shows height in kilometers, vs. conductivities in Siemens. As this is a log plot—the maximum, in a “rough cut,” is approximately equivalent to the (height) integrated property. Therefore, the model has been shown to reproduce realistic height-integrated Pedersen conductivities.

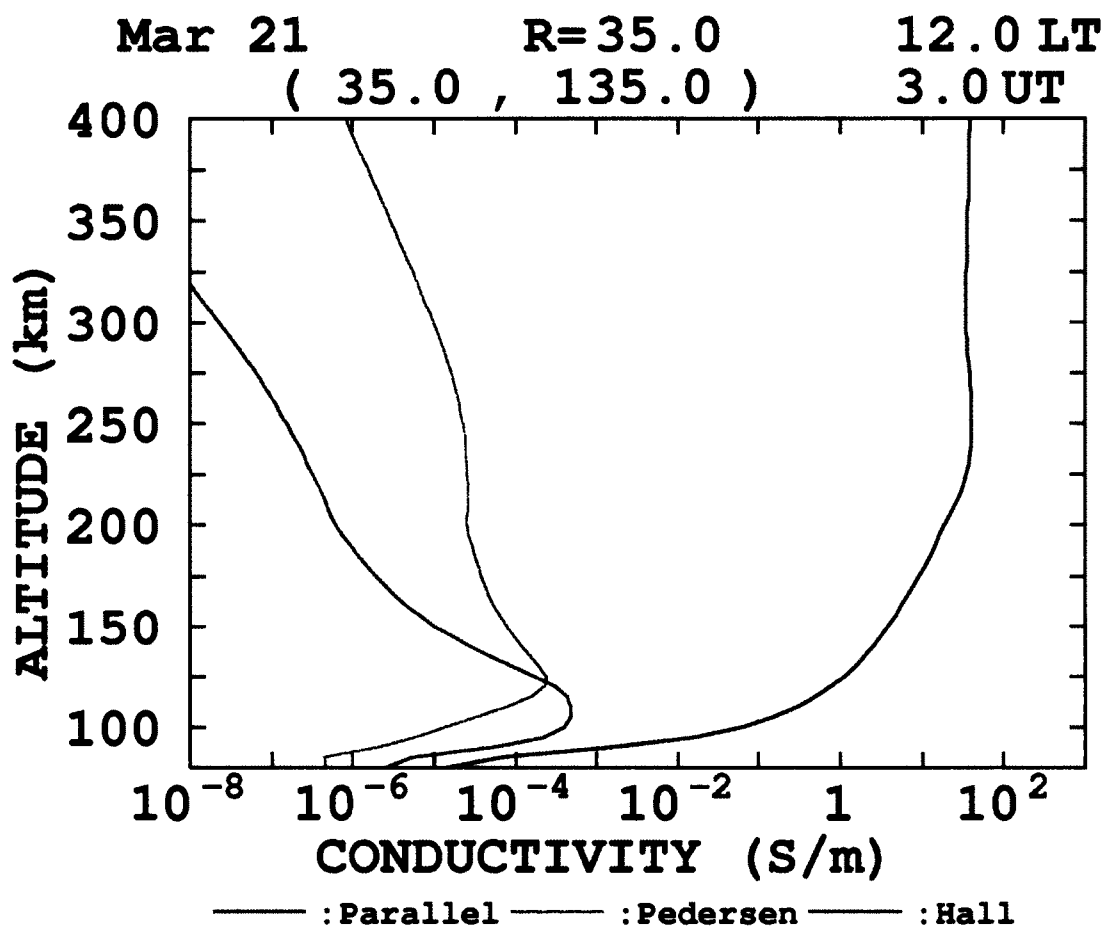


Figure 3.28 Realistic Ionospheric Conductivities (From <http://wdc.kugi.kyoto-u.ac.jp/ionocond/exp/icexp.html> "On the Ionospheric Conductivity," Kitashirakawa and Sakyō, July, 2011).

## Discussion

The reflection of an Alfvén wave from the ionosphere was successfully modeled. This was performed for both Boundary Conditions A and Boundary Conditions B.

It has been shown that the initial resistivity perturbation is a source of Alfvén wave generation. This is most clearly evident in the first frames of both Figure 3.9 and Figure 3.23. Alfvén waves have been shown to “map” from the reconnection region, to the bottom of the ionosphere, and back. It is these Alfvén waves, traveling downward from the reconnection region, that carry with them a magnetic perturbation, resulting in a current, and a parallel electric field, in the presence of a localized resistivity. It has been shown that Alfvén waves, spawned by this reconnection region, are responsible for the deformation of the current sheet.

The edges of this current sheet have been shown to have waves of Alfvénic character. These Alfvénic structures, that carry with them both velocity and magnetic perturbations are responsible for both the anti-parallel velocity shear, and the electric field, pointing outwards from the (electron) precipitation region(s) (c.f. **Fig 3.15** and **Fig 3.16**). In addition, upon visual inspection, the appearance of the (electron) precipitation region is very similar to that of actual discrete aurora. At their reflection at the bottom of the simulation domain (the ionosphere), these regions become quite thin (due to the narrowing of the current sheet)—again, a very (discrete arc) aurora-like feature.

The parameters of the system were varied, to produce differing conductivities. The behavior of these conductivities was as expected—except for the behavior of the “Density” run. The failure of an increase in plasma density to increase the Pedersen conductivity as expected, points to the possibility that the assumptions of the model are not entirely correct, or, at least, not entirely complete.

It was shown that it was more likely that an increased conductance was more likely to shut off the magnetic reconnection—with a resultant loss of discrete aurora-like characteristics. However, the mechanism for this is uncertain.

Realistic ionospheric conductivities were reproduced. They ranged from approximately  $4.18 \times 10^{-6}$  to  $2.62 \times 10^{-5}$  Siemens (c.f. **Fig. 3.28**).

There are many outstanding issues involved with the formation and time evolution of discrete auroral arcs, including: the narrowness of arcs current sheet structures above arcs; electric fields extending parallel outwards from the arcs; fast (plasma) flows in the region of discrete arcs; and the formation and maintenance of parallel (to the magnetic “guide field”) electric fields—deep into the ionosphere.

The model has reproduced, qualitatively and semi-quantitatively, the features of discrete auroral arcs, and their time evolution. The lower regions of the simulation domain reproduced the attributes of discrete auroral arcs: a thin [mostly electron] precipitation region, electric fields extending out perpendicularly to said



region—and velocity shear parallel to it. This has been achieved in a fully self-consistent manner.

Major theoretical underpinnings of this work have been previously postulated (notably Otto and Birk 1993 and Zhu, Otto, Lummerzheim, Rees and Lanchester 2001). However, performing the simulations in three dimensions, as well as determining which input parameters (e.g. shear rate—that is, a measure of energy inputted into the system; conductance, Pedersen conductivity) lead to a “switching on” or a “switching off” of those properties which lead to aurora arc formation ([magnetic] reconnection), and the mapping of the Alfvénic perturbation from the magnetic reconnection regions is entirely new.

## **Chapter 4 Joule Heating**

### **Introduction and Motivation**

A major portion of the solar wind energy that crosses the magnetopause, ends up being deposited in the ionosphere, in the form of Joule heating. This heating is mainly caused by the dissipation of the Pedersen currents, and the majority is deposited in the auroral zone (Kosch and Nielsen 1995). As the consequences of this Joule heating are appreciable, and global in the M-I coupled system, accurate knowledge of the amount of heating occurring is essential.

Large-scale experimental observations and global models have limited spatial and temporal resolution, and yield parameters that are averaged in space and time. These large-scale experimental observations can fail to resolve accurate values for many important physical processes. Specifically, such large-scale or global approaches may result in an underestimation of the Joule heating (Rodger, Wells, Moffett, and Bailey 2001). A computer model designed to look at small-scale temporal and spatial scales was employed to make quantitative measurement of the Joule heating occurring over various scale averages.

Because of the (unavoidable) underestimation of the Joule heating in global models, they fail to match up with observations. Even with present-day computational resources, the largest supercomputers do not have sufficient memory or processing power to resolve small scales over a global simulation

domain. Attempting to remove this mismatch was an important motivation for this study.

Knowledge of the geo-space environment is obtained from large-scale and global observations, and from global models of the geo-space environment. It is known that many important physical processes in the geo-space environment happen on smaller spatial and temporal scales than can be resolved by large-scale observations. This is particularly true of the discrete aurora, which shows structure with a typical length scale ranging from 100 m to over 1,000 km (Trondsen and Cogger 1998; Trondsen and Cogger 2001), and motions with time scales of a fraction of a second. The time-varying nature of the electric field can lead to an underestimation of the Joule heating.

For example, for ISR (incoherent scatter radar), the range resolution (dependent upon the distance from radar) is on the order of 100's of meters (e.g. 300 m). In this example, for a beam width of  $\sim 1/2$  degree at 100 km, the fundamental of the horizontal resolution is 873 meters.

Another uncertainty is given by the signal to noise ratio. One needs a sufficient number of electrons in order to obtain resolution. For a strong signal (high electron density), and the above conditions, this would be on the order of 1 minute (Bristow, pers. comm.). This is an example of a temporal average.

Because of the nonlinear nature of many processes in M-I coupling, observed and modeled averaged quantities do not always yield consistent results. An example of such a mismatch is the heating and temperature balance in the high latitude thermosphere-ionosphere system. A significant heat source in the aurora results from the ion-neutral collisions in strong ionospheric currents. The large-scale structure of these currents provides extended regions of Joule heating in and around the auroral oval. Models of this large-scale heating source, however, do not account for the observed temperature increase in the auroral zone (Emery, Lathuiller, Richards, Roble, Buonsanto, Knipp, Wilkenson, Sipler, and Niciejewski 1999). Structured auroras cause strong gradients in the plasma density and consequently in conductivity. At the same time, the ionospheric electric fields in aurora also show structure on the same spatial and temporal scale as the visible aurora (Lanchester, Rees, Lummerzheim, Otto, Sedgemore-Shulthess, Zhu, and McCrea 2001). Thus, there are strong and highly localized currents which lead to a similarly localized and uneven distribution of heating. Large-scale modeling of the thermosphere using only averaged electric fields, conductivities, and currents misses these heating sources. The mismatch between modeled temperatures and observations can be large, requiring an increase of the Joule heating source by a factor of 2 (Emery, Lathuiller, Richards, Roble, Buonsanto, Knipp, Wilkenson, Sipler, and Niciejewski 1999).

The following is a derivation of a means of quantitatively measuring the loss of Joule heating by larger-scale averaging. It is used extensively in the model. Please note that this is a two-dimensional derivation—the Joule heating is calculated in plane parallel to the Earth’s surface, near the bottom of the ionosphere.

The average Joule heating is given by:

$$\langle Q \rangle = \frac{1}{\int_{FOV} d^2r} \int_{FOV} Q d^2r \quad (\text{Equation 4.1})$$

where  $Q \equiv$  the Joule heating, and  $FOV \equiv$  the field of view. (By field of view, it is meant the range over which an experimental observation or measurement of a model is made.)

where:

$$A = \int_{FOV} d^2r \quad (\text{Equation 4.2})$$

(Note that  $d^2r = dx dy$ . Also please note that  $Q$  can also be integrated over time—in which case, one divides by the time integral to obtain the time-averaged Joule heating.)

The unaveraged Joule heating is given by:

$$\begin{aligned} Q &= \vec{E} \cdot \vec{j} \\ &= \vec{E} \cdot \underline{\underline{\sigma}} \cdot \vec{E} \\ &= \sigma_p \vec{E}^2 \end{aligned} \quad (\text{Equation 4.3})$$

Note that the volume integrated Pederson conductivity is expressed as  $\Sigma_p$ .

The spatially-averaged Joule heating is thus given by:

$$\begin{aligned}\langle Q \rangle &= \langle \sigma_p E^2 \rangle \\ &\approx \langle \sigma_p \rangle \langle E \rangle^2 \quad (\text{Equation 4.4})\end{aligned}$$

Since the velocity is never uniformly in one direction, averaging over larger scale sizes will always result in an under-estimation of the Joule heating.

As an aside, worth mentioning is that the complete (unaveraged) Joule heating is given by:

$$q = \sigma_p (\vec{E} \times \vec{u}_n \times \vec{B})^2 \quad (\text{Equation 4.5})$$

where  $\vec{u}_n$  = the neutral wind.

Qualitatively, one can view this process this way. As the neutral wind in the model is zero, and  $\vec{E} = \vec{v} \times \vec{B}$ :

$$q = \sigma_p (\vec{v} \times \vec{B})^2$$

$$q \propto \sigma_p B^2 (v^2)$$

$$q = (\text{constants})v^2 \quad (\text{Equations 4.6})$$

Thus, the Joule heating is proportional to the velocity squared. If the velocity changes rapidly either spatially, or over time, taking either a larger spatial average, or a larger temporal average, will result in a loss of Joule heating. Similarly, in a region of either high temporal or spatial fine structure, an increase in resolution (correspondingly temporal or spatial) will result in a much higher value for the Joule heating.

The method of computation of the Joule heating is shown (qualitatively) in Figure 1. The boundaries for the scale averaging and the boundaries for the processors are shown. As this computation is fully automated for arbitrary grids, and an arbitrary (1-D) parallelization scheme, this represents a significant level of code design and implementation.

In the model, the neutral dynamics are turned off. This roughly halved the number of computations—the physical rationale for this is that for the length of time the simulation runs, the time scales of the neutral dynamics are too long to be appreciable.

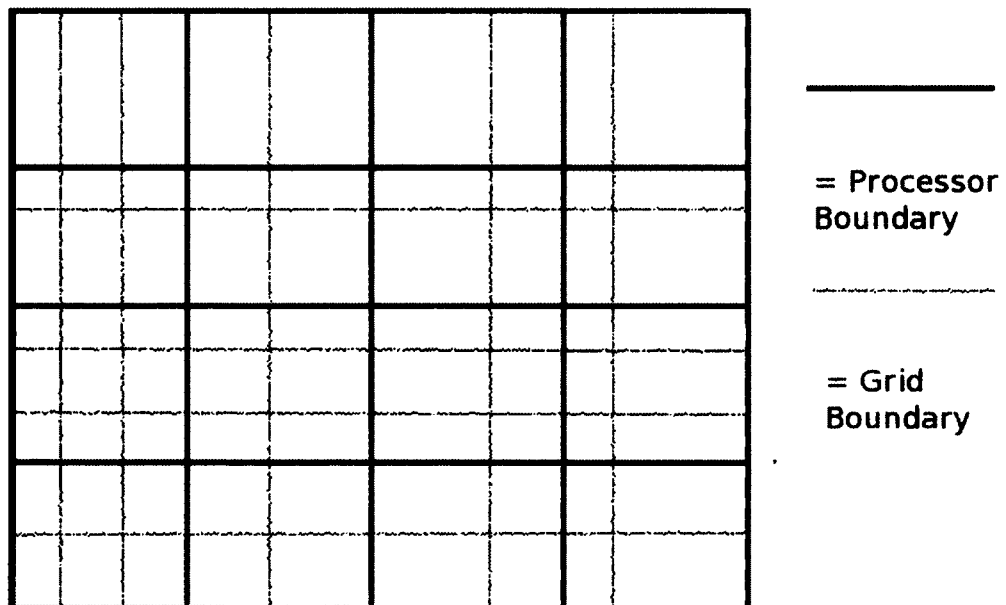


**Figure 4.1 Joule Heating Diagram. This Figure Shows an Idealized Picture of How the Joule Heating is Computed Over Various Processor and Grid Boundaries.**

So, while the above derivation is valid within the model, it should be noted that ignoring the neutral wind may result in an overestimation of the Joule heating by as much as 40%, or an underestimation by as much as 400% (Thayer 1998).

Please note that one cannot measure  $\langle E_{\perp}^2 \rangle$  directly, but can only make measurements of  $\langle E_{\perp} \rangle$ .

Attempts at remedying the problem of the underestimation of the Joule heating in models include: artificially increasing the heating in aurora by a constant factor (Emery, Lathuiller, Richards, Roble, Buonsanto, Knipp, Wilkenson, Sipler, and Niciejewski 1999), using nested grids to locally increase the spatial and temporal resolution (Fuller-Rowell 1985), or accounting for not only the average but also the temporal variability of the electric field in the calculation of heating sources (Codrescu, Fuller-Rowell, Foster, Holt, and Cariglia 2000).

The model employed in this study used high temporal and spatial resolution measurements of small-scale physical processes using an ionosphere-magnetosphere auroral model. A computational study was made of the Joule heating, and the effects of averaging over various length scales was observed. High spatial and temporal resolution was employed to address heating on scales upward of 100 m and time scales of  $10^{-2}$  sec. Eventually it is proposed to determine which observable parameters can be employed as a parameterization and derive



methods and parameterizations that correct the consequences of missing small-scale structure in the global models.

The developed model is suitable to study small-scale auroral processes. It includes energetic particle transport, and the dynamics and energetics of the neutral gas and plasma. The model is 3-D, and has 3-fluids (ions, electrons, neutrals). The interaction of a highly collisionless plasma with a strongly collision dominated plasma required an extension of the usual fluid plasma equations, to include the transport which dominates ionospheric dynamics. Ionospheric transport is included as a set of source terms in the set of fluid plasma equations.

### **Boundary Conditions**

Two distinct boundary conditions were used in this study. The first case—Boundary Conditions A—computed  $\mathbf{B}$  (the magnetic field) at the lower simulation boundary, with the assumption that the magnetic field is symmetric. The densities, pressures and temperatures were computed by continuous boundary conditions.

In the second case—Boundary Conditions B—magnetic perturbations in  $x$  and  $y$  were set to zero ( $B_x = B_y = 0$ ), and  $B_z$  was computed from  $\nabla \cdot \vec{B} = 0$ . This was the most expedient way of closing the currents through the Pedersen currents; in the Boundary Conditions A case, the currents were able to flow through the bottom of the simulation domain. Setting the above magnetic perturbations to zero

greatly increased the Pedersen conductivities in the simulation—allowing ionospheric currents to close in a more realistic manner. This comprised the Boundary Conditions B case.

## Results

**Table 4.1 Inventory of Runs**

Boundary Conditions A	Applied Shear Rate (System Units)
	0.25
	0.50
	0.75
Boundary Conditions B	
	0.25
	0.50
	0.75
	1.00

### Boundary Conditions A

The amplitude of the shear flow applied at the top of the simulation domain (c.f. **Chapter 3, Figure 3.2**) was varied—to see the effect on the Joule heating. This magnitude (imposed at the top of the simulation domain, a measure of the energy input into the system) was used as an input—the shear flow was set in system units at 0.25, 0.50 (nominal), 0.75, and 1.0.

The total Joule heating was computed for grid resolutions of numerical resolution, 1 square km, 4 square km's, 16 square km's, 64 square km's, and 256 square km's. (The numerical grid resolution was on the order of 0.1 km in x, 0.4 km in y.) It should also be noted that the Joule heating was computed in a plane,

corresponding to approximately 120 km's from the Earth's surface. The choice of numerical resolution had a marked effect on the total observed Joule heating—indicating a remarkable amount of fine scale structure (in the form of variation of velocity perturbations over small spatial scales) being present.

As a reference run, a study was made of the Joule heating for various scale sizes, without an initial perturbation (c.f. **Chapter 3**) and an imposed shear rate of 0.50. Interestingly, this example shows a higher peak of Joule heating, when the Alfvén wave spawned at the top of the simulation domain (c.f. **Chapter 3**) reaches the bottom of the simulation domain, than for the case with an initial perturbation (**Figure 4.2—Absence of Resistivity Region**).

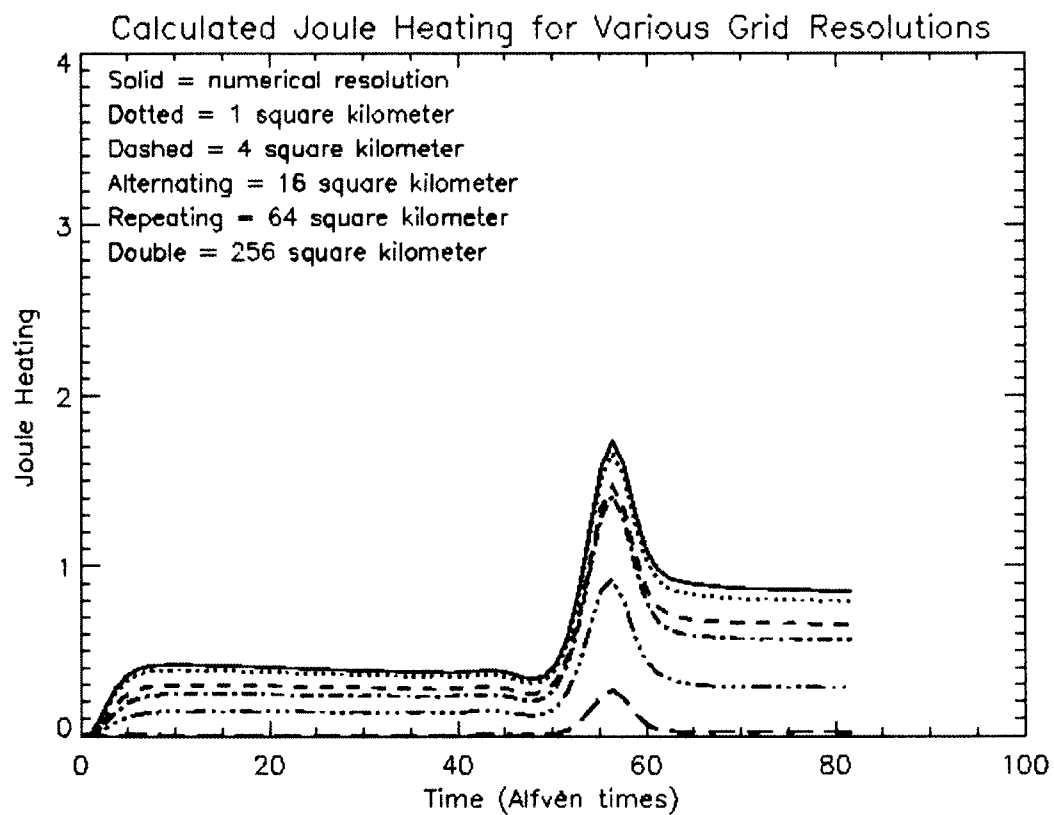
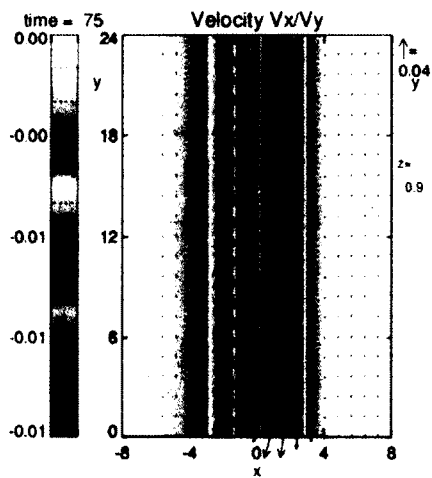
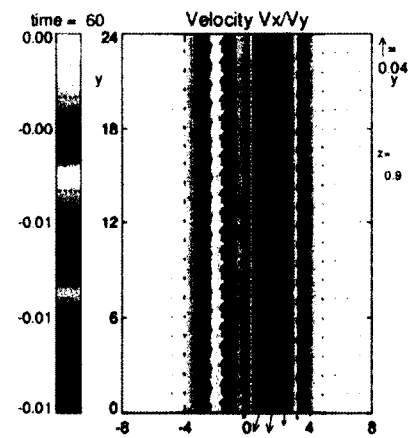
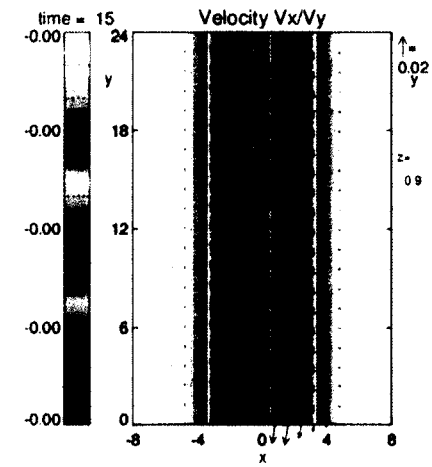


Figure 4.2 Joule Heating—Absence of Resistivity Region



**Figure 4.3a, 4.2b, and 4.2c**  
Velocity Perturbations in the  
x-y Plane (Near the Bottom of  
the Simulation Domain) for  
Before the Peak,  
(Approximately) During the  
Peak, and After the Peak.

The first figure (**Figure 4.2, Joule heating no initial perturbation**) shows the initial plasma motion (This is caused by dissipation in the field-aligned current—the plasma is responding with  $\vec{E} = \vec{v} \times \vec{B}$  motion, the only way that the plasma can respond—to the non-equilibrium configuration of the current sheet, an imposed initial condition.), followed by a peak (indicating the arrival of the Alfvén wave), and finally a region of increased flow—due to the energy imparted by the reflecting Alfvén wave. The second set of figures (**Figs. 4.3a, 4.3b, and 4.3c**) show a very smooth velocity distribution—on both sides of the current sheet. These figures show snapshots of the velocity field vectors and the magnitude of the velocity in the z-direction (color code). The absence of an initial perturbation has resulted in an undisturbed evolution of the simulation—there has been a very tidy reflection of the Alfvén wave, spawned at the top of the simulation domain, with no turbulence or spreading/deformation of the current sheet.

A study was then made of altering the shear rate at the top of the simulation domain. Shear rates (in system units) of 0.25, 0.50, and 0.75 were used. The shear rate of 1.0 (for the Boundary Conditions A case) proved too unstable for sufficient time-evolution of the simulation.

In Figs. 4.4, 4.5, and 4.6 (figure references: Joule heating shear rate of 0.25, Joule heating shear rate of 0.5, and Joule heating shear rate of 0.75, respectively), it can be seen that the total amount of heating maps linearly with the imposed shear

rate. This is a reasonable result; the rate of shear establishes the amount of energy that is input into the system (in the form of Poynting flux). Figures 4.4, 4.5, and 4.6 show the velocity field vectors and the magnitude of the velocity in the z-direction on the left.

In addition, as the shear rate increases, the velocity distribution becomes increasingly turbulent. This can be seen in Figs. 4.4, 4.5, and 4.6 (velocity distributions for a shear rate of 0.25, velocity distribution for a shear rate of 0.5, and velocity distribution for a shear rate of 0.75, respectively).

The cause for this turbulence, and the—rather remarkable—amount of fine structure, is the deformation—striation—of the field-aligned current sheet (See Chapter 3, particularly Fig. 3.23.). From an inspection of right-hand Figs. 4.4, 4.5, and 4.6, it would appear that one would need to go (at least) to a scale size at the numerical resolution ( $\sim 0.1$  km in  $x$ ,  $\sim 0.4$  km in  $y$ ), to resolve the spatial variation in the Joule heating, and to at least an Alfvén time ( $\sim 1.1$  seconds) to resolve the temporal variations [of the Joule heating]. (Prior to the turbulence after the arrival of the peak in Joule heating, a scale size of 1 square kilometer would appear to be adequate.) This corresponds to a truly remarkable degree of fine structure both spatially, and temporally, in the velocity perturbations.

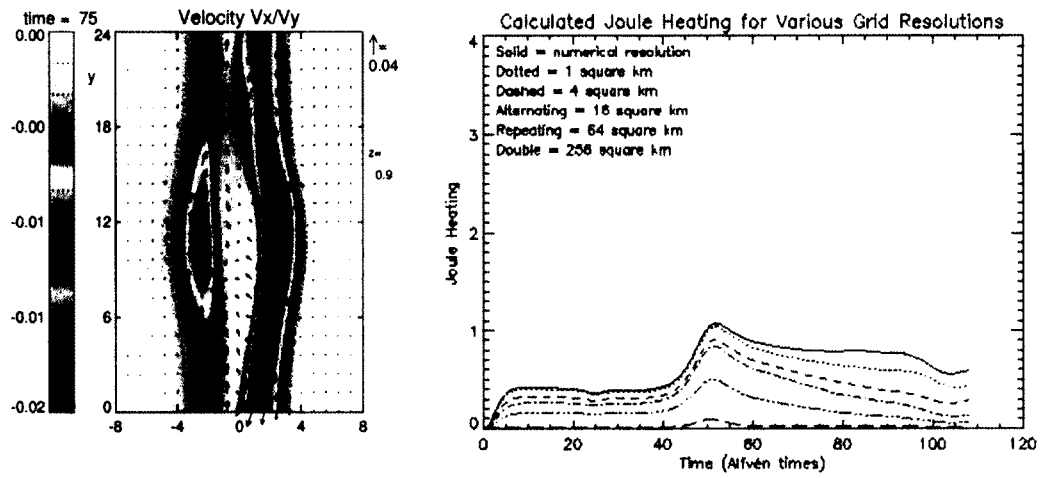


**Figure 4.4 Velocity Perturbations and Joule Heating for a Shear Rate of 0.25 (Boundary Conditions A)**

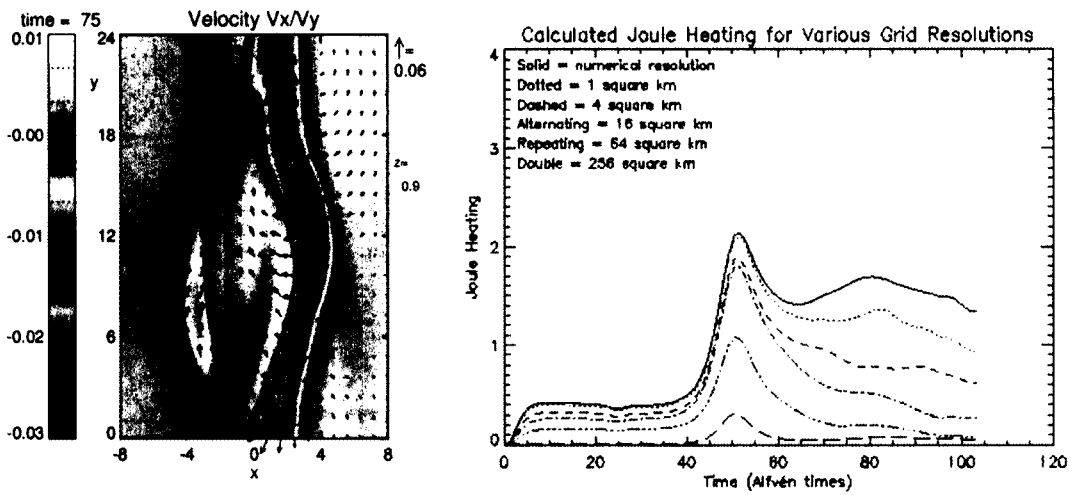


**Figure 4.5 Velocity Perturbations and Joule Heating for a Shear Rate of 0.50 (Boundary Conditions A)**



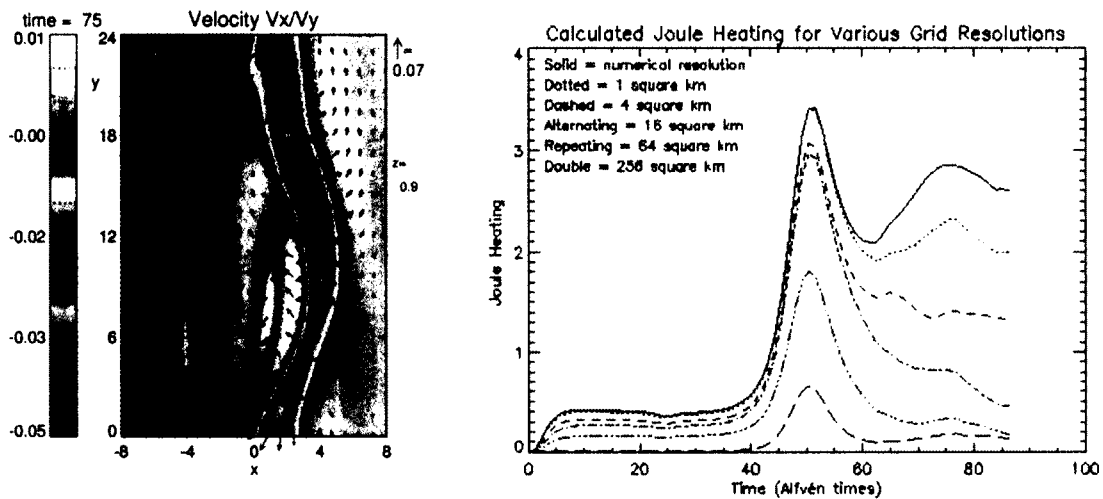


**Figure 4.6 Velocity Perturbations and Joule Heating for a Shear Rate of 0.75 (Boundary Conditions A)**

### **Boundary Conditions B**

For the Boundary Conditions B case, one observes similar behavior for the Joule heating for various scales, for varying shear rate applied at the top of the simulation (Fig. 4.7, Fig. 4.8, Fig. 4.9, and Fig. 4.10). These plots are for nominal ionospheric conductivity. However, the magnitudes of the Joule heating are much higher. This is due to the fact that the currents (Pedersen) are closing more realistically in the ionosphere, and thus more energy is being deposited in the ionosphere—rather than flowing freely through the bottom of the simulation, as was the case with Boundary Conditions A.

There is a curious lack of the turbulence after the peak, that is evident in the Boundary Conditions A case(s). This may be due to the fact that these plots were generated at too low an altitude for this case ( $\sim 120$  km above the Earth's surface).

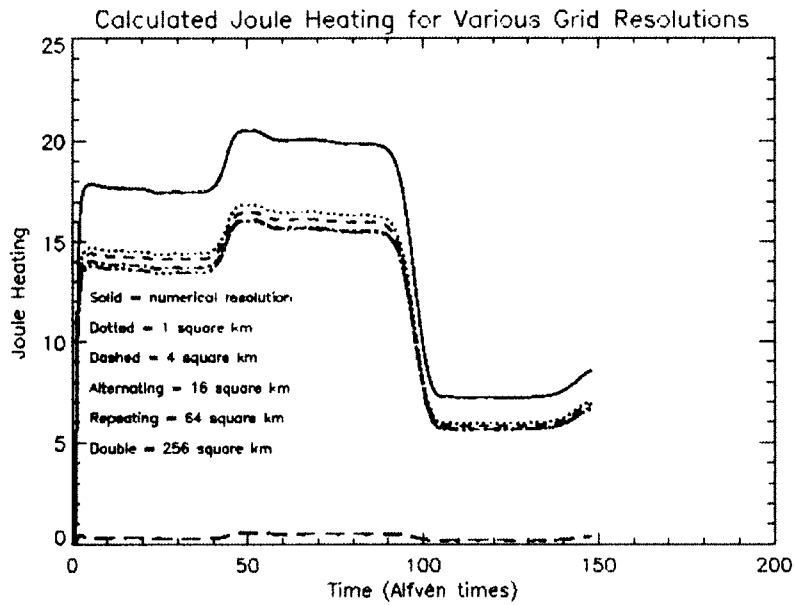


**Figure 4.7 Joule Heating for a Shear Rate of 0.25 (Boundary Conditions B)**

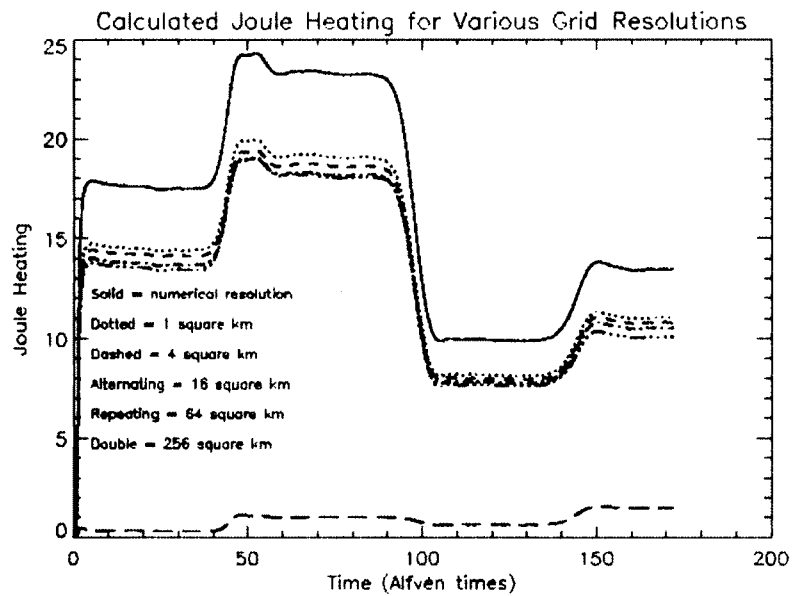


**Figure 4.8 Joule Heating for a Shear Rate of 0.50 (Boundary Conditions B)**

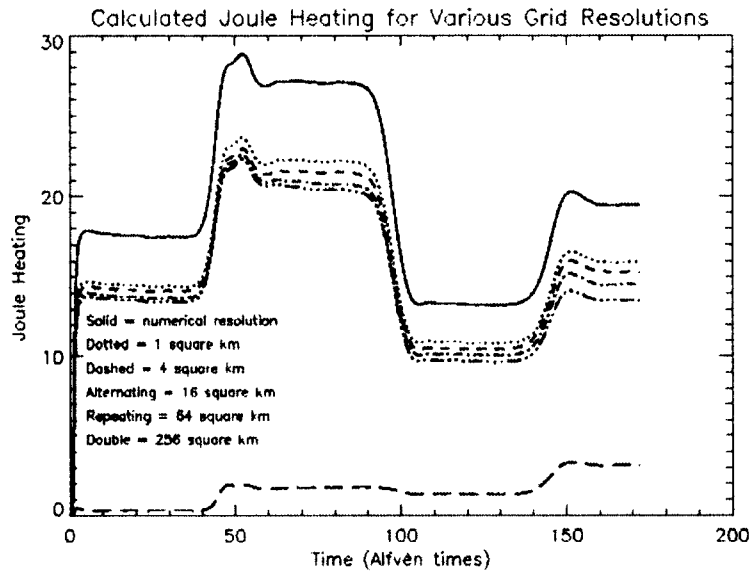


**Figure 4.9 Joule Heating for a Shear Rate of 0.75 (Boundary Conditions B)**

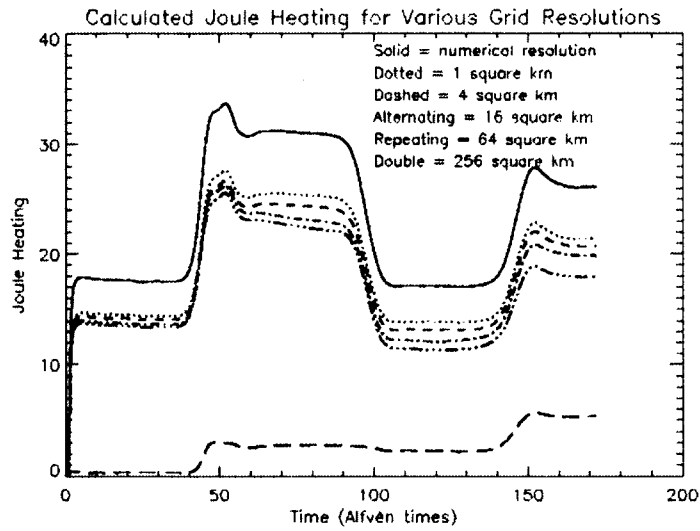


**Figure 4.10 Joule Heating for a Shear Rate of 1.00 (Boundary Conditions B)**

## Discussion

For both the Boundary Conditions A, Fig. 4.11, and the Boundary Conditions B, Fig. 4.12, cases, the maximum amount of Joule heating (the peak) varied linearly with the applied shear rate. This is a fully reasonable result, as the shear rate provides a direct measure of the energy input into the system (in the form of Poynting flux).

As the neutral dynamics are turned off in the code, and the neutrals are initialized to be at rest—the neutral wind contribution to the Joule heating is zero. It should be noted again that ignoring the neutral wind may result in an overestimation of the Joule heating by as much as 40%, or an underestimation by as much as 400% (Thayer 1998).

The Boundary Conditions A cases displayed a—truly remarkable—degree of fine structure, both spatially and temporally. It would appear that one would need to go to (at least) a scale size at the numerical resolution ( $\sim 0.1$  km in  $x$ ,  $\sim 0.4$  km in  $y$ ), and a temporal resolution of around 1 Alfvén time ( $\sim 1.1$  seconds), to adequately resolve the correct value of the Joule heating. The Boundary Conditions B case(s) showed less turbulence/fine structure—possibly due to these plots being generated at too low a height ( $\sim 120$  km).

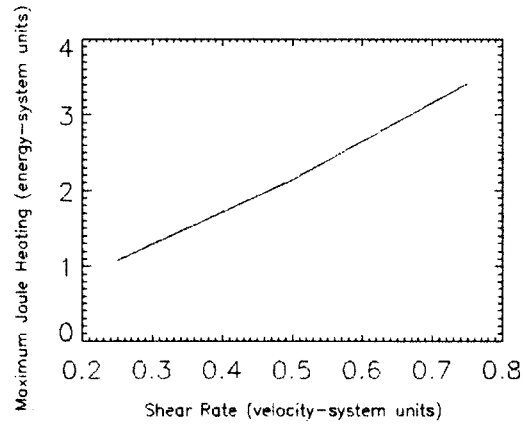


**Figure 4.11 Peak of Joule Heating vs. Shear Rate (Boundary Conditions A)**

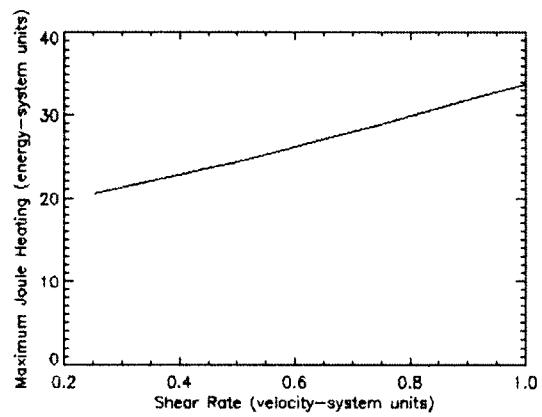


**Figure 4.12 Peak of Joule Heating vs. Shear Rate (Boundary Conditions B)**

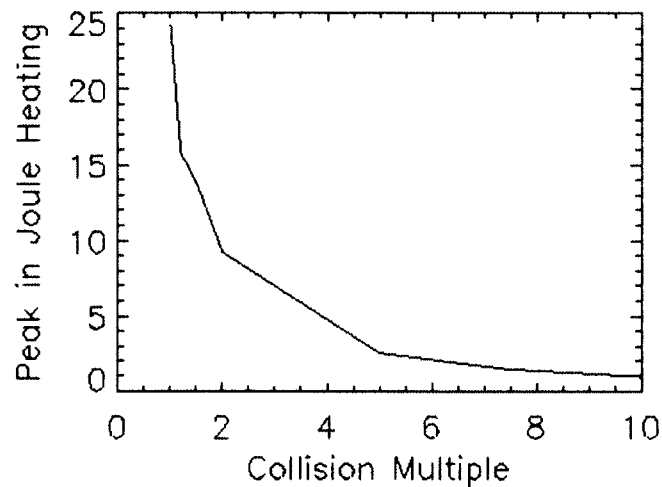


**Figure 4.13 Peak vs. Collision Multiple (Conductivity) for New Boundary Conditions for Reference Shear (0.5). This Is For a Height of Approximately 120 km.**

As shown in Fig 4.13, an increase in the Pedersen conductivity, results in a lowering of the (magnitude of the) peak of Joule heating. This corresponds to a larger proportion of currents closing higher in the simulation box, thus less energy being deposited near the lower boundary.

In this chapter, we investigated the Joule heating for various scale sizes in the region of fine scale structure, that is, in the region of discrete aurora. A means of making quantitative measurements of the Joule heating was expounded and developed. The behavior of the system for two different lower boundary conditions was investigated. Boundary Conditions A allowed for magnetic perturbations to flow out of the bottom of the simulation domain; Boundary Conditions B closed off the lower ionosphere (The velocity perturbations at the lower boundary are set to zero.)—and enabled the system to close more realistically through the Pedersen

currents. This caused more energy to be deposited in the lower ionosphere—as evidenced by larger values of the Joule heating.

The arrival of the Alfvén wave from the top of the simulation was clearly visible, as a peak in the Joule heating. This mapped linearly with the shear rate. This was reasonable—as the shear rate was a measure of how much energy was input into the system.

In Emery, Lathuiller, Richards, Roble, Buonsanto, Knipp, Wilkenson, Sipler, and Niecejewski (1999), it is stated that the under-representation of the Joule heating is as high as a factor of 2. Rodger, Wells, Moffett, and Bailey (2001) stated that the underestimation of the Joule heating is  $\sim 20\%$ , with an upper value of  $65\%$ . Our simulation of small spatial and temporal scales showed that the large-scale averaged estimate of the Joule heating may be off by as much as a factor of 8, in the presence of small structures. Qualitatively, this large increase in the Joule heating is due to vary rapid spatial and temporal changes in the velocity profile, at an altitude of  $\sim 120$  km. The model enabled a study of this on smaller spatial and temporal scales than previously possible.

This model quantifies the amount of Joule heating generated in small-scale auroral structures. According to the model results, an (approximately as high as a factor of eight) change was found from the smallest to largest scale averaging.

## Chapter 5 Conclusions

The reflection of an Alfvén wave from the ionosphere was successfully modeled. This was performed for both Boundary Conditions A and Boundary Conditions B.

The initial resistivity perturbation has been shown to be a source of Alfvén wave generation. This is particularly evident in the first two frames of both Figures 3.9 and 3.23. Alfvén waves have been shown to “map” from the perturbation region, all the way down to the bottom of the ionosphere, and back. These Alfvén waves, traveling downward from the reconnection region, carry with them a magnetic perturbation, resulting in a current, and a parallel electric field, in the presence of a localized resistivity. These waves are responsible for the deformation of the current sheet.

The edges of this current sheet have been shown to have waves of Alfvénic character. It is these Alfvénic structures, that carry with them both velocity and magnetic perturbations, which are responsible for both the anti-parallel velocity shear and the electric field, pointing outwards from the (electron) precipitation region(s). In addition, upon visual inspection, the appearance of the (electron) precipitation region, is very similar to that of actual discrete aurora. At their reflection at the bottom of the simulation domain (the ionosphere), these regions



become quite thin (due to the narrowing of the current sheet)—again, a very (discrete arc) aurora-like feature.

The parameters of the system were varied, to produce differing conductivities. The behavior of these conductivities was as expected—except for the behavior of the “Density” run. The failure of an increase in plasma density to increase the Pedersen conductivity as expected, points to the possibility that the assumptions of the model are not entirely correct, or, at least, not entirely complete.

It was shown that it was more likely that an increased conductance would shut off the magnetic reconnection—with a resultant loss of discrete aurora-like characteristics. However, the mechanism for this is uncertain.

Realistic ionospheric conductivities were reproduced. They ranged from approximately  $4.18 \times 10^{-6}$  to  $2.62 \times 10^{-5}$  Siemens (c.f. **Fig. 3.27**).

In chapter 4, the Joule heating for various scale sizes was investigated in the region of fine scale structure. That is, in the region of discrete aurora. A means of making quantitative measurements of the Joule heating was expounded and developed. The behavior of the system for two different lower boundary conditions was investigated. The original boundary conditions allowed for magnetic perturbations to flow out of the bottom of the simulation domain; the new boundary condition closed off the lower ionosphere, and enabled the system to close more realistically through the Pedersen currents. This caused more energy to be

deposited in the lower ionosphere—as evidenced by larger values of the Joule heating.

For both the Boundary Conditions A case, and the Boundary Conditions B case, the maximum amount of Joule heating (the peak) varied linearly with the applied shear rate. This is a fully reasonable result, as the shear rate provides a direct measure of the energy input into the system.

As the neutral dynamics are turned off in the code, and the neutrals are initialized to be at rest, the neutral wind contribution to the Joule heating is zero. It should be noted that ignoring the neutral wind may result in an overestimation of the Joule heating by as much as 40%, or an underestimation by as much as 400% (Thayer 1998).

The Boundary Conditions A cases displayed a—truly remarkable—degree of fine structure, both spatially and temporally. It would appear that one would need to go to (at least) numerical grid resolution ( $\sim 0.1$  km in  $x$ ,  $\sim 0.4$  km in  $y$ ), and a temporal resolution of around 1 Alfvén time ( $\sim 1.1$  seconds), to successfully resolve the correct value for the Joule heating. The Boundary Conditions B case(s) showed less turbulence/fine structure—possibly due to these plots being generated at too low a height ( $\sim 120$  km).

It was shown that an increase in the Pedersen conductivity results in a lowering of the (magnitude of the) peak of Joule heating. This corresponds to a larger proportion of currents closing higher in the simulation box, thus less energy being deposited near the lower boundary.

The Joule heating was investigated for various scale sizes in the region of fine scale structure, that is, in the region of discrete aurora. A means of making quantitative measurements of the Joule heating was expounded and developed. The behavior of the system for two different lower boundary conditions was investigated. Boundary Conditions A allowed for magnetic perturbations to flow out of the bottom of the simulation domain; Boundary Conditions B closed off the lower ionosphere (The velocity perturbations at the lower boundary are set to zero.), and enabled the system to close more realistically through the Pedersen currents. This caused more energy to be deposited in the lower ionosphere—as evidenced by larger values of the Joule heating.

The arrival of the Alfvén wave from the top of the simulation was clearly visible, as a peak in the Joule heating. This mapped linearly with the shear rate. This was reasonable—as the shear rate was a measure of how much energy was input into the system.

In Emery, (1999), it is stated that the under-representation of the Joule heating is as high as a factor of 2. Rodger, Wells, Moffett, and Bailey (2001) stated

that the underestimation of the Joule heating is  $\sim 20\%$ , with an upper value of 65%. Our simulation of small spatial and temporal scale showed that the large-scale averaged estimate of the Joule heating may be off by as much as a factor of 8, in the presence of small structures. This model provides quantitatively accurate measurements of the amount of Joule heating generated in small-scale auroral structures. A strong (approximately factor as high as eight) change was found from the smallest to largest scale averaging.

There are many outstanding issues involved with the formation and time evolution of discrete auroral arcs, namely: the narrowness of arcs; current sheet structures above arcs; electric fields extending parallel outwards from the arcs; fast (plasma) flows in the region of discrete arcs; and the formation and maintenance of parallel (to the magnetic “guide field”) electric fields—deep into the ionosphere.

The model has reproduced, qualitatively and semi-quantitatively, the features of discrete auroral arcs, and their time evolution. The lower regions of the simulation domain reproduced the attributes of discrete auroral arcs: a thin [mostly electron] precipitation region, electric fields extending out perpendicularly to said region—and velocity shear parallel to it. This has been achieved in a fully self-consistent manner.

Major theoretical underpinnings of this work have been previously postulated (notably Otto and Birk 1993 and Zhu, Otto, Lummerzheim, Rees and

Lanchester 2001). Performing the simulations in three dimensions, as well as determining which input parameters (e.g. shear rate—that is, a measure of the amount of energy inputted into the system; conductance, Pedersen conductivity) lead to a “switching on” or a “switching off” of those properties which lead to auroral arc formation ([magnetic] reconnection) is the major contribution of the present work.

In addition, the explicit parallelization of a very complex (coupled partial differential equations) extant code, for a generalized parallelization scheme, and a generalized grid—as well as the development of a routine to automatically calculate the Joule heating, for a generalized set of scale sizes, are key contributions. Both represent significant achievements in both code design and implementation.

There remain some open issues in the study. For one, a better understanding of the mechanism by which an increased ionospheric conductivity is more likely to shut off the magnetic reconnection in the system, thus causing a loss of the properties of discrete aurora. Also, it is not clear why for the Boundary Conditions B case, there is less turbulence in the Joule heating, than for the Boundary Conditions A case. This may be a consequence of choosing too low an altitude for making measurements. Both topics present possibilities for further study.

## References

- Akasofu, S.-I., S. Chapman, and P.C. Kendall. "Aurora and Airglow." Edited by B.M. McCormac. New York: Reinhold, 1967.
- Albert, R.D. and P.J. Lindstrom. "Auroral-particle precipitation and trapping caused by electrostatic double layers." *Science* 170 (1970): 1398.
- Alfvén, H., and C.-G. Fälthammar. *Cosmical Electrodynamics*. Vol. 3.2.1. London: Oxford at the Clarendon Press, 1963.
- Atkinson, G. "Mechanism by which merging at X lines causes discrete auroral arcs." *J. Geophys. Res.* 97 (1992): 1337.
- Atkinson, G., F. Creutzberg, and R.L. Gattinger. "Interpretation of complicated discrete arc structure and behavior in terms of multiple X lines." *J. Geophys. Res.* 94 (1989): 5292.
- Axford, W. "Magnetospheric convection." *Rev. Geophys.* 7 (1969): 421.
- Baumjohann, W. and R. A. Treumann. "Basic Space Plasma Physics," Imperial College Press, 1997.
- Bingham, R., D.A. Bryant, and D.S. Hall. "Auroral electron acceleration by lower-hybrid waves." *Ann. Geophys.* 6 (1988): 159.
- Bingham, R., D.A. Bryant, and D.S. Hall, A wave model for the aurora. *Geophys. Res. Lett.* 11 (1984): 327.
- Birk, G.T. and Otto, A. "A three-dimensional plasma-neutral gas-fluid code." *Journal of Computational Physics* 125 (1996): 513.
- Birn, J., M. Hesse, and K. Schindler. "What determines the latitudinal extent of the auroral acceleration region?" *J. Atmos. Terr. Phys.*, 1992: 513.
- Birn, J. and M. Hesse. "The substorm current wedge and field-aligned currents in MHD simulations of magnetotail reconnection." *J. Geophys. Res.* 96 (1991): 1611.
- Block, L.P. "Magnetospheric Currents, Geophys. Mongr. Ser." Edited by T.A. Potemra. Vol. 28. Washington, D.C.: AGU, 1984.
- Block, L.P. "A double layer Review." *Astrophys. Space Sci.* 55 (1978): 59.

- Block, L.P. "Double Layers." In "Physics of the Hot Plasma in the Magnetosphere," edited by B. Hultqvist and L. Stenflo, 229. New York: Plenum, 1975.
- Block, L.P. "Potential double layers in the ionosphere." *Cosmic Electrodyn.* 3 (1972): 349.
- Borovsky, J. E. "Auroral arc thicknesses as predicted by various theories." *Journal of Geophysical Research* 98 (1993): 6101.
- Bryant, D.A., D.S. Hall, and R. Bingham. "Auroral Physics." Edited by M.J. Rycroft, and L.A. Frank C.-I. Meng. New York: Cambridge University Press, 1991.
- Bryant, D.A., A.C. Cook, Z.-S. Wang, U. de Angelis, and C.H. Perry. "Turbulent acceleration of auroral electrons." *J. Geophys. Res.* 96 (1991): 13829.
- Bujarbarua, S. and K.S. Goswami. "Weak ion acoustic double layers and solitary waves on the auroral field lines." *J. Geophys. Res.* 90 (1985): 7611.
- Bythrow, P.F., R.A. Heelis, W.B. Hanson, R.A. Power, and R.A. Hoffman. "Observational evidence for a boundary layer source of dayside region 1 field-aligned currents." *J. Geophys. Res.* 86 (1981): 5577.
- Calvert, W. "Auroral precipitation caused by auroral kilometric radiation." *J. Geophys. Res.* 92 (1987): 8792.
- Calvert, W. "A feedback model for the source of auroral kilometric radiation." *J. Geophys. Res.* 87 (1982): 8199.
- Carlqvist, P. and R. Bostrom. "Space-charge regions above the aurora." *J. Geophys. Res.* 75 (1970): 7140.
- Chiu, Y.T., A.L. Newman, and J.M. Cornwall. "On the structures and mapping of auroral electrostatic potentials." *J. Geophys. Res.* 86 (1981): 10029.
- Chiu, Y.T, and J.M. Cornwall. "Electrostatic model of a quiet auroral arc." *J. Geophys. Res.* 85 (1980): 543.
- Codrescu, M. V., T. J. Fuller-Rowell, J. C. Foster, J. M. Holt, and S. J. Cariglia, "Electric field variability associated with the Millstone Hill electric field model." *Journal of Geophysical Research* 105 (March 2000): 5265-5274.
- Crooker, N. U., R. A. Greenwald, M. Hesse, M. K. Hudson, W. J. Hughes, L. R. Lyons, N. C. Maynard, C. T. Ryssel, and G. L. Siscoe, "Report from the first geospace environment modeling GEM campaigns: 1991-1997", p. cover, Space Science Center, IGPS, UCLA, 1999.
- Dungey, J.W. "Thinning of field-aligned currents." *Geophys. Res. Lett.* 9 (1982): 1243.

Eastman, T.E., E.W. Hones, S.J. Barne, and J.R. Asbridge. "The magnetospheric boundary layer: Site of plasma, momentum and energy transfer from the magnetosheath into the magnetosphere." *Geophys. Res. Lett.* 3 (1976): 685.

Emery, B. A., Lathuiller, C., Richards, P. G., Roble, R. G., Buonsanto, M. J., Knipp, D. J., Wilkenson, P., Sipler, D. P., and Niciejewski, R. "Time dependent thermospheric neutral response to the 2 - 11 november 1993 storm period." *Journal of Atmospheric Terrestrial Physics* 61 (1999): 329.

Fuller-Rowell, T. J. "A two-dimensional, high-resolution, nested-grid model of the thermosphere. II - response of the thermosphere to narrow and broad electrodynamic features." *Journal of Geophysical Research* 90 (July 1985): 6567-6586.

Fuller-Rowell, T. and Rees, D. "A three-dimensional and time-dependent global model of the thermosphere." *Journal of Atmospheric Science* 37 (1980): 2545.

Galeev, A.A. "High-Latitude Space Plasma Physics." Edited by B. Hultqvist and T. Hagfors. New York: Plenum, 1983.

Galperin, Y.I., A.V. Volosevich, and L.M. Zelenyi. "Pressure gradient structures in the tial neutral sheet as 'roots of the arcs' with some effects of stochasticity." *Geophys. Res. Lett.* 19 (1992): 2163.

Galperin, Y.I. and A.V. Volosevich. "The ARCAD-3 Project and the theory of auroral structures." *Can. J. Phys.* 67 (1989): 719.

Goertz, C.K. "Heating and cooling of the Earth's plasma sheet." *Adv. Space Res. Suppl.* 10 (1990): 29.

Goertz, C.K. "Auroral arc formation: Kinetic and MHD effects." *Space Sci. Rev.* 42 (1985): 499.

Goertz, C.K. "Kinetic Alfvén waves on auroral field lines." *Planet. Space Sic.* 32 (1984): 1387.

Goertz, C.K. "Eur. Space Agency Sec. Publ." *Sixth ESA Symposium on European Rocket and Balloon Programmes.* 1983. 221.

Goertz, C.K. and R.W. Boswell. "Magnetosphere-ionosphere coupling." *J. Geophys. Res.* 84 (1979): 7239.

Gurnett, D.A. "Electric field and plasma observations in the magnetosphere." Edited by E.R. Dyer. Washington, D.C.: National Academy of Sciences, 1972.

Haerendel, G., S. Buchert, C. La Hoz, B. Raaf, and E. Rieger. "On the proper motion of auroral arcs." *Journal of Geophysical Research* 98, no. A4 (April 1993): 6087-6099.



- Harel, M., Wolf, R., Reiff, P., Spiro, R., Burke, W., Rich F., and Smiddy, M. "Quantitative simulation of a magnetospheric substorm, 1, model logic and overview." *J. Geophys. Res.* 86 (1981): 1981.
- Harrold, B.G., C.K. Goertz, R.A. Smith, and P.J. Hansen. "Resonant Alfvén wave heating of the plasma sheet boundary layer." *J. Geophys. Res.* 95 (1990): 15030.
- Hasegawa, A. and T. Sato. "Dynamics of the Magnetosphere." Edited by S.-I. Akasofu. Highham, Mass.: D. Reidel, 1979.
- Hasegawa, A. and L. Chen. "Kinetic process of plasma heating by resonant conversion of Alfvén wave." *Phys. Fluids* 19 (1976): 1924.
- Heikkila, W.J. "Magnetospheric Currents, Geophys. Monogr. Ser." Edited by T.A. Potemra. Vol. 28. Washington, D.C.: AGU, 1984.
- Hubbard, R.F. and G. Joyce. "Simulation of auroral double layers." *J. Geophys. Res.* 84 (1979): 4297.
- Hudson, M.K. and D.W. Potter. "Physics of Auroral Arc Formation, Geophys. Monogr. Ser." Edited by S.-I. Akasofu and J.R. Kan. Vol. 25. Washington, D.C.: AGU, 1981.
- Hudson, M.K. and F.S. Mozer. "Electrostatic shocks, double layers, and anomalous resistivity in the magnetosphere." *Geophys. Res. Lett.* 5 (1978): 131.
- Hudson, M.K., T.L. Crystal, W. Lotko, and C. Barnes. "Weak double layers in the auroral ionsosphere." *Laser Part. beams* 5 (1987): 295.
- Hudson, M.K., W. Lotko, I. Roth, and E. Witt. "Solitary waves and double layers on auroral field lines." *J. Geophys. Res.* 88 (1983): 916.
- Hultqvist, B. "On the Production of a magnetic-field-aligned electric field by the interaction between the hot magnetospheric plasma and the cold ionosphere." *Planet. Space Sci.* 19 (1971): 749.
- Ionson, J.A., R.S.B. Ong, and E.G. Fontheim. "Anomalous resistivity of the auroral plasma in the top-side ionosphere." *Geophys. Res. Lett.* 3 (1976): 549.
- Kan, J. R. "A globally integrated substorm model: Tail reconnection and magnetosphere-ionosphere coupling." *Journal of Geophysical Review* 103 (1998): 11787-11796.
- Kan, J.R., and Lee, L.C. "Theory of imperfect magnetosphere-ionosphere coupling." *Geophys. Res. Lett.* 7 (1980): 633.

- Kan, J.R. and S.-I. Akasofu. "Energy source and mechanisms for accelerating the electrons and driving the field-aligned current of the discrete auroral arc." *J. Geophys. Res.* 81 (1976): 5123.
- Kan, J.R. "Energization of auroral electrons by electrostatic shock waves." *Journal of Geophysical Research* 80 (1975): 2089-2096.
- Kern, J.W. "Physics of Geomagnetic Phenomena." Edited by S. Matsushita and W.H. Cambell. San Diego, Calif.: Academic, 1967.
- Kitashirakawa-Oiwake C. and Sakyoku, "On the ionospheric conductivity", <http://wdc.kugi.kyoto-u.ac.jp/ionocond/exp/icexp.html>, World Data Center for Geomagnetism, Kyoto, Graduate School of Science, Kyoto University, Kyoto, Japan, July 2011.
- Kosch, M. J. and E. Nielsen, "Coherent radar estimates of average high-latitude ionospheric Joule heating." *Journal of Geophysical Research* 100 A7 (1995): 12201-12215.
- Lanchester, B. S., M. H. Rees, D. Lummerzheim, A. Otto, K. J. F. Sedgemore-Schulthess, H. Zhu, and I. W. McCrea, "Ohmic heating as evidence for strong field-aligned currents in filamentary aurora." *Journal of Geophysical Research* 106 A2, (2001): 1785-1794.
- Lee, L. C. and Kan J. R. "Auroral double layer." in "Physics of Auroral Arc Formation," edited by S.-I. Akasofu and Kan J. R., 245-251. Washington, D.C.: AGU, 1981.
- Lennartsson, W. "On the role of magnetic mirroring in the auroral phenomena." *Astrophys. Space Sci.* 51 (1977): 461.
- Lennartsson, W. "On the magnetic mirroring as the basic cause of parallel electric fields." *J. Geophys. Res.* 81 (1976): 5583.
- Leontyev, S.V. and V.B. Lyatskiy. "Longitudinal electric fields in an Alfvén wave." *Geomagn. Aeron.* 20 (1980): 196.
- Lotko, W. and C.G. Schultz. "Modeling Magnetospheric Plasma, Geophys. Monogr. Ser." Edited by T.E. Moore and J.H. Waite. Vol. 44. Washington, D.C.: AGU, 1988.
- Lotko, W., B.U.O. Sonnerup, and R.L. Lysak. "Nonsteady boundary layer flow including ionospheric drag and parallel electric fields." *J. Geophys. Res.* 92 (1987): 8635.
- Lotko, W. "Diffusive acceleration of auroral primaries." *J. Geophys. Res.* 91 (1986): 191.
- Lotko, W. and C.F. Kennel. "Spiky ion acoustic waves in collisionless auroral plasma." *J. Geophys. Res.* 88 (1983): 381.

- Lui, A.T.Y., E.W. Hones, F. Yasuhara, S.-I. Akasofu, and S.J. Bame. "Magnetotail plasma flow during plasma sheet expansions: VELA 5 and 6 and IMP 6 observations." *J. Geophys. Res.* 82 (1977): 1235.
- Lundin, R. and D.S. Evans. "Boundary layer plasmas as a source for high-latitude, early afternoon, auroral arcs." *Planet. Space Sci.* 32 (1985): 1389.
- Lyons, L.R. "Auroral Physics." Edited by M.J. Rycroft, and L.A. Frank C.-I. Meng. New York: Cambridge University Press, 1991.
- Lyons, L.R. and D.S. Evans. "An association between discrete aurora and energetic particle boundaries." *J. Geophys. Res.* 89 (1984): 2395.
- Lyons, L.R. "Discrete auroral as the direct result of an inferred high-altitude generation potential distribution." *J. Geophys. Res.* 86 (1981): 1.
- Lyons, L.R. "Generation of large-scale regions of auroral currents, electric potentials, and precipitation by the divergence of the convection electric field." *J. Geophys. Res.* 85 (1980): 17.
- Lysak, R.L. "Feedback instability of the ionospheric resonant cavity." *J. Geophys. Res.* 96 (1991): 1553.
- Lysak, R.L. "Electrodynamic coupling of the magnetosphere and ionosphere" *Space Science Reviews.*, 52 (1990), 33-87
- Lysak, R.L. "Coupling of the dynamic ionosphere to auroral flux tubes." *J. Geophys. Res.* 91 (1986): 7047.
- Lysak, R.L. and C.T. Dum. "Dynamics of magnetosphere-ionosphere coupling including turbulent transport." *J. Geophys. Res.* 88 (1983): 365.
- Lysak, R.L. and C.W. Carlson. "The effect of microscopic turbulence on magnetosphere-ionosphere coupling." *Geophys. Res. Lett.* 8 (1981): 296.
- Maggs, J. E. and Davis, T. N. "Measurements of the thickness of auroral structures." *Planetary Space Science* 16 (1968): 205.
- Maurits, S. A. and Watkins, B. J. "UAF Eulerian model of the polar ionosphere." Edited by R. W. Schunk. "Solar Terrestrial Energy Program (STEP) Handbook of Ionospheric Models." Logan, UT: Utah State University, 1996. 95-123.
- McIlwain, C.E. "Direct measurements of particles producing visible aurora" *J. Geophys. Res.* 65 (1960), 2727.
- Mozer, F.S. "Magnetospheric Particles and Fields." Edited by B.M. McCormac. Higham, Mass.: D. Reidal, 1976.

- Ogawa, T. and T. Sato. "New mechanism of auroral arcs." *Planet. Space Sci.* 19 (1971): 1393.
- Onsager, T.G., M.F. Thomsen, R.C. Elphic, and J.T. Gosling. "Model of electron and ion distributions in the plasma sheet boundary layer." *J. Geophys. Res.* 96 (1991): 20999.
- Otto, A., "Properties of two- and three-dimensional magnetic reconnection," *Physica Scripta*, T 74, 9, 1998.
- Otto, A. and G. T. Birk, "Formation of Thin Auroral Arcs by Current Striation," *Geophysical Research Letters* (1993): 2833-2836.
- Palmadesso, P.J., T. Coffey, S.L. Osakow, and K. Papadopoulos. "Topside ionosphere ion heating due to electrostatic ion cyclotron turbulence." *Geophys. Res. Lett.* 1 (1974): 105.
- Papadopoulos, K. "A review of anomalous resistivity for the ionosphere." *Rev. Geophys. Space Phys.* 15 (1977): 113.
- Parks, George K. "Physics of Space Plasmas." Seattle, Washington: Perseus Publishing, 1991.
- Persson, H. "Electric field parallel to the magnetic field in a low-density plasma." *Phys. Fluids* 9 (1966): 1090.
- Persson, H. "Electric field along a magnetic line of force in a low-density plasma." *Phys. Fluids* 6 (1963): 1756.
- Ponyavin, D.I., M.I. Pudovkin, and S.S. Sazhin. "Self-consistent field-aligned electric field in the Earth's magnetosphere." *Geomagn. Aeron.* 17 (1977): 323.
- Prakash, M. and R.L. Lysak. "Resistivity due to weak double layers: a model for auroral arc thickness." *Geophys. Res. Lett.* 19 (1992): 2159.
- Roble, R. G., Ridley, and Dickinson, R. E. "On the Global Mean Structure of the Thermosphere." *Journal of Geophysical Research* 92 (1987): 8745.
- Roble, R. G. and Rees, M. H. "Time-dependent studies of the aurora: Effects of particle precipitation on the dynamic morphology of ionospheric and atmospheric properties." *Planetary Space Science* 25 (1977): 991.
- Rodger, A. S., G. D. Wells, R. J. Moffett, and G. J. Bailey. "The variability of Joule heating, and its effects on the ionosphere and thermosphere." *Annales Geophysicae* 19 (2001): 773-781.
- Rostoker, G. and R. Bostrom. "A mechanism for driving the gross Birkeland current configuration in the auroral oval." *J. Geophys. Res.* 81 (1976): 235.

- Rothwell, P.L., M.B. Silevitch, L.P. Block, and C.-G. Falthammar. "Prebreakup arcs: A comparison between theory and experiment." *J. Geophys. Res. Lett.* 96 (1991): 13967.
- Sato, T. and T. Iijima. "Primary sources of large-scale Birkeland currents." *Space Sci. Rev.* 24 (1979): 347.
- Sato, T. "A theory of quiet auroral arcs." *J. Geophys.* 56 (1978): 1042.
- Sato, T. and T.E. Holzer. "Quiet auroral arcs and electrodynamic coupling between the ionosphere and the magnetosphere, 1." *J. Geophys. Res.* 78 (1973): 7314.
- Scholer, M. "On the motion of artificial ion clouds in the magnetosphere." *Planetary and Space Science* 18 (1970): 977.
- Schunk, R. W. "A mathematical model of the middle and high latitude ionosphere." *Pure Appl. Geophys.* 127 (1988): 255.
- Schunk, R. W. "The terrestrial ionosphere." *Solar-Terrestrial Physics: Principles and Theoretical Foundations* (D. Reidel), 1983: 609-676.
- Seyler, C. E. "A mathematical model of the structure and evolution of small-scale discrete auroral arcs." *Journal of Geophysical Research* 95 (1990): 17199.
- Smith, R.A. "Anomalous transport in discrete arcs and motion of double layers in a model auroral circuit." *Laser beams* 5 (1987): 381.
- Smith, R.A. "Simulation of double layers in a model circuit with nonlinear impedance." *Geophys. Res.* 13 (1986a): 809.
- Smith, R. A. "Effects of anomalous transport on the potential discrete auroral arcs." 13 (1986b): 889.
- Sojka, J.J. "Global scale, physical models of the F region ionosphere." *Revue Geophysical* 27 (1989): 371.
- Song, Y. and R.L. Lysak. "Modeling Magnetospheric Plasmas." Edited by T.E. Moore and J.H. Waite. Washington, D.C., 1988.
- Sonnerup, B.U.O. "Theory of the low-latitude boundary." *J. Geophys. Res.* 85 (1980): 2017.
- Stasiewicz, K. "On the origin of the auroral inverted-V spectra." *Planet. Space Sci.* 32 (1984): 379.
- Swift, D.W. "A two-dimensional particle code simulation of inertial Alfvén waves and auroral electron acceleration." *Journal of Geophysical Research* 112 (January 2007).

- Swift, D.W. "Numerical simulation of the generation of electrostatic turbulence in the magnetotail." *J. Geophys. Res.* 86 (1981a): 2273.
- Swift, D.W. "Physics of Auroral Arc Formation, Geophys. Monogr. Ser." Edited by S.-I. Akasofu and J.R. Kan. Vol. 25. Washington, D.C.: AGU, 1981b.
- Swift, D.W. "An equipotential model for auroral arcs: The theory of two-dimensional laminar electrostatic shocks." *J. Geophys. Res.* 84 (1979a): 6427.
- Swift, D.W. "On the structure of auroral arcs: The results of numerical simulations." *J. Geophys. Res.* 84 (1979b): 469.
- Swift, D.W. "Turbulent generation of electrostatic fields in the magnetosphere." *J. Geophys. Res.* 82 (1977): 5143.
- Swift, D.W. "An equipotential model for auroral arcs 2. Numerical simulations." *J. Geophys. Res.* 80 (1976): 3935.
- Swift, D. W. "On the formation of auroral arcs and acceleration of auroral electrons." *Journal of Geophysical Research* 80 (1975): 2096.
- Temerin, M.A. and D. Cravens. "Production of electron conics by stochastic acceleration parallel to the magnetic field." *J. Geophys. Res.* 95 (1990): 4285.
- Temerin, M.A., J. McFadden, M. Boehm, C.W. Carlson, and W. Lotko. "Production of flickering aurora and field-aligned electron flux by electromagnetic ion cyclotron waves." *J. Geophys. Res.* 91 (1986): 5769.
- Thayer, J. P. "Height-resolved Joule heating rates in the high-latitude E region and the influence of neutral winds." *Journal of Geophysical Research* 103 A1 (1998): 471-487.
- Trondsen, T S. and Cogger, L. L. "Fine-scale optical observations of aurora." *Physics and Chemistry of the Earth Part C* 26, no. 1-3 (January 2001): 179-188.
- Trondsen, T. S. and Cogger, L. L. "A survey of small-scale spatially periodic distortions of auroral forms." *Journal of Geophysical Research* 103 (May 1998): 9405-9416.
- Vasyliunas, V.M. "Magnetospheric Processes." Hingham, Massachusetts: D. Reidel, 1972.
- Vasyliunas, V.M. "Mathematical models of magnetospheric convection and its coupling to the ionosphere." *Particles and Fields in the Magnetosphere*, 1970a: 60.
- Vasyliunas, V.M. "Particles and Fields in the Magnetosphere." Edited by B.M. McCormac. Hingham, Mass.: D. Reidel, 1970b.

Vogt, J. "Shear velocity profiles associated with auroral curls." *Journal of Geophysical Research* 104 (1999), No. A8, 17,277-17,288.

Watanabe, K. and T. Sato. "Self-excitation of auroral arcs in a three-dimensionally coupled magnetosphere-ionosphere system." *Geophys. Res. Lett.* 15 (1988): 717.

Weimer, D.R., C.K. Goertz, D.A. Gurnett, N.C. Maynard, and J.L. Burch. "Auroral zone electric fields from DE 1 and 2 at magnetic conjunctions." *J. Geophys. Res.* 90 (1985): 7479.

Wolf, R., Harel, R. Spiro, G. H. Voigt, P. Reiff, Chen, C. K. "Computer simulation of inner magnetospheric dynamics for the magnetic storm of July 29, 1977." *Journal of Geophysical Research* 87 (1982): 5949.

Zhu, H., Otto, A., Lummerzheim, D., Rees, M. H., and Lanchester, B. H. "Ionosphere-magnetosphere simulation of small-scale structure and dynamics." *Journal of Geophysical Research* 106 (2001): 1795-1806.

## Appendix A

### Fitting scheme

### Integration Methods

The numerical techniques employed by the code were Dufort-Frankel (Leapfrog) and Lax-Wendroff integration methods. For the main integration, the Leapfrog method was employed. For example, in a 1-D case:

$$T_j^{n+1} = T_j^{n-1} - C(T_{j+1}^n - T_{j-1}^n) \quad (\text{Equation A.1})$$

Consider a simple equation of the form:

$$\frac{\partial T}{\partial t} = -v \frac{\partial T}{\partial x}$$

... which would yield a value for the constant C:

$$C = \frac{v\Delta t}{\Delta x}$$

Note that superscripts denote the time index:  $n + 1$   $\equiv$  centered in present time +  $\Delta t$ ,  $n$   $\equiv$  present time, etc. The subscripts denote the spatial index:  $j + 1$   $\equiv$  centered in space +  $\Delta x$ ,  $n$   $\equiv$  centered in space, etc.



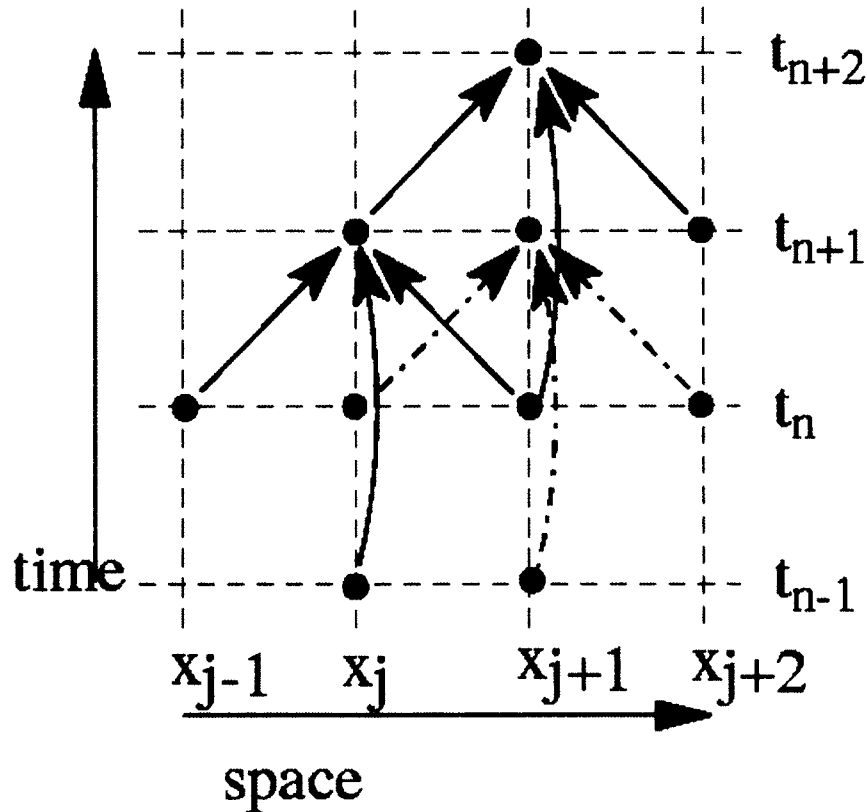


Figure A.1 1-D Leap Method, Time vs. Space

Figure A.1 displays the one-dimensional Dufort-Frankel integration scheme. Note that the code leaps through the two grid (red,blue), for each integration step. This is why the scheme is called Leapfrog.

The 3-D method employed in the model, while far more complicated, is of the same character. The fitting scheme also moves through the 3-D grid in a staggered manner, as in the above figure. Shown below is an example of the scheme for the 3-D convection equation:

$$f_{ijk}^{l+1} = \frac{1}{A_{ijk}} [(1 - A_{ijk}) f_{ijk}^l - 2\Delta t (\Delta x_i u_x^{ijk} (f_{i+1,j,k}^l - f_{i-1,j,k}^l))$$

$$\begin{aligned}
& +\Delta y_i u_y^{ijk} (f_{i,j+1,k}^l - f_{i,j-1,k}^l) + \Delta z_i u_z^{ijk} (f_{i,j,k+1}^l - f_{i,j,k-1}^l) \quad (\text{Equation A.2}) \\
& + 2\Delta t \eta \left( (f_{i-1,j,k}^l - f_{i+1,j,k}^l) / (\Delta x_i)^2 + (f_{i,j+1,k}^l - f_{i,j-1,k}^l) / (\Delta y_j)^2 + (f_{i,j,k+1}^l - f_{i,j,k-1}^l) / (\Delta z_k)^2 \right)
\end{aligned}$$

where:

$$A_{ijk} = 2\Delta t \eta \left( \frac{1}{(\Delta x_i)^2} + \frac{1}{(\Delta y_j)^2} + \frac{1}{(\Delta z_k)^2} \right) \quad (\text{Equation A.3})$$

The Leapfrog scheme is a second-order method, but leaves gaps (in the grid) for any given time step. Thus, the first-order-accurate Lax-Wendroff integration method is employed for the initial and final time steps and whenever a data output is desired. As an example, the 1-D case of the Lax-Wendroff integration method is given by:

$$T_i^{n+1} = T_i^n - 0.5C(T_{i+1}^n - T_{i-1}^n) + 0.5(T_{i-1}^n - 2T_i^n + T_{i+1}^n) \quad (\text{Equation A.4})$$

Note that superscripts denote the time index:  $n + 1$   $\equiv$  centered in present time +  $\Delta t$ ,  $n$   $\equiv$  present time, etc. The subscripts denote the spatial index:  $j + 1$   $\equiv$  centered in space +  $\Delta x$ ,  $n$   $\equiv$  centered in space, etc. (See Fig A.2.)

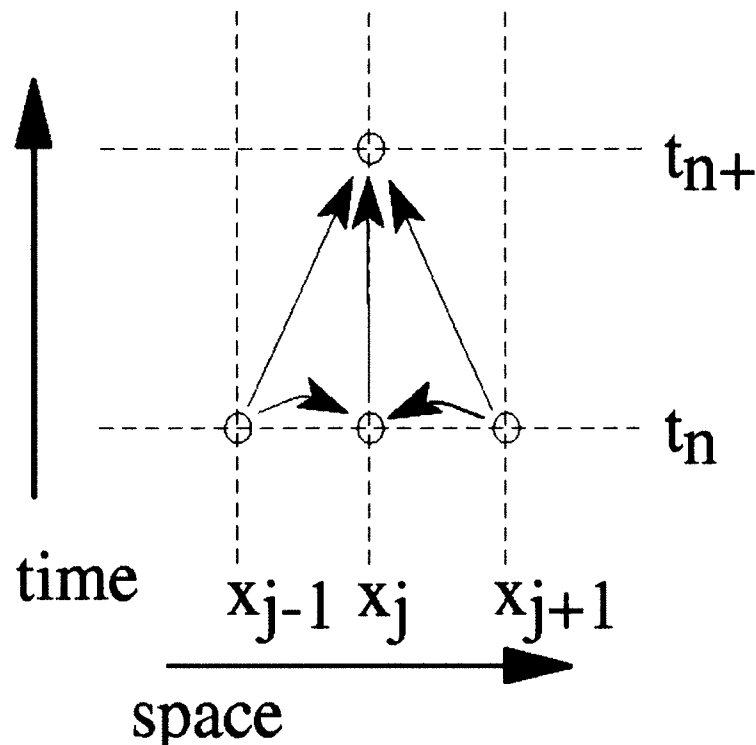


Figure A.2 1-D Lax-Wendroff Method—Time vs. Space

Figure A.2 displays the Lax-Wendroff integration scheme in 1-D. The Lax-Wendroff method fills in the gaps in the grid left by the Leapfrog method. To update to the next time step, it uses three points: One a time step back and centered in space, and two a time step back and offset from center by  $\pm\Delta x$ .

A note about discretization: If one is fortunate, a closed form solution to a partial differential equation exists. If one is even more fortunate, it can be determined. More frequently, however, a numerical solution must be applied.

The PDE (partial differential equation) is discretized into a system of algebraic equations. For consistency, when the transform that yielded the system of

algebraic equations from the original partial differential equations is done in reverse, one must again obtain the original set of PDE's. When applying the numerical solution, one must of course have numerical stability of the integration method. And finally, in the limit of  $\Delta x \Delta t \rightarrow 0$ , one must obtain (or at least approach) the exact solution. All the above conditions must be met for this to be a legitimate approach.

### **The Courant Conditions and Stability Considerations**

The Courant condition states that the time step  $dt$  (zeit) must be small enough that information traveling at the fastest speed, must not outrun the smallest spatial grid (e.g.)  $dx$ . If the information speed exceeds this velocity,  $\left(\frac{dx}{dt}\right)$ , numerical instability will result, and the code will crash.

### **Parallelization**

In order to investigate small-scale spatial and fast temporal scales with a three-dimensional, magnetosphere-ionosphere coupling code, computational resources far beyond what a personal computer or workstation could provide were required. Runs had to be made on the fastest (parallel, distributed memory) machines.

Please note that the equations of the model are explicit hyperbolic—resulting in a finite speed transport of information (i.e.waves). This enables one to use the finite element treatment. (Under certain circumstances, certain terms may dominate, becoming elliptic. This can be problematic for parallel simulations—imaginary characteristics, infinite information propagation speed. This is not considered to be a major problem in this simulation, though.)

Parallelization is the distribution of work (total simulation volume)—by the programmer—among multiple processors. The user explicitly determines which parts of the simulation domain are distributed “where” among the processors (domain decomposition).

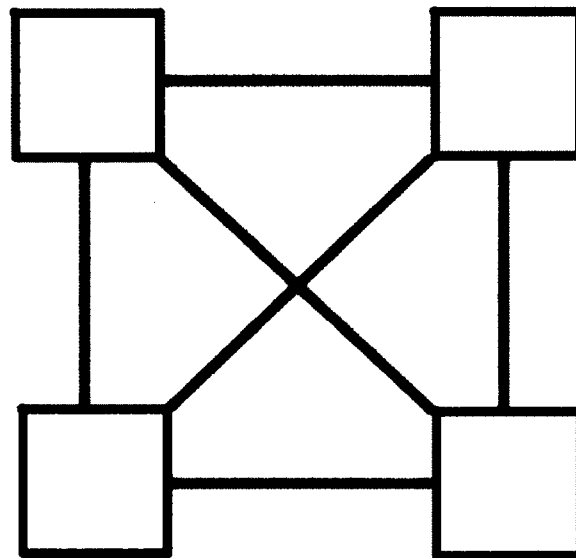


**Figure A.3 Parallelization Scheme. Assemblage of 4 Processors Shown.**

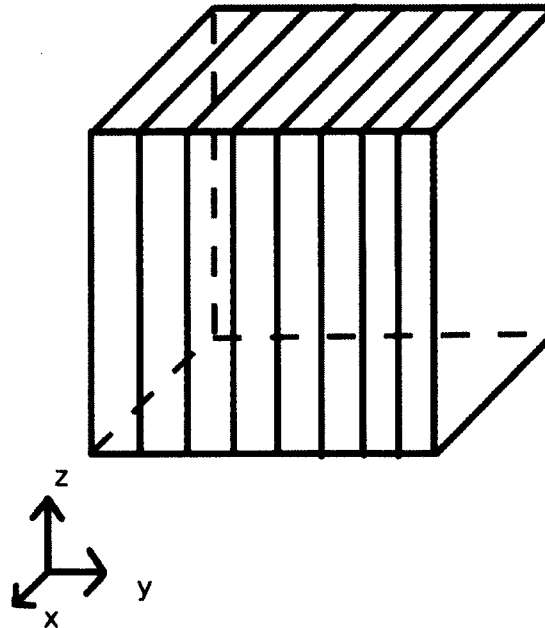


**Figure A.4 One-Dimensional Domain Decomposition**

Consider the speed-up that can be obtained:

$S$  = Speed of Individual Processor

$F$  = Efficiency of Parallelized Code. (This is a measure of the “Load Balance”—how evenly the work has been distributed among the processors. In the ideal case, this would be equal to 1. In any real-life situation,  $F < 1$ .)

$N_p$  = Number of Processors

$P$  = Proportion of Problem which Can Be Parallelized

$\tau_c$  = Inter-Processor Communication Time

Total Execution Time of Problem of Size N:

Scalar:

$$\tau_s = \frac{N}{S}$$

Parallel:

$$\tau_p = \frac{N}{S}(1 - P) + \frac{N}{FSN_p} + \tau_c$$

Speed-Up:

$$\frac{\tau_s}{\tau_p} = \left( 1 - P + \frac{P}{FN_p} + \frac{\tau_c S}{N} \right)^{-1}$$

Thus, for a code with a small portion which needs remain serial, one can reasonably expect for an explicitly parallelized code an approximately linear speed-up with increasing numbers of processors.

In an explicit parallelization, the user programs the work to be separated up among different processors; the determination of which processor receives which portion of the work is determined by the programmer. An example of a 2-D domain decomposition for this process is shown in Fig A.3.

Note that each processor has only its own portion of the work and has only local memory. Communication between the processors passes through the data connections after an integration cycle has been completed. (See Figure A.4.)

## Domain Decomposition

The above figure shows the 1-D domain decomposition used in the simulation. However, other potential domain decompositions could be employed. When choosing a domain decomposition scheme, it is desirable to maximize volume, and minimize surface area—as one wants to maximize the amount of work a processor is performing on its local domain, and minimize the amount of inter-processor communication it is required to do. However, serious consideration of the amount of coding required must be made. Consider, as an example, a 4-by-4-by-4 cube (general units). The work is to be distributed among 64 processors. It is assumed that: 1) the workload is evenly distributed throughout the volume of the simulation, and 2) the grid is not sliced too finely. (There are enough grid points per cell.) For the 1-D scheme, each processor would have a volume of 1; each interior processor would have a surface area of 32; the ratio of surface area to volume is 16; and the coding would only be moderately difficult. For the 2-D scheme, each processor would have a volume of 1; each interior processor would have a surface area of 4; the ratio of surface area to volume is 4; and the coding would be extremely difficult. For the 3-D scheme, each processor would have a volume of 1; each interior processor would have a surface area of 6; the ratio of surface area to volume would be 6; and the coding would be almost surrealistically difficult. For this model, a 1-D domain decomposition was chosen. (This proved to be adequate for our purposes.)



## Languages

For the explicit parallelization, there was a choice of languages that could be employed, namely, HPC (High performance FORTRAN), MPI (Message passing interface), and Co-Array FORTRAN. HPC is pretty much obsolete—and was thus never seriously considered. Co-Array [FORTRAN], while the easiest choice for coding, was not chosen, as it is (at present) only available on Cray platforms, and thus would be an extremely poor choice for “portability.” It was proposed that MPI be the parallel language used as it represented the closest thing to a standard in parallel computing, and thus would *optimize* portability. MPI is a distributed memory architecture.

### Parallel Distribution of the Grid

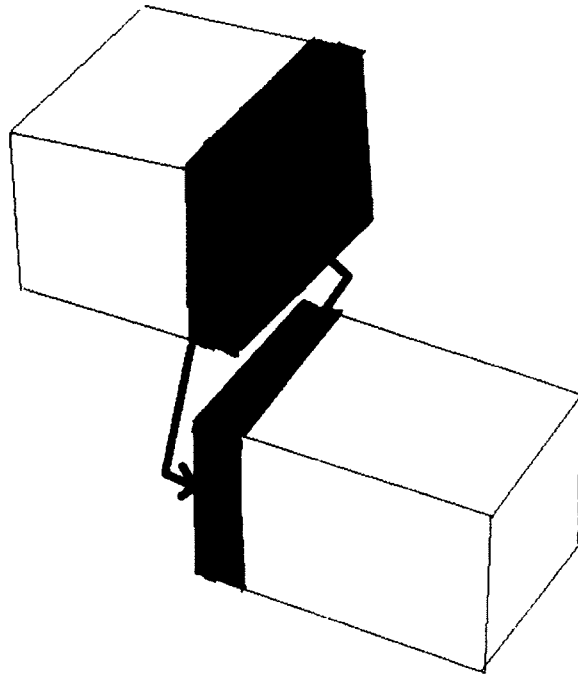
For the work distributed by the master to the slaves, each processor needed to know its portion of the grid (See Appendix C).

### Boundary Update

After each processor has finished its portion of the work, the overlapping boundaries for each processor are updated; this keeps the processors “on common ground” as far as computations are concerned. For the first version of this swapping, it was believed that explicitly handing each piece of data, one at a time, would be the most efficient. However, it was later determined [Personal conversation, Kate Hedstrom, of the Arctic Region Supercomputing Center], that this was extremely inefficient as each swap required that three steps be performed: The data had to be

prepared to be sent, it had to be sent, and the data had to be received by another processor. For the second incarnation of this swap routine, the entire data set was buffered, and then sent (See Appendix D). This greatly improved efficiency. The mathematical bounds (that is, the boundaries needed for adjacent points by the integration routines, but not part of the simulation domain) on the first and last processor (boundaries not shared with another processor) must then be updated.

Since the 1-D domain decomposition scheme was the one chosen, two overlapping two-dimensional “planes” had to be swapped:



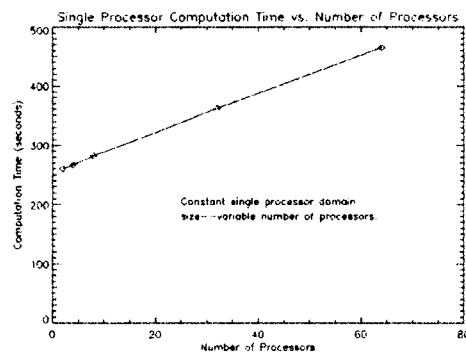
**Figure A.5 Boundary Update Scheme**

Figure A.5 shows how two-dimensional planes are updated during a boundary swap.

Worth noting, is that—since all the equations used in the model were explicitly hyperbolic (Meaning they had only local physics with no changes occurring instantaneously at high speed across the entire simulation domain)—the model lent itself quite well to explicit parallelization. Also worth noting, is that the discretization of the PDE (mentioned above—“Integration Methods”) for hyperbolic equations, leads to characteristic equations which only require “next-neighbor” information, thus lending nicely to parallelization.

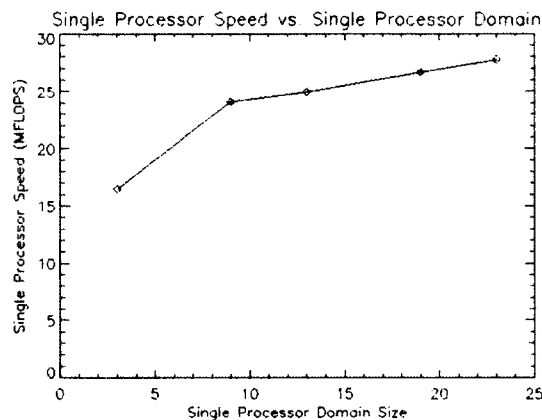
### Performance Testing

Extensive validation and performance testing of the explicit parallelization model was performed. The parallelized version of the code performed superbly well (see below), and the parallelization was extremely efficient (see below). The results of the code were also validated.



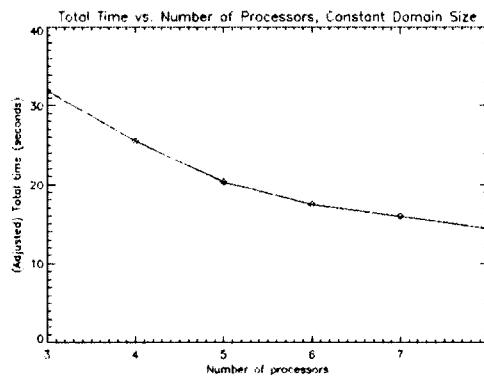
**Figure A.6 Single Processor Computation Times for Constant Domain Size (7), and Varying Number of Processors**

Figure A.6 shows an undesirable—but acceptable—increase in computation time with an increasing number of processors. In an ideal case, this line would have zero slope, showing no increase in overhead of inter-processor communication with an increase in the number of processors.



**Figure A.7 Single Processor Computation Times for Fixed Number of Processors (3), and Varying Domain Size**

Figure A.7 shows and increase in single processor speed (MFLOPS), for an increase in single processor domain size. This reflects the fact that the processor is progressively spending more time on its own portion of the work, and less time on inter-processor communication.



**Figure A.8 Total Time for Fixed "Large" Domain Size, and Varying Number of Processors**

Figure A.8 shows a decrease in total computation time (seconds). This is due to the fact that as more processors are added, each one has less total work to perform. Note the flattening of the slope of the curve with increasing number of processors: This reflects the fact that there is an intrinsically serial portion of the code, and, theoretically, if the number of processors were to approach infinity, the total computation time would approach the serial computation time.

### **VAMPIR**

There exists an exceptional profiling/debugging tool for MPI codes named VAMPIR. (Note “MPI” in the name.) VAMPIR shows, among other things, what each processor is doing in a timeline.

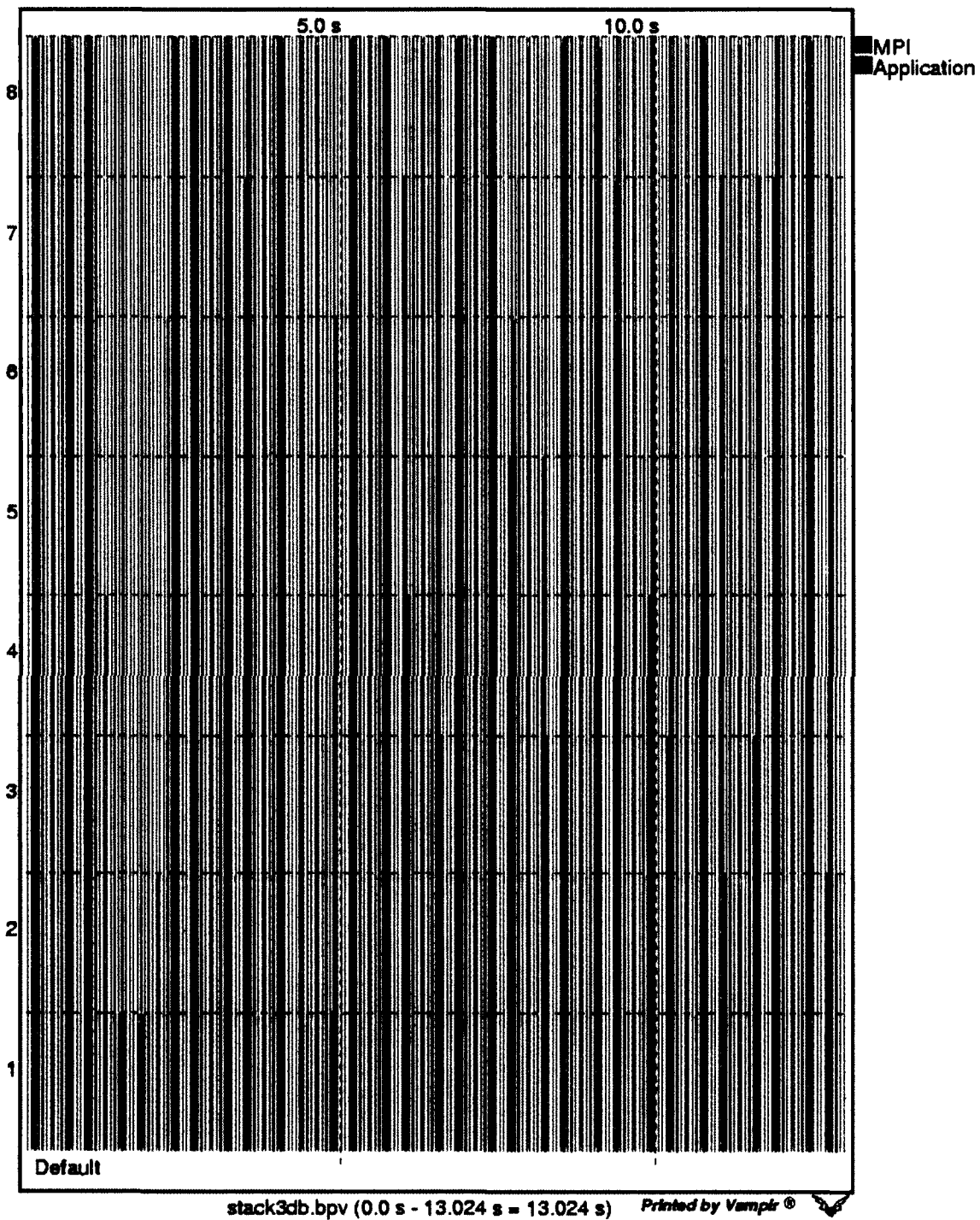


Figure A.9VAMPIR Timeline Plot, Number of Processors vs. Time (seconds)

Figure A.9 shows for each processor when it is active (green) and idle (red). Red means either that a processor is waiting on an MPI call, or for another processor to finish with information it requires. Except for the red bar showing the initial start-up (the master processor determining the work to distribute to the slaves), this plot is almost all green. This demonstrates that this is a well-parallelized code.

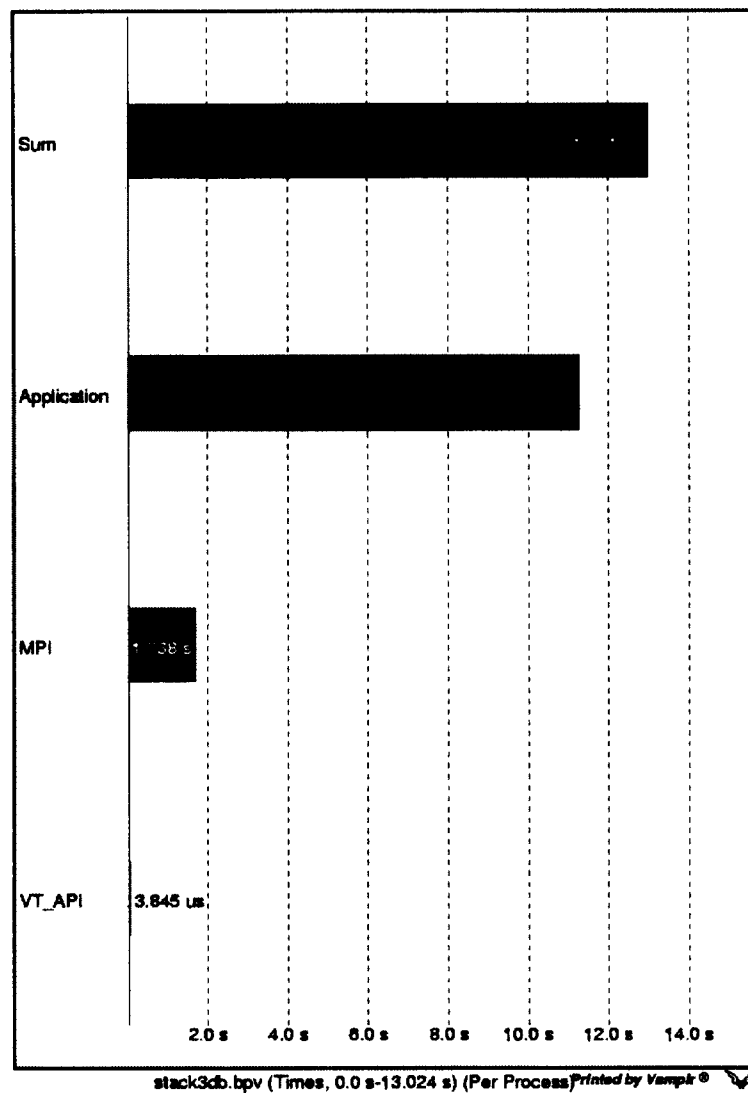


Figure A.10 VAMPIR Summary Chart

The above figure shows that the vast majority of processor time is spent on computation—again displaying excellent parallelization. It is worth noting that this code also vectorized more efficiently than 94% of the codes run on ARSC (Arctic Region Supercomputing Center) machines, when audited in 2002. This is comparing with codes written by professional programmers.

Earlier runs were done on “Yukon,” a Cray T3-E, compiled in the Cray Compiler Environment. Later runs were run on “Iceberg,” an IBM cluster, compiled with the IBM MPI XLF Fortran Compiler.



## Appendix B — Calculation of the Amount of Joule Heating for Various Scale Sizes

Shown below are the (truncated) code segments for the calculation of the amount of Joule heating for various scale sizes. The language used is FORTRAN.

```

subroutine diag1
c*****
c bestimmung von masse und energien des plasmas -And the joule
c heating stuff :)
c*****
implicit none
include 'mpif.h'

```

Inclusion of MPI library. This must be done in each subroutine which uses any MPI variable. (It is a good idea to include it unconditionally.)

```
include 'elin'
```

Inclusion of library with common variables to “clone” the operation of “global variables.”

Routine to calculate the amount of Joule heating occurring, for various scale sizes—  
for any generalized parallelization.

```

* .....
* the joule heating stuff
* .....
*
*

* Set height:
* determined from "epar"--z~2 or 3 (km)
  iz = 15
* addition of calculation of Joule heating at numerical resolution
* 11/4/04 Thursday
  fine = 0.
  do 990 i = 2,nx-1
    do 990 j = 2,ny-2
      iv = i+(j-1)*nx
      del(iv) = 0.25/(difx(iv)*dify(iv))
      fine = fine
      *      + ((sx(iv,iz)**2 + sy(iv,iz)**2 + sz(iv,iz)**2)
      *      /(rho(iv,iz)**2))*del(iv)
990 continue
  call MPI_BARRIER(MPI_COMM_WORLD,ierr)

```

```

call MPI_GATHER(fine,1,MPI_REAL,sum,1,MPI_REAL,
* 0,MPI_COMM_WORLD,ierr)
if (procid .eq. 0) then
  joulefine = 0.
  do 995 i = 1,numpe
    joulefine = joulefine + sum(i)
995  continue
  end if

* write numerical resolution to file
  if (procid .eq. 0) then
    write(69,2002) zeit,97,97,joulefine
  end if

* Find the location of the physical boundaries.
  stepx = ((-xmin)+xmax)/float(jouleitx)
  do 1000 i=1,jitx-1
    xbound(i) = xmin + float(i-1)*stepx
1000 continue
  xbound(jitx) = xmax
  stepy = ((-ymin)+ymax)/float(jouleity)
  do 1010 i = 1,jity-1
    ybound(i) = ymin + float(i-1)*stepy
1010 continue
  ybound(jity) = ymax

```

\* Find the "span" of all but boundary grid points

```
do 1020 i = 2,nx-1
```

```
  delxleft(i) = (x(i)-x(i-1))/2.
```

```
  delxright(i) = (x(i+1)-x(i))/2.
```

\* just interesting---xminus is never used. . . .

```
  xminus(i) = (x(i)+x(i-1))/2.
```

```
  xplus(i) = (x(i+1)+x(i))/2.
```

```
  delxspan(i) = delxright(i) + delxleft(i)
```

```
1020 continue
```

\* Note: This only works as the grid is orthogonal (irregular---but

\* still orthogonal)

```
do 1030 i = 2,ny-1
```

```
  j = 2+(i-1)*nx
```

```
  delydown(i) = (y(j)-y(j-nx))/2.
```

```
  delyup(i) = (y(j+nx)-y(j))/2.
```

```
  ylower(i) = (y(j)+y(j-nx))/2.
```

```
  yupper(i) = (y(j+nx)+y(j))/2.
```

```
  delyspan(i) = delyup(i) + delydown(i)
```

```
1030 continue
```

\* so boundlocas (boundary locations) not undefined. . . .

```
do 1040 i = 1, jitx
```

```
  boundlocax(i) = -1
```

```
1040 continue
```

```

do 1050 i = 1, jity
    boundlocay(i) = -1
1050 continue
* (this also serves as an "error condition")

* Determine number of [physical] boundaries on each processor (if any)
* This loop is b*****-all inefficient :(
    boundsx = 0
    do 1060 i = 1, jouleix
        do 1060 j = 2, nx-1
            if ((xbound(i) .gt. (x(j)-delxleft(j))) .and.
                * (xbound(i) .le. (x(j)+delxright(j)))) then
                    boundsx = boundsx + 1
* record boundary "location" (grid point)
                    boundlocax(boundsx) = j
* record "location" of xbound value
                    boundnumx(boundsx) = i
                end if
1060 continue

* Determine the number of boundaries in y identically for all
* processors. This loop is also b*****-all inefficient. :(
    boundsy = 0
    do 1070 i = 1, jouleity
        do 1070 j = 2, ny-1
            k = 2+((j-1)*nx)

```

```

        if ((ybound(i) .gt. (y(k)-delydown(j)))
*       .and. (ybound(i) .le. (y(k)+delyup(j))))
*       then
            boundsy = boundsy + 1
* record boundary "location" (grid point)
            boundlocay(boundsy) = j
* record "location" of ybound value
            boundnumy(boundsy) = i
        end if
1070 continue

* initialize "local" vxbin,bybin,vzbin, and areabin
* Note: This used to run from 1 to "bounds"---but it caused a floating
* point exception, if "bounds" was equal to zero. . . .
    do 1080 i = 1,jitx
        do 1080 j = 1,jity
            vxbin(i,j) = 0.
            vybin(i,j) = 0.
            vzbin(i,j) = 0.
            areabin(i,j) = 0.
        do 1080 continue

* This is now done above---11/4/04 Thursday
* Interim calculation of 1/(4*difx*dify)---to avoid future division
* note that this must be done in a separate loop---otherwise

```

```
* del(iv+1) not defined in next loop computation
*   do 1090 i = 1,ny
*     do 1090 j = 1,nx
*       iv = j + (i-1)*nx
*       del(iv) = 0.25/(difx(iv)*dify(iv))
* 1090 continue

* ATTENTION!! WARNING!! This next bit is for DEBUGGING ONLY!!!!
* DO NOT use for any other purpose WHATSOEVER!!!!
*   do 1069 j = 1,ny
*     do 1069 i = 1,nx
*       iv = i + (j-1)*nx
*       sx(iv,iz) = 4.
*       sy(iv,iz) = 4.
*       sz(iv,iz) = 4.
*       rho(iv,iz) = 1.
* 1069 continue

* calculation of "local" vxbin,bybin,vzbin, and areabin
* This is the "meat and potatoes" of the code. This is where all the
* values for the x-velocity, the y-velocity, the z-velocity, and the
* area of the region in question are computed and put into "bins." The
* way this works is as follows:
*
* For each y-value:
```

- \* -determine if there is a y-boundary for that grid point; if yes,
- \* -add the lower part of that value to the "bin."
- \* -check to see if there is a multiple boundary for the grid
- \* point; if yes,
- \* -add that value to the next bin, then check for an
- \* addition multiple boundary; if yes,
- \* -go to "deal with multiple boundary"
- \* -repeat check
- \* -when all boundaries have been dealt with on that grid point,
- \* add the final bit to that bin
- \* -if it has been determined that there is are no boundaries
- \* on a grid point, add the entire amount to this "unencumbered
- \* cell"
- \* Also, for each y-value, perform for EACH x-value
- \* -add to total value for each grid point to the "bin"
- \* -then check for a boundary on that grid point; if yes,
- \* -subtract the amount necessary to the present bin, then move
- \* to the "next 'bin'"
- \* -check for multiple boundaries; if yes, deal with as above---
- \* making successive checks for subsequent multiple boundaries
- \* on a grid point
- \* -finally, after all boundaries have been accounted for,
- \* "close the cell"
- \* Please note that the x-values are dealt with slightly differently
- \* than the y-values. (First adding the total value to "y"--and then



\* subtracting if necessary--wasn't practical

boundvaly = 1

do 1100 j = 2,ny-1

boundvalx = 1

if (boundlocay(boundvaly) .eq. j) then

\* deal with the first "y boundary"

do 1110 i = 2,nx-1

iv = i + (j-1)\*nx

tempvelx = (sx(iv,iz)/rho(iv,iz))\*del(iv)

tempvely = (sy(iv,iz)/rho(iv,iz))\*del(iv)

tempvelz = (sz(iv,iz)/rho(iv,iz))\*del(iv)

temparea = del(iv)

yvalue = (ybound(boundnumy(boundvaly))

\* - ylower(j))/delyspan(j)

vxbin(boundvalx,boundvaly) = vxbin(boundvalx,boundvaly)

\* + yvalue

\* \* tempvelx

vybin(boundvalx,boundvaly) = vybin(boundvalx,boundvaly)

\* + yvalue

\* \* tempvely

vzbin(boundvalx,boundvaly) = vzbin(boundvalx,boundvaly)

\* + yvalue

\* \* tempvelz

areabin(boundvalx,boundvaly) =

\* areabin(boundvalx,boundvaly)

```

*           + yvalue
*           * temparea
if (boundlocax(boundvalx) .eq. i) then
  xvalue = (xplus(i)
*         - xbound(boundnumx(boundvalx)))
*         / delxspan(i)
  vxbin(boundvalx,boundvaly) =
*         vxbin(boundvalx,boundvaly)
*         - xvalue
*         * yvalue
*         * tempvelx
  vybin(boundvalx,boundvaly) =
*         vybin(boundvalx,boundvaly)
*         - xvalue
*         * yvalue
*         * tempvely
  vzbin(boundvalx,boundvaly) =
*         vzbin(boundvalx,boundvaly)
*         - xvalue
*         * yvalue
*         * tempvelz
  areabin(boundvalx,boundvaly) =
*         areabin(boundvalx,boundvaly)
*         - xvalue
*         * yvalue

```

```

*           * temparea
boundvalx = boundvalx + 1
if (boundlocax(boundvalx-1) .eq.
*   boundlocax(boundvalx)) then
1120   xvalue = (xbound(boundnumx(boundvalx))
*         - xbound(boundnumx(boundvalx-1)))
*         / delxspan(i)
vxbin(boundvalx,boundvaly) =
*   vxbin(boundvalx,boundvaly)
*   + xvalue
*   * yvalue
*   * tempvelx
vybin(boundvalx,boundvaly) =
*   vybin(boundvalx,boundvaly)
*   + xvalue
*   * yvalue
*   * tempvely
vzbin(boundvalx,boundvaly) =
*   vzbin(boundvalx,boundvaly)
*   + xvalue
*   * yvalue
*   * tempvelz
areabin(boundvalx,boundvaly) =
*   areabin(boundvalx,boundvaly)
*   + xvalue

```

```

*           * yvalue
*           * temparea
          boundvalx = boundvalx + 1
          if (boundlocax(boundvalx-1) .eq.
*           boundlocax(boundvalx)) goto 1120
          end if
          xvalue = (xplus(i)
*           - xbound(boundnumx(boundvalx-1)))
*           / delxspan(i)
          vxbin(boundvalx,boundvaly) =
*           vxbin(boundvalx,boundvaly)
*           + xvalue
*           * yvalue
*           * tempvelx
          vybin(boundvalx,boundvaly) =
*           vybin(boundvalx,boundvaly)
*           + xvalue
*           * yvalue
*           * tempvely
          vzbin(boundvalx,boundvaly) =
*           vzbin(boundvalx,boundvaly)
*           + xvalue
*           * yvalue
*           * tempvelz
          areabin(boundvalx,boundvaly) =

```

```

*          areabin(boundvalx,boundvaly)
*          + xvalue
*          * yvalue
*          * temparea
      end if
1110  continue
      boundvaly = boundvaly + 1
* check for "double boundary"
      if (boundlocay(boundvaly-1) .eq. boundlocay(boundvaly))
*   then
* deal with "double boundary"
1150  do 1130 i = 2,nx-1
      iv = i + (j-1)*nx
      tempvelx = (sx(iv,iz)/rho(iv,iz))*del(iv)
      tempvely = (sy(iv,iz)/rho(iv,iz))*del(iv)
      tempvelz = (sz(iv,iz)/rho(iv,iz))*del(iv)
      temparea = del(iv)
      yvalue = (ybound(boundnumy(boundvaly))
*           - ybound(boundnumy(boundvaly-1)))
*           / delyspan(j)
      vxbin(boundvalx,boundvaly) =
*           vxbin(boundvalx,boundvaly)
*           + yvalue
*           * tempvelx
      vybin(boundvalx,boundvaly) =

```

```

*          vybin(boundvalx,boundvaly)
*          + yvalue
*          * tempvely

vzbin(boundvalx,boundvaly) =
*          vzbin(boundvalx,boundvaly)
*          + yvalue
*          * tempvelz

areabin(boundvalx,boundvaly) =
*          areabin(boundvalx,boundvaly)
*          + yvalue
*          * temparea

if (boundlocax(boundvalx) .eq. i) then
  xvalue = (xplus(i)
*          - xbound(boundnumx(boundvalx)))
*          / delxspan(i)

vxbin(boundvalx,boundvaly) =
*          vxbin(boundvalx,boundvaly)
*          - xvalue
*          * yvalue
*          * tempvelx

vybin(boundvalx,boundvaly) =
*          vybin(boundvalx,boundvaly)
*          - xvalue
*          * yvalue
*          * tempvely

```

```

vzbin(boundvalx,boundvaly) =
*       vzbin(boundvalx,boundvaly)
*       - xvalue
*       * yvalue
*       * tempvelz
areabin(boundvalx,boundvaly) =
*       areabin(boundvalx,boundvaly)
*       - xvalue
*       * yvalue
*       * temparea
boundvalx = boundvalx + 1
if (boundlocax(boundvalx-1) .eq.
*     boundlocax(boundvalx)) then
1140     xvalue = (xbound(boundnumx(boundvalx))
*           - xbound(boundnumx(boundvalx-1)))
*           / delxspan(i)
vxbin(boundvalx,boundvaly) =
*       vxbin(boundvalx,boundvaly)
*       + xvalue
*       * yvalue
*       * tempvelx
vybin(boundvalx,boundvaly) =
*       vybin(boundvalx,boundvaly)
*       + xvalue
*       * yvalue

```

```

*           * tempvely
          vzbin(boundvalx,boundvaly) =
*           vzbin(boundvalx,boundvaly)
*           + xvalue
*           * yvalue
*           * tempvelz
          areabin(boundvalx,boundvaly) =
*           areabin(boundvalx,boundvaly)
*           + xvalue
*           * yvalue
*           * temparea
          boundvalx = boundvalx + 1
          if (boundlocax(boundvalx-1) .eq.
*           boundlocax(boundvalx)) goto 1140
          end if
          xvalue = (xplus(i)
*           - xbound(boundnumx(boundvalx-1)))
*           / delxspan(i)
          vxbin(boundvalx,boundvaly) =
*           vxbin(boundvalx,boundvaly)
*           + xvalue
*           * yvalue
*           * tempvelx
          vybin(boundvalx,boundvaly) =
*           vybin(boundvalx,boundvaly)

```



```

*          + xvalue
*          * yvalue
*          * tempvely
          vzbin(boundvalx,boundvaly) =
*          vzbin(boundvalx,boundvaly)
*          + xvalue
*          * yvalue
*          * tempvelz
          areabin(boundvalx,boundvaly) =
*          areabin(boundvalx,boundvaly)
*          + xvalue
*          * yvalue
*          * temparea
          end if
1130      continue
* check if additional "double boundary" if yes, go to "deal with 'double
* boundary" :)
          boundvaly = boundvaly + 1
          if (boundlocay(boundvaly-1) .eq.
*          boundlocay(boundvaly)) goto 1150
          end if
* close cell (deal with "end portion of 'y cell")
          do 1160 i = 2,nx-1
              iv = i + (j-1)*nx
              tempvelx = (sx(iv,iz)/rho(iv,iz))*del(iv)

```

```

tempvely = (sy(iv,iz)/rho(iv,iz))*del(iv)
tempvelz = (sz(iv,iz)/rho(iv,iz))*del(iv)
temparea = del(iv)
yvalue = (yupper(j)
*       - ybound(boundnumy(boundvaly-1)))
*       / delyspan(j)
vxbin(boundvalx,boundvaly)
*       = vxbin(boundvalx,boundvaly)
*       + yvalue
*       * tempvelx
vybin(boundvalx,boundvaly)
*       = vybin(boundvalx,boundvaly)
*       + yvalue
*       * tempvely
vzbin(boundvalx,boundvaly)
*       = vzbin(boundvalx,boundvaly)
*       + yvalue
*       * tempvelz
areabin(boundvalx,boundvaly) =
*       areabin(boundvalx,boundvaly)
*       + yvalue
*       * temparea
if (boundlocax(boundvalx) .eq. i) then
  xvalue = (xplus(i)
*         - xbound(boundnumx(boundvalx)))

```

```

*           / delxspan(i)
vxbin(boundvalx,boundvaly) =
*           vxbin(boundvalx,boundvaly)
*           - xvalue
*           * yvalue
*           * tempvelx
vybin(boundvalx,boundvaly) =
*           vybin(boundvalx,boundvaly)
*           - xvalue
*           * yvalue
*           * tempvely
vzbin(boundvalx,boundvaly) =
*           vzbin(boundvalx,boundvaly)
*           - xvalue
*           * yvalue
*           * tempvelz
areabin(boundvalx,boundvaly) =
*           areabin(boundvalx,boundvaly)
*           - xvalue
*           * yvalue
*           * temparea
boundvalx = boundvalx + 1
if (boundlocax(boundvalx-1) .eq.
*   boundlocax(boundvalx)) then
1170     xvalue = (xbound(boundnumx(boundvalx))

```

```

*      - xbound(boundnumx(boundvalx-1)))
*      / delxspan(i)
vxbin(boundvalx,boundvaly) =
*      vxbin(boundvalx,boundvaly)
*      + xvalue
*      * yvalue
*      * tempvelx
vybin(boundvalx,boundvaly) =
*      vybin(boundvalx,boundvaly)
*      + xvalue
*      * yvalue
*      * tempvely
vzbin(boundvalx,boundvaly) =
*      vzbin(boundvalx,boundvaly)
*      + xvalue
*      * yvalue
*      * tempvelz
areabin(boundvalx,boundvaly) =
*      areabin(boundvalx,boundvaly)
*      + xvalue
*      * yvalue
*      * temparea
boundvalx = boundvalx + 1
if (boundlocax(boundvalx-1) .eq.
*      boundlocax(boundvalx)) goto 1170

```

```
end if
xvalue = (xplus(i)
*      - xbound(boundnumx(boundvalx-1)))
*      / delxspan(i)
vxbin(boundvalx,boundvaly) =
*      vxbin(boundvalx,boundvaly)
*      + xvalue
*      * yvalue
*      * tempvelx
vybin(boundvalx,boundvaly) =
*      vybin(boundvalx,boundvaly)
*      + xvalue
*      * yvalue
*      * tempvely
vzbin(boundvalx,boundvaly) =
*      vzbin(boundvalx,boundvaly)
*      + xvalue
*      * yvalue
*      * tempvelz
areabin(boundvalx,boundvaly) =
*      areabin(boundvalx,boundvaly)
*      + xvalue
*      * yvalue
*      * temparea
end if
```

```

1160  continue
      else
* unencumbered "y cell"
      do 1180 i = 2,nx-1
          iv = i + (j-1)*nx
          tempvelx = (sx(iv,iz)/rho(iv,iz))*del(iv)
          tempvely = (sy(iv,iz)/rho(iv,iz))*del(iv)
          tempvelz = (sz(iv,iz)/rho(iv,iz))*del(iv)
          temparea = del(iv)
          vxbin(boundvalx,boundvaly) = vxbin(boundvalx,boundvaly)
*              + tempvelx
          vybin(boundvalx,boundvaly) = vybin(boundvalx,boundvaly)
*              + tempvely
          vzbin(boundvalx,boundvaly) = vzbin(boundvalx,boundvaly)
*              + tempvelz
          areabin(boundvalx,boundvaly) =
*              areabin(boundvalx,boundvaly)
*              + temparea
          if (boundlocax(boundvalx) .eq. i) then
              xvalue = (xplus(i)
*                  - xbound(boundnumx(boundvalx)))
*                  / delxspan(i)
              vxbin(boundvalx,boundvaly) =
*                  vxbin(boundvalx,boundvaly)
*                  - xvalue

```

```

*           * tempvelx
vybin(boundvalx,boundvaly) =
*           vybin(boundvalx,boundvaly)
*           - xvalue
*           * tempvely
vzbin(boundvalx,boundvaly) =
*           vzbin(boundvalx,boundvaly)
*           - xvalue
*           * tempvelz
areabin(boundvalx,boundvaly) =
*           areabin(boundvalx,boundvaly)
*           - xvalue
*           * temparea
boundvalx = boundvalx + 1
if (boundlocax(boundvalx-1) .eq.
*   boundlocax(boundvalx)) then
1190   xvalue = (xbound(boundnumx(boundvalx))
*           - xbound(boundnumx(boundvalx-1)))
*           / delxspan(i)
vxbin(boundvalx,boundvaly) =
*           vxbin(boundvalx,boundvaly)
*           + xvalue
*           * tempvelx
vybin(boundvalx,boundvaly) =
*           vybin(boundvalx,boundvaly)

```

```

*          + xvalue
*          * tempvely
      vzbin(boundvalx,boundvaly) =
*          vzbin(boundvalx,boundvaly)
*          + xvalue
*          * tempvelz
      areabin(boundvalx,boundvaly) =
*          areabin(boundvalx,boundvaly)
*          + xvalue
*          * temparea
      boundvalx = boundvalx + 1
      if (boundlocax(boundvalx-1) .eq.
*      boundlocax(boundvalx)) goto 1190
      end if
      xvalue = (xplus(i)
*      - xbound(boundnumx(boundvalx-1)))
*      / delxspan(i)
      vxbin(boundvalx,boundvaly) =
*      vxbin(boundvalx,boundvaly)
*      + xvalue
*      * tempvelx
      vybin(boundvalx,boundvaly) =
*      vybin(boundvalx,boundvaly)
*      + xvalue
*      * tempvely

```



```

        vzbin(boundvalx,boundvaly) =
*           vzbin(boundvalx,boundvaly)
*           + xvalue
*           * tempvelz
        areabin(boundvalx,boundvaly) =
*           areabin(boundvalx,boundvaly)
*           + xvalue
*           * temparea
    end if
1180  continue
    end if
1100 continue

* bringing it all together:
* note: this may not be the most efficient method (gathering (potentially)
* undefined array elements) ---but, MPI_Allgather, I believe, would cost
* me information that I need
    call MPI_BARRIER(MPI_COMM_WORLD,ierr)
    call MPI_GATHER(boundsx,1,MPI_INTEGER,rootboundsx,1,
*           MPI_INTEGER,0,MPI_COMM_WORLD,ierr)
* find maximum bounds
    if (procid .eq. 0) then
        maximumx = rootboundsx(1)
        do 1200 i = 2,numpe
            if (rootboundsx(i) .gt. maximumx) maximumx

```

```

*           = rootboundsx(i)
1200 continue
    end if
    call MPI_BCAST(maximumx,1,MPI_REAL,0,MPI_COMM_WORLD,ierr)

* attention -- possibility to make this more efficient (MPI_GATHER
* of 2-D arrays. . . .)
* If you're still reading this, I owe you a beer.
* :) ;)

do 1210 i = 1,maximumx+1
    do 1210 j = 1,jity
        call MPI_GATHER(vxbin(i,j),1,MPI_REAL,vxtemp,1,
*           MPI_REAL,0,MPI_COMM_WORLD,ierr)
        call MPI_GATHER(vybin(i,j),1,MPI_REAL,vytemp,1,
*           MPI_REAL,0,MPI_COMM_WORLD,ierr)
        call MPI_GATHER(vzbin(i,j),1,MPI_REAL,vztemp,1,
*           MPI_REAL,0,MPI_COMM_WORLD,ierr)
        call MPI_GATHER(areabin(i,j),1,MPI_REAL,areatemp,1,
*           MPI_REAL,0,MPI_COMM_WORLD,ierr)
        if (procid .eq. 0) then
            do 1220 k = 1,numpe
                vxroot(i,j,k) = vxtemp(k)
                vyroot(i,j,k) = vytemp(k)
                vzroot(i,j,k) = vztemp(k)
            end do
        end if
    end do
end do

```

```
        arearoot(i,j,k) = areatemp(k)
1220        continue
        end if
1210 continue

if (procid .eq. 0) then
  do 1230 i = 1,jitx
    do 1230 j = 1,jity
      velx(i,j) = 0.
      vely(i,j) = 0.
      velz(i,j) = 0.
      area(i,j) = 0.
1230  continue
    endif
```

- \* A note to Antonius: I never "predefined" vxroot, etc. However, if the
- \* code ever hits any of the "undefined values," something is WRONG.
- \* Therefore, I left it as it is---sort of an automatic "error checking."

```
if (procid .eq. 0) then
  do 1240 m = 1,jity
    i = 1
    k = 1
1260  loopvar = rootboundsx(k)
      tempx = rootboundsx(k)
```

```

do 1250 l = 1, loopvar + 1
  if (tempx .gt. 0) then
    velx(i,m) = velx(i,m) + vxroot(l,m,k)
    vely(i,m) = vely(i,m) + vyroot(l,m,k)
    velz(i,m) = velz(i,m) + vzroot(l,m,k)
    area(i,m) = area(i,m) + arearoot(l,m,k)
    i = i + 1
    tempx = tempx - 1
  else
    velx(i,m) = velx(i,m) + vxroot(l,m,k)
    vely(i,m) = vely(i,m) + vyroot(l,m,k)
    velz(i,m) = velz(i,m) + vzroot(l,m,k)
    area(i,m) = area(i,m) + arearoot(l,m,k)
  end if
1250 continue
  k = k + 1
  if (k .le. numpe) goto 1260
1240 continue
end if

```

\* \*FINALLY! have average velocities

```

if (procid .eq. 0) then
  jouleave = 0.

```

\* The following assumes that no one would ever want to "chop" the

\* total domain more than 10 times. If you don't like this--go

```

* ahead and crank it up to 100---or a million; it won't make any
* difference....
    do 1270 k = 1,10
* termination condition of diag1--_limited_ error checking....
* Not very "elegant," but... if one does "return" then processor 0
* avoids the MPI_BARRIER at the end of this routine, and carries on its
* merry way to other diagnostics---ultimately gridlocking the code :P
* attention change
*   if (((k-1)*xiter .gt. jitx) .or. ((k-1)*yiter .gt.
* *   jity)) goto 2069
*   if ((xiter**(k-1) .gt. jitx) .or.
* *   (yiter**(k-1) .gt. jity)) goto 2069
* attention change
*   if (k .gt. 1) then
*       if ((mod(jitx,(k-1)*xiter) .ne. 0) .or. (mod(jity,
* *       (k-1)*yiter) .ne. 0)) then
*           if ((mod(jitx,xiter**(k-1)) .ne. 0) .or. (mod(jity,
* *           yiter**(k-1)) .ne. 0)) then
*               write(69,2003)
* debug attention ATTENTION change
*   if (k .le. 2) then
        checkx = xiter**(k-1)
        checky = yiter**(k-1)
        if ((checkx .gt. jitx) .or.
*       (checky .gt. jity)) goto 2069

```

```

    if ((mod(jitx,checkx) .ne. 0) .or.
*   (mod(jity,checky) .ne. 0)) then
        write(69,2003)
        goto 2069
    end if
*   else
*       checkx = checkx**2
*       checky = checky**2
*       if ((checkx .gt. jitx) .or.
* *   (checky .gt. jity)) goto 2069
*       if ((mod(jitx,checkx) .ne. 0) .or.
* *   (mod(jity,checky) .ne. 0)) then
*           write(69,2003)
*           goto 2069
*       end if
*   endif
*   Not very "elegant," but ... if one does "return" then processor 0
*   avoids the MPI_BARRIER at the end of this routine, and carries on its
*   merry way to other diagnostics---ultimately gridlocking the code :P
*       goto 2069
*   end if
*   end if
do 1280 j=1,jity
    do 1280 i = 1,jitx
        velxsum(i,j) = 0.

```

```

        velysum(i,j) = 0.
        velzsum(i,j) = 0.
        areasum(i,j) = 0.
1280    continue
* debug ATTENTION attention -- change
*    if (k .gt. 1) then
*        xwidth = jitx/((k-1)*xiter)
*        ywidth = jity/((k-1)*yiter)
*    else
*        xwidth = 1
*        ywidth = 1
*    endif
*        xwidth = jitx/(jitx/(xiter**(k-1)))
*        ywidth = jity/(jity/(yiter**(k-1)))
*    if (k .le. 2) then
*        xwidth = jitx/(jitx/(xiter**(k-1)))
*        ywidth = jity/(jity/(yiter**(k-1)))
*    else
*        xwidth = xwidth**2
*        ywidth = ywidth**2
*    endif
* REUSE of boundvalx, boundvaly!
    boundvaly = 1
    do 1290 j = 1,jity
        boundvalx = 1

```

```

do 1300 i = 1,jitx
    velxsum(boundvalx,boundvaly) =
*       velxsum(boundvalx,boundvaly)
*       + velx(i,j)
    velysum(boundvalx,boundvaly) =
*       velysum(boundvalx,boundvaly)
*       + vely(i,j)
    velzsum(boundvalx,boundvaly) =
*       velzsum(boundvalx,boundvaly)
*       + velz(i,j)
    areasum(boundvalx,boundvaly) =
*       areasum(boundvalx,boundvaly)
*       + area(i,j)
    if (mod(i,xwidth) .eq. 0) boundvalx
*           = boundvalx + 1
1300    continue
    if (mod(j,ywidth) .eq. 0) boundvaly
*           = boundvaly + 1
1290    continue

* debug ATTENTION attention
    xloop = jitx/checkx
    yloop = jity/checky
* Let's try. . . .
*     xloop = jitx/(xiter**(k-1))

```



```

*   yloop = jity/(yiter**(k-1))
*   if (k.gt. 1) then
*       xloop = jitx/((k-1)*xiter)
*       yloop = jity/((k-1)*yiter)
*   else
*       xloop = jitx
*       yloop = jity
*   endif
jouleave = 0.
do 1310 j = 1,yloop
    do 1310 i = 1,xloop
        jouleave = jouleave + (velxsum(i,j)**2
*           + velysum(i,j)**2
*           + velzsum(i,j)**2)
*           / areasum(i,j)
1310    continue

* write to file
* debug attention change
*   if (k.gt. 1) then
*       write(69,2002) zeit,jitx/((k-1)*xiter),jity
* *           / ((k-1)*yiter),jouleave
*   else
*       write(69,2002) zeit,jitx,jity,jouleave
*   end if

```

```
        write(69,2002) zeit,jitx/checkx,jity/checky,jouleave
1270 continue
    end if
* debug -- test
*2069 beer = 'MILLER TIME!'
2069 i = 1
2002 format(1x,E15.4,1x,I7,1x,I7,1x,E15.4)
2003 format(1x,7H*ERROR*)
```

“Barrier call” seen by all processors—to make sure that they are all “in sync” before returning control to the main program. This call is almost certainly superfluous.

```
* More for my peace of mind than anything else:
    call MPI_BARRIER(MPI_COMM_WORLD,ierr)
    return
end
```

## Appendix C — Calculation and Distribution of Grid by “Master” to “Slaves”

Shown below are the (truncated) code segments for the calculation of the “big grid,” and the distribution of the necessary portions of the total grid to each processor—its “local grid.” The language used is FORTRAN.

```

subroutine grid
c*****
c  grid berechnet die gitterparameter, welche der integration
c  zugrunde liegen.
c  ( x senkrecht zur stromschicht - n koordinate
c  y ostrichtung      - -m koordinate
c  z nordrichtung    - l koordinate )
c*****
include 'mpif.h'

```

Inclusion of MPI library. This must be done in each subroutine which uses any MPI variable. (It is a good idea to include it unconditionally.)

```
include 'elin'
```

Inclusion of library with common variables—to “clone” the operation of “global variables.”

Determination of “big parameters”—the grid of the *entire* domain:

c symmetrie fuer zentrierte nichtaequidistantes gitter:

c.....

if (zentr(1)) then

do 260 ix = 1, ix0

bigx(ix) = ( bigx(ix)-bigx(bignx+1-ix) )/2.0

bdifx(ix) = ( bdifx(ix)+bdifx(bignx+1-ix) )/2.0

bddifpx(ix) = ( bddifpx(ix)+bddifmx(bignx+1-ix) )/2.0

bddifmx(ix) = ( bddifmx(ix)+bddifpx(bignx+1-ix) )/2.0

bddifx(ix) = ( bddifx(ix)+bddifx(bignx+1-ix) )/2.0

bmeanpx(ix) = ( bmeanpx(ix)+bmeanmx(bignx+1-ix) )/2.0

bmeanmx(ix) = ( bmeanmx(ix)+bmeanpx(bignx+1-ix) )/2.0

260 continue

bigx(ix0) = 0.0

bddifpx(ix0) = ( bddifpx(ix0)+bddifmx(ix0) )/2.0

bddifmx(ix0) = ( bddifpx(ix0)+bddifmx(ix0) )/2.0

bddifx(ix0) = ( bddifpx(ix0)+bddifmx(ix0) )/2.0

bmeanpx(ix0) = ( bmeanpx(ix0)+bmeanmx(ix0) )/2.0

bmeanmx(ix0) = ( bmeanpx(ix0)+bmeanmx(ix0) )/2.0

do 270 ix = ix0+1, bignx

bigx(ix) = -bigx(bignx+1-ix)

bdifx(ix) = bdifx(bignx+1-ix)

```

bddifpx(ix) = bddifmx(bignx+1-ix)
bddifmx(ix) = bddifpx(bignx+1-ix)
bddifx(ix) = bddifx(bignx+1-ix)
bmeanpx(ix) = bmeanmx(bignx+1-ix)
bmeanmx(ix) = bmeanpx(bignx+1-ix)

```

```
270 continue
```

```
end if
```

```
do 300 ix = 1, bignx
```

```
    x(ix) = xanf + x(ix)
```

```
300 continue
```

```
c
```

```
c belegung der randwerte der gitterparameter:
```

```
c.....
```

```
bigx(1)    = 2.*xmin - bigx(3)
```

```
bigx(bignx) = 2.*xmax -bigx(bignx-2)
```

```
bigx(2)    = xmin
```

```
bigx(bignx-1) = xmax
```

```
bdifx(1)    = bdifx(3)
```

```
bdifx(bignx) = bdifx(bignx-2)
```

```
bddifmx(2)  = ( bddifpx(2) + bddifmx(2) ) / 2.0
```

```
bddifmx(bignx-1)= ( bddifpx(bignx-1) + bddifmx(bignx-1) ) / 2.0
```

```
bddifpx(2)  = bddifmx(2)
```

```
bddifpx(bignx-1)= bddifmx(bignx-1)
```

```
bddifmx(1)  = bddifpx(3)
```

```

bddifpx(1)  = bddifmx(3)
bddifmx(bignx) = bddifpx(bignx-2)
bddifpx(bignx) = bddifmx(bignx-2)
bmeanmx(1)  = bmeanpx(3)
bmeanpx(1)  = bmeanmx(3)
bmeanmx(bignx) = bmeanpx(bignx-2)
bmeanpx(bignx) = bmeanmx(bignx-2)

```

Distribution of the “local grid” to each “slave.” Please note that this employs both the variable “numpe” (number of processors) and “procid” (the unique numerical id of each processor in the simulation).

c

c attention

```

do 320 i=0,numpe-1
  if (procid .eq. i) then
    do 325 ix=1,nx
      x(ix)  = bigx(ix+(nx-2)*i)
      difx(ix) = bdifx(ix+(nx-2)*i)
      ddifx(ix) = bddifx(ix+(nx-2)*i)
      ddifpx(ix) = bddifpx(ix+(nx-2)*i)
      ddifmx(ix) = bddifmx(ix+(nx-2)*i)
      meanpx(ix) = bmeanpx(ix+(nx-2)*i)
      meanmx(ix) = bmeanmx(ix+(nx-2)*i)
    enddo
  endif
enddo

```

```
325  continue
      endif
320  continue
```

**Note:**

“Numpe” = Number of processors

“Procid” = Unique numerical ID tag for each processor

So, the above loop runs in parallel on all the processors. As each ID tag is reached in the loop, it then distributes the correct local grid to each processor.

## Appendix D — Swap Routine to Update Boundary Grid Points

Shown below is a (truncated) boundary update routine. This is tied with the shortest of such routines. It is in the language of FORTRAN.

```

subroutine randr
c*****
c  berechnung der randwerte fuer rho,rhon analog randwe
c*****
      implicit none
      include 'mpif.h'

```

Inclusion of MPI library. This must be done in each subroutine which uses any MPI variable. (It is a good idea to include it unconditionally.)

```

      include 'elin'

```

Inclusion of library with common variables—to “clone” the operation of “global variables.”

Local “swap arrays” that allow for a large increase in efficiency of the boundary updates:



- \* The following arrays are "local," and burn a fair amount of memory;
- \* however, they allow one to send messages as `_one_array_--` and thus
- \* allow for SPEED. :)

```
real pumpuprho(ny,nz), pumpdnrho(ny,nz), pumpuprho(ny,nz),
```

```
* pumpdnrho(ny,nz), pumpuprho(ny,nz), pumpdnrho(ny,nz),
```

```
* pumpuprho(ny,nz), pumpdnrho(ny,nz)
```

Boundary update:

- \* Update the periodic boundary y-z planes:

- \* Make certain boundaries are in sync:

```
call MPI_BARRIER(MPI_COMM_WORLD,ierr)
```

- \* Swap periodic y-z plane(s):

- \* Update "evens" and boundary for processor zero:

```
if (procid .ne. numprocs-1) then
```

- \* "Pump up" "evens"---get ready to swap:

```
do 10 countz = 1,nz
```

```
do 20 cntnv = 1,ny
```

```
pumpuprho(cntnv,countz) =
```

```
* rho(nx*cntnv-1,countz)
```

```

        if (withn) pumpuplrhon(cntnv,countz) =
*   rhon(nx*cntnv-1,countz)
20  continue
10  continue
        end if

* Swap "evens":
* WARNING!! -This method "yaks" for over 100 processors, 'n stuff.

        if (procid .ne. numprocs-1) then
            call MPI_SEND(pumpuplrho,ny*nz,MPI_REAL,
*   procid+1,procid+100,MPI_COMM_WORLD,ierr)
            if (withn) call MPI_SEND(pumpuplrhon,ny*nz,MPI_REAL,
*   procid+1,procid+200,MPI_COMM_WORLD,ierr)
            end if

        if (procid .ne. 0) then
            call MPI_RECV(pumpdnlrho,ny*nz,MPI_REAL,
*   procid-1,procid+99,MPI_COMM_WORLD,status,ierr)
            if (withn) call MPI_RECV(pumpdnlrhon,ny*nz,MPI_REAL,
*   procid-1,procid+199,MPI_COMM_WORLD,status,ierr)
            end if

* "Pump down" "evens":

```

```

if (procid .ne. 0) then
  do 30 countz = 1,nz
  do 40 cntnv = 1,ny
    rho(nx*(cntnv-1)+1,countz) =
*   pumpdnlrho(cntnv,countz)
    if (withn) rhon(nx*(cntnv-1)+1,countz) =
*   pumpdnlrhon(cntnv,countz)
40  continue
30  continue
end if

```

Since the first and last processors only share one boundary with a neighbor, the very first and last boundary must be updated as a “mathematical boundary.”

\* Update physical boundary for processor zero:

```

  if (procid .eq. 0) then
c-----
c  x = xmin
c  (liniensymmetrie entlang z-achse)
c-----
  if (perio(1) ) then

  do 110 iz = 2, nz1
  do 110 iv = nx+1, nv1,nx

```

```
        rho(iv,iz) = rho(iv+nx3,iz)
        rhon(iv,iz) = rhon(iv+nx3,iz)
110 continue

    else if ( lsym(1,1) ) then

        do 120 iz = 2, nz1
        do 120 iv = nx+1, nv1,nx
            rho(iv,iz) = rho(nv1-iv+4,iz)
            rhon(iv,iz) = rhon(nv1-iv+4,iz)
120 continue

        else

            do 140 iz = 2, nz1
            do 140 iv = nx+1, nv1,nx
                rho(iv,iz) = crho1(1,1)*rho(iv+2,iz) + crho2(1,1)*rho(iv+4,iz)
                rhon(iv,iz) = crho1(1,1)*rhon(iv+2,iz)+crho2(1,1)*rhon(iv+4,iz)
140 continue

        end if
    endif

* Make certain boundaries are in sync:
    call MPI_BARRIER(MPI_COMM_WORLD,ierr)
```

\* Update "odds" and boundary for final processor:

```

        if (procid .ne. 0) then
* "Pump up" "odds"---get ready to swap:
        do 50 countz = 1,nz
            do 60 cntnv = 1,ny
                pumpuprrho(cntnv,countz) =
* rho(2+(cntnv-1)*nx,countz)
                if (withn) pumpuprrhon(cntnv,countz) =
* rhon(2+(cntnv-1)*nx,countz)
60        continue
50        continue
            end if

```

\* Swap "odds":

\* WARNING!! -This method "yaks" for over 100 processors, 'n stuff.

```

        if (procid .ne. 0) then
            call MPI_SEND(pumpuprrho,ny*nz,MPI_REAL,
* procid-1,procid+99,MPI_COMM_WORLD,ierr)
            if (withn) call MPI_SEND(pumpuprrhon,ny*nz,MPI_REAL,
* procid-1,procid+199,MPI_COMM_WORLD,ierr)
            end if

```

```

        if (procid .ne. numprocs-1) then
        call MPI_RECV(pumpdnrrho,ny*nz,MPI_REAL,
*   procid+1,procid+100,MPI_COMM_WORLD,status,ierr)
        if (withn) call MPI_RECV(pumpdnrrhon,ny*nz,MPI_REAL,
*   procid+1,procid+200,MPI_COMM_WORLD,status,ierr)
        end if

```

\* "Pump down" "odds":

```

        if (procid .ne. numprocs-1) then
            do 70 countz = 1,nz
            do 80 cntnv = 1,ny
                rho(cntnv*nx,countz) =
*   pumpdnrrho(cntnv,countz)
                if (withn) rhon(cntnv*nx,countz) =
*   pumpdnrrhon(cntnv,countz)
            80 continue
        70 continue
        end if

```

\* Update physical boundary for final processor:

```

        if (procid .eq. numprocs-1) then
c
c-----

```

```

c x = xmax
c (liniensymmetrie entlang z-achse)
c-----
  if ( perio(1) ) then

    do 210 iz = 2, nz1
    do 210 iv = 2*nx, nv1,nx
      rho(iv,iz) = rho(iv-nx+3,iz)
      rhon(iv,iz) = rhon(iv-nx+3,iz)
210 continue

    else if ( lsym(2,1) ) then

      do 220 iz = 2, nz1
      do 220 iv = 2*nx, nv1,nx
        rho(iv,iz) = rho(nv-iv+nx2,iz)
        rhon(iv,iz) = rhon(nv-iv+nx2,iz)
220 continue

    else

      do 240 iz = 2, nz1
      do 240 iv = 2*nx, nv1,nx
        rho(iv,iz) = crho1(2,1)*rho(iv-2,iz) + crho2(2,1)*rho(iv-4,iz)
        rhon(iv,iz) = crho1(2,1)*rhon(iv-2,iz) + crho2(2,1)*rhon(iv-4,iz)

```

```
240 continue
```

```
end if
```

```
endif
```

“Barrier call” seen by all processors—to make sure that they are all “in sync” before returning control to the main program. This call is almost certainly superfluous.

\* Let's be safe:

```
call MPI_BARRIER(MPI_COMM_WORLD,ierr)
```



